FIRE RESISTANCE OF LOAD-BEARING LSF WALLS: CRITICAL TEMPERATURE

ALAN VÍTOR DEVENS

Dissertation Submitted to the Polytechnic Institute of Bragança (Portugal) with the Universidade Tecnológica Federal do Paraná (Brazil) to Fulfilment of the Requirements for the Double Diploma program to obtain the degree of **Master's degree in Industrial Engineering - Mechanical Engineering branch.**

Supervised by:

Prof. Doctor Paulo Alexandre Gonçalves Piloto

Prof. Doctor Diego Rossetto

This dissertation does not include the comments and suggestions mentioned by the Jury

BRAGANÇA
2022-2023

Declaro que o trabalho descrito neste relatório é da minha autoria e é da minha vontade que o mesmo seja submetido a avaliação.

Nome do Aluno - Número Mecanográfico

Dedicatory

I dedicate this work to all people who had their lives taken by fire incidents and pray that their souls have found serenity and peace on the other side. Especially to the 242 colleagues of Santa Maria, 27/01/2013 will not be forgotten.

Acknowledgement

I am grateful to all people who have crossed my path and been a piece of what I am today, especially to:

My family gives me every kind of support and is my safe place to return. My reason to keep fighting;

The 3D for the friendship, patience and great memories, you made this year unforgettable. Pedro for the first meal here (so careful), Mancuso for being my main entertainment for 10 months and Nava for the travels and Spotify playlists;

The F&C for be my war mates in the first mouths 8800 km away from home. We fight together and the histories will echo forever;

The C-Village for the best and most fun nights. Without you, this journey would be much less enjoyable;

My friends from Rotaract Dois Vizinhos Amizade e 4640 District, who have kept in contact and motivated me, will be a pleasure to return to you;

Beatriz and Nala, both with warm hugs and funny walks;

All my ERASMUS friends, with whom I opened my mind about the world, and a mind that expands, never returns to its previous size;

Paulo for the teachings and motorsport talks;

UTFPR for my graduation and the opportunity of the double diploma program;

IPB for the reception and support.

Resumo

Esta monografia apresenta uma investigação numérica do desempenho ao fogo de paredes de Light Steel Frame (LSF), normalmente utilizadas em estruturas de edifícios. Este estudo centra-se em seis ensaios de LSF em escala real com diferentes níveis de carga, formas de montantes, classes de materiais e camadas de proteção. As simulações são desenvolvidas utilizando análises térmicas e mecânicas não interligadas. A análise térmica é baseada num modelo numérico híbrido, incorporando resultados experimentais para prever com exatidão a temperatura da parede de LSF. São desenvolvidas três simulações mecânicas diferentes. A análise de encurvadura elástica é utilizada para determinar o modo de instabilidade (utilizado para a imperfeição geométrica). A análise não linear material e geométrica com imperfeição (GMNIA) é utilizada para determinar a capacidade de carga da estrutura do LSF à temperatura ambiente e, finalmente, a simulação termomecânica é efetuada com o efeito da temperatura na estrutura LSF com um nível de carga constante.

O modelo foi validado através de comparações com seis ensaios experimentais à temperatura ambiente e em condições de incêndio. O erro quadrático médio foi determinado para cada comparação. Foram obtidos erros inferiores a 100 °C para a estrutura metálica.

Os resultados mostram que a resistência ao fogo (R) das paredes de LSF diminui à medida que o nível de carga aumenta, quando protegidas por camadas de placas de gesso cartonado. A presença de isolamento da cavidade das paredes de LSF é também examinada. As paredes de LSF feitas de pilares ocos (secções fechadas) com cavidades com isolamento podem melhorar a resistência ao fogo em comparação com as suas semelhantes não isoladas, mas tal não é verificado para as secções transversais tradicionais do tipo C (secções abertas). Quando se utilizam cavidades vazias, a resistência ao fogo dos pilares de secção oca é geralmente mais elevada do que a dos pilares de secção abertas similares.

É apresentada uma nova proposta para determinar a resistência ao fogo, baseada na relação entre a temperatura crítica dos montantes de aço e o nível de carga. A relação proposta permite a previsão do tempo de resistência ao fogo através de uma análise térmica preliminar das paredes LSF.

Palavras-chave: Paredes de LSF, Paredes portantes, Resistência ao fogo, Simulações numéricas.

Abstract

This article presents a numerical investigation of the fire performance of Light Steel Frame (LSF) walls, commonly used in building structures. This study is focused on six full-scale LSF tests with varying load levels, stud shapes, material grades, and composite protection layers. Simulations are developed using uncoupled thermal and mechanical analyses. The thermal analysis is based on a hybrid numerical model, incorporating experimental results to accurately predict the temperature of the LSF wall. Three different mechanical simulations are developed. The elastic buckling analysis is used to determine the mode of instability (used for geometric imperfection). The Geometric and Material Non-Linear Imperfection Analysis (GMNIA) is used to determine the load-bearing capacity of the LSF structure at room temperature, and finally, the thermo mechanical simulation runs with the temperature effect on the LSF with constant load level.

The model was validated through comparisons with six experimental tests under room temperature and fire conditions. The RMSE has been determined for each comparison. Errors under 100 °C was achieved to all metallic structure.

The results show that the fire resistance (R) of LSF walls decreases as the load level increases, when protected by gypsum plasterboard layers. The presence of cavity insulation in LSF walls is also examined. Cavity-insulated LSF hollow stud (closed sections) walls may improve the fire resistance compared to their non-insulated counterparts, but this is not verified to the traditional lipped cross sections (open sections). When using void cavities, the fire resistance of hollow section studs is usually higher than the corresponding similar-lipped section studs.

A new proposal is presented to determine the fire resistance, based on the relationship between the critical temperature of the steel studs and the load level. The proposed relationship enables the prediction of fire resistance time through a preliminary thermal analysis of the LSF walls.

Keywords: LSF walls, load-bearing walls, fire resistance, numerical simulations.

Summary

List of Tables

List of Figures

1 Introduction

The steel structural system has experienced a resurgence among designers and construction contractors who are seeking innovative technologies. In recent years, steel construction has emerged as a standard and technologically advanced alternative to the traditional concrete method. Particularly in Brazil and Portugal, steel structures are increasingly being used in multistory buildings, primarily residential dwellings. Several advantages have been realized by utilizing steel structures and the efficiency of industrialized construction processes, including improved accuracy and faster project completion.

To further enhance the benefits of industrialized construction, lighter and more cost-effective metallic structures have been developed. One such system is the Light Steel Framing (LSF) system, which has been widely adopted in residential construction in North America, United Kingdom, Australia, and Japan [1]. Recently, it has gained popularity in emerging economies as well. The LSF system incorporates the principles of construction industrialization, including rationalization, standardization, modular coordination, and job site transformation.

The LSF system offers various construction methods, such as prefabrication into panels or modules, as well as on-site assembly. From an industry perspective, modular construction holds the most promising future by employing the just-in-time methodology. Factory production of pre-engineered buildings that are delivered to the site and assembled as large building components enable rapid construction, minimizing errors and losses [2]. Additionally, the recyclable and reusable nature of steel structures adds to their appeal.

LSF finds wide application across different construction sectors, including industrial complexes, commercial buildings, and residential structures. It typically utilizes cold-rolled steel with various profiles such as U, C, Σ or Z, or their variants (complex composite sections), which serve as partition walls or structural walls with a thickness of the sheet can range between 0.6 to 3.0

mm [3].

Figure 1.1 – Multi-storey LSF residential building. Adapted from [3].

The use of cold-formed steel (CFS) dates back to the 1800s, however the typical framing members we see today appeared in the early 20th Century with the Virginia Baptist Hospital built around 1925 in Lynchburg, Virginia. The walls were load-bearing duty, with a floor system framed with double back-to-back CFS-lipped channels. The three “homes of the future” made of cold-formed steel exhibited in 1933 at the Chicago Century of Progress decreed the establishment of this construction method [4].

Steel structures are often chosen for their strength, durability, and ability to withstand extreme weather conditions such as seismic zones. But when steel is exposed to high temperatures, it begins

to lose its strength and stiffness which can cause it to deform and buckle leading to potentially catastrophic consequences. This deformation can compromise the structural integrity of the building, leading to collapse or failure.

A good fire safety design is vital for safeguarding lives, limiting the risk of full development of the fire, limiting the spread inside the building and limiting the risk of spread to other buildings, besides facilitating fire-fighting. Passive fire protection refers to the use of fire-resistant materials and structural design strategies to prevent the spread of fire and limit its potential damage. This can include fire-resistant walls, doors, floors, and firestops, which act as barriers to slow down the fire's progression and maintain the structural integrity of a building. On the other hand, active fire protection involves the use of systems and equipment to actively detect, control, and extinguish fires. This includes fire alarm systems, sprinkler systems, fire extinguishers, and fire suppression systems.

The fundamental objectives of fire safety are to minimize the risk to life and reduce the loss of property and for that, the design resistance of a building structure needs to be functional for a certain time in minutes enough for all occupants to escape to a safe place and produce no-spread flames [5], the requirements vary according to each country's legislation and often have a distinction of the use of the building.

The increase in protection in LSF walls comes from the use of single or multi-layer thermal insulation systems, the most common materials made for plasterboards are gypsum, OSB or cork, as well as cavity fillers with mineral wool, which are widely used in walls to increase the energy performance and ensure the safety of users preventing the passage of dark smoke. Sometimes this cavity insulation leads to a reduction of the fire resistance time of the system (R), caused by the thermal bowing effect, that induces an earlier bending of the member by the high gradient of temperature and consequently thermal expansion between fire exposed and unexposed side [6]

To mitigate the risk of steel structures failing in a fire, building codes and regulations often require fire-resistant coatings or other measures to protect the steel from high temperatures, the

European Standard EN13501-2 [7] has classifications for building elements based on integrity (E), insulation (I) and resistance (R). When an element is tested, it receives a classification according to the time to the shortest time to fire resistance.

Several authors have conducted experiments and numerical studies to understand the behaviour of these structures in fire conditions. These studies aim to improve the safety and performance of buildings in fire incidents, ensuring adequate protection for both occupants and the structure itself. The dedication to investigating the properties of fire-protected LSF walls using different types of fire protection, such as intumescent coatings, gypsum plasterboard panels, and insulation materials. These studies involve both laboratory experiments and numerical analyses through computer simulations.

Experiments aim to evaluate the performance of LSF walls when exposed to different fire conditions, such as temperature variations, heat flux, and fire duration. Temperature measurements, structural deformation, are considered to determine the fire resistance of the walls. The results obtained allow for the analysis of the behaviour of the structures and the verification of the efficiency of the protection systems used [8]–[18].

In addition to experiments, numerical studies play a fundamental role in the analysis of the properties of fire-protected LSF walls. Through computer simulations, it is possible to model the thermal and structural behaviour of the walls in different fire scenarios. These numerical analyses enable a deeper understanding of the phenomena involved and can assist in the development of more efficient and cost-effective fire protection solutions for LSF [18]–[21].

In this dissertation, a numerical model is introduced and its thermo-mechanical accuracy is validated against multiple full-scale specimens. The study draws significant conclusions on the critical temperature of LSF walls under varying load levels. The findings are also compared to the correlation between the load level of LSF and the hot flange temperature, which can be assumed to be the critical temperature [10], [19]. This correlation, along with the simulation of the temperature

distribution, can be used to estimate the load-bearing capacity of LSF walls during a fire, eliminating the need for specimen testing.

1.1. Framework

The traditional methods of conducting standard tests are time-consuming and expensive and require the usage of modern technology, also highly qualified personnel. Nowadays the entire process of building development relies on computer-aided design, from architectural modelling to the calculation of steel structures. This dissertation aims to be another brick in the wall of the castle of advances in this area of technology, using a multiphysics-software and multidisciplinary study, while also acknowledging the importance of theoretical advancements.

Computer-aided design (CAD) has revolutionized the field of structural engineering, providing numerous advantages to professionals in this discipline. By integrating advanced software tools into the design process, structural engineers can enhance their productivity, accuracy, communication, visualization, and overall efficiency.

The development of objectives of the original proposal is inspired in this numeric field with software that can help in enhanced visualization e presentation besides cost and time savings.

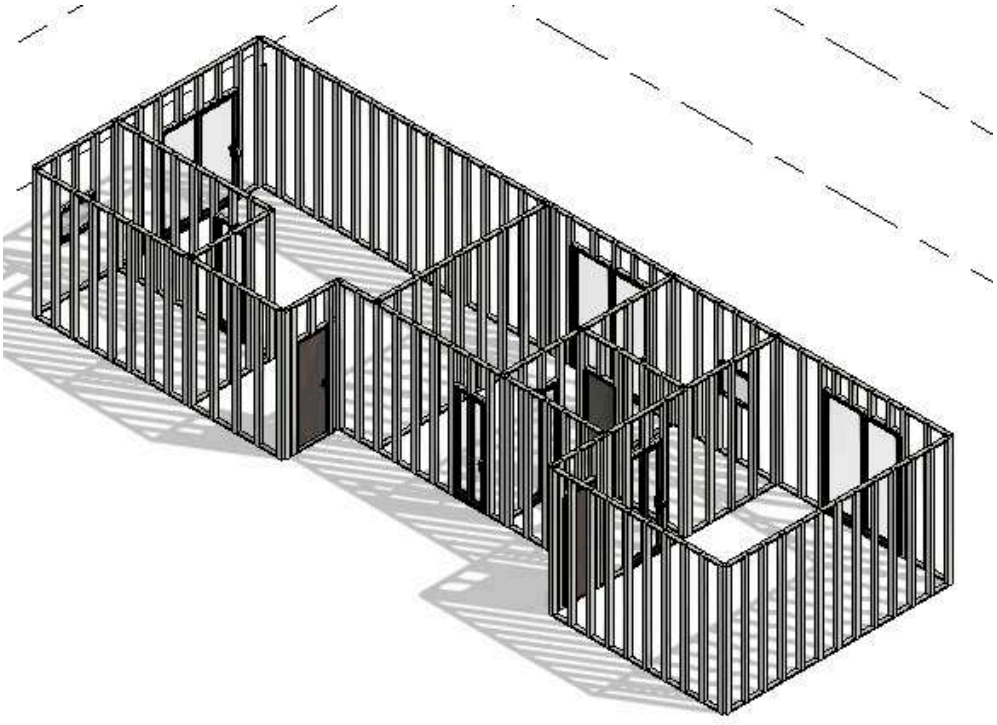

Figure 1.2 – Computer-aided design of LSF house.

Standard fire tests on materials have destructive nature, particularly composite layers that are not easily recyclable, the cost implications of such tests are significant. These materials are often expensive, adding to the overall expense of the testing process. For instance, based on a budget analysis conducted with a Portuguese company (J.Soares Correa) specializing in cold-formed shapes, the average cost was found to be €907.50 for every 100 linear meters of steel used in square and rectangular hollow sections, which is used in this study. Another research study revealed that the cost of a 15mm plasterboard gypsum is approximately €3.79 per m^2, while mineral wool with a thickness of 100mm costs around €5.35 per m^2.

In this thesis, we conducted more than 60 simulations, and each simulation led to substantial material and resource savings. For example, for one simulation, we saved 24 linear meters of steel, 36 square meters of double-layered gypsum plasterboard, dozens of screws, cavity insulation, combustible gas, electricity, and other associated resources. These simulations play a crucial role in reducing costs by minimizing the consumption of these materials and resources.

1.2. Dissertation Content

Chapter 2: Presents the state of the art which describes, studies regarding load-bearing LSF walls under fire conditions.

Chapter 3: Presents the specimens evaluated, and discusses the methods of solution, fire safety requirement, mechanical and thermal properties and the interactive solution methods.

Chapter 4: Presents the four-step solution methods used for the validation method.

Chapter 5: Presents the parametric study and the influence of load level in LSF load-bearing walls at high temperatures.

Chapter 6: Presents a discussion of the results obtained.

Chapter 7: Presents the main conclusions about this work and future investigations that are required.

1.3. Objectives

The objective of this dissertation is to analyze the structural and thermal performance of LSF walls in fire situations. The research seeks to investigate the behavior of the LSF system with different configurations, such as protection layers, cavity insulation, steel grade and column section, in order to provide insights to improve the safety and efficiency of these structures. Through numerical simulations and experimental validation, it is intended to evaluate the fire resistance of LSF walls and to analyze the effect of different load levels. The results obtained will allow the development of more robust design guidelines and practical recommendations for fire protection in SFL structures, contributing to the safety of civil construction and risk mitigation

Specific tasks are included to be investigated using the finite element software (ANSYS APLD):

- An elastic buckling analysis to determine the critical load and the modes of instability. This

information is used to introduce the geometric imperfection of the LSF;

- A non-linear static analysis to determine the load-bearing resistance, using plastic behaviour and large displacement;
- Using standard fire, a non-linear transient thermal analysis is used to determine the temperature field over time;
- The validation of the thermal and mechanical model including convergence tests, boundary conditions, solution methods, and convergence criteria, is presented. The average error estimation is also determined to compare the numerical results with the experimental results;
- The parametric analysis regarding the load level is presented and a new proposal is developed for the critical temperature of the LSF with a compilation from more than a hundred results by other authors.

2 State of the Art

This chapter presents a comprehensive literature review on the research conducted to investigate the fire performance of load-bearing Light Steel Framed (LSF) Walls. The objective of this literature review is to explore experimental, numerical, and simplified models to enhance our understanding of load-bearing LSF Walls under fire conditions. By examining previous studies, one aim to gain insights into the behaviour and performance of these walls when exposed to fire.

Bibliometric research in the Scopus database triggered to LSF, load-bearing and walls documents, presents a total of 56 articles about the prompt. Used the *Rstudio* program to examine the results, showing the network of co-occurrence of subjects in Figure 2.1, As can be observed, issues involving fire and high temperatures are the main subject of study.

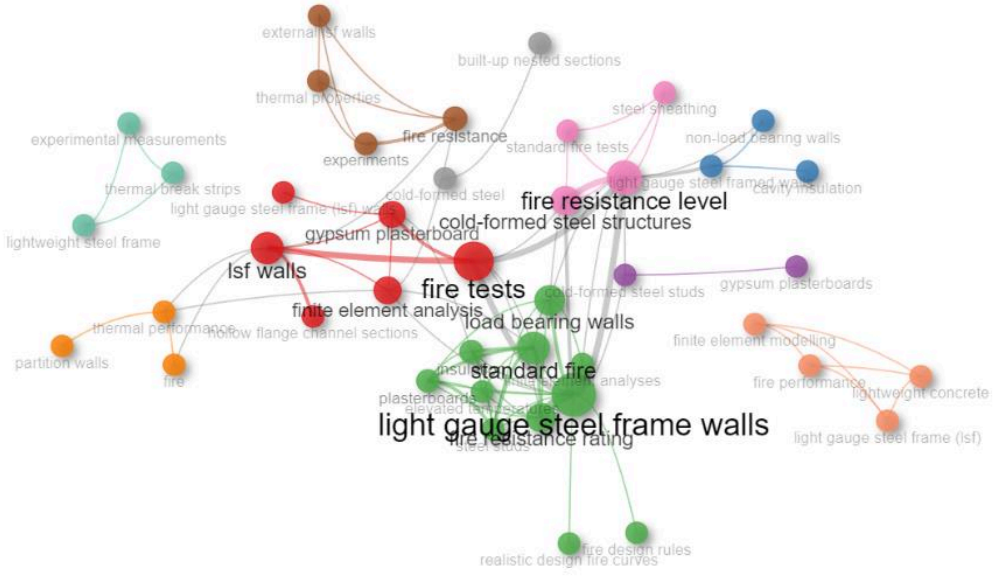

Figure 2.1 – Co-occurrence network.

The most used keywords in studies are visualized in word cloud format in Figure 2.2, it is

more clearly seen that there is a focus on structural walls, fire tests and numeric simulations.

Figure 2.2 – Keywords mostly used in studies.

By examining the existing literature, this thesis aims to synthesize the findings and identify trends, limitations, and areas for further research. This chapter serves as a comprehensive overview of the current state of the art in load-bearing LSF Wall research under fire conditions, providing valuable insights that can inform future investigations and contribute to the development of robust fire safety strategies for load-bearing LSF structures.

Overall, this literature review seeks to establish a solid foundation of knowledge and understanding, paving the way for advancements in the design, construction, and fire protection of load-bearing LSF Walls.

2.1. Previous Experimental Tests

Coming from philosophy, the systematic scientific method provides a strong “way of thinking” to observe and describe a phenomenon. After the formulation of a hypothesis to explain the phenomenon, the next step is the design and conduct of experiments to test the hypothesis, analyze

the results and drawing a conclusion. Many engineering universities worldwide analyze steel structures deeply and produce research results in this area.

Chen [11] analyzed the influence of external insulation of aluminium silicate wool between different material boards in the side exposed to fire, with a comparison of three identical specimens from Chen [10] except for the insulation. The results show an increase of 71% in the mean fire resistance time. The paper shows the effect of different panels in the same layout, such as the better performance of Bolivian magnesium board against the gypsum plasterboard but with the consideration that both types of boards, were not suitable for exterior wall panels, and the combustion of OSB after 148 minutes of fire exposure.

LSF wall panels made of low-strength steel with gypsum plasterboard boards were examined by Ariyanayagam et al. [18], the results showed an increase of fire resistance with the use of noggings and the decrease of that with glass fiber cavity insulation. For the authors, this conclusion is valid for HSS (High Strength Steel) and LSS (Low Strength Steel) steel studs. The use of noggings is recommended by reducing the lateral deflection. This means fewer cracks on the fireside and not allowing the hot gases to penetrate in plasterboards to warm up the studs more quickly. The failure of the cavity insulation to increase the fire resistance is assigned to heat retained on the fireside. This heat made the gypsum calcinate and collapse partially. These actions will remove the thermal barrier and the temperature of the studs rise rapidly.

Dias et al. [12] made experiments to investigate the fire performance of gypsum-steel sheathed walls. The full-scale web-stiffened studs' specimens with 0.4 load level have shown that the presence of steel sheathing helps the maintenance of structural integrity even at high-temperatures and increases the axial load-bearing capacity in approximately 10%, but provides a marginal improvement in the insulation fire resistance. The web-stiffened studs used present a superior performance than the commonly lipped channel stud, with the same load ratio. An improvement of 57.3% in axial compression load was obtained without losing the same level of fire resistance.

Fire tests from Tao et al [9] provide information about the superior properties of cold-formed steel square and rectangular hollow sections (SHS/RHS) due to the better behaviour at high temperatures in comparison with the commonly used lipped channel section (LCS). Another difference between the two types of steel sections is related to cavity insulation. While the LCS, when insulated in your cavity, has its fire resistance decreased due to the bowing deformation, caused by the high-temperature difference between the stud HF and CF, the SHS/RHS provides an improvement of the fire resistance when their cavity has is filled by a glass fiber insulation material.

More recently Vy et al. [8] conducted experimental tests to assess the enhanced load capacity of the back-to-back channel (BC) and nested channel (NC) configurations while maintaining their fire resistance level. These geometrical steel shapes offer a simpler and more cost-effective solution. The observed increase in load capacity is substantial, and the achieved fire resistance is comparable to that of lipped channels. The nested channel design, resembling hollow sections, exhibits a similar thermal performance. However, due to the flange's thickness being twice that of the web, the advantageous effect of cavity insulation is diminished.

A good amount of other experimental fire tests can be found in the well-known literature, with variations of a large number of parameters such: Composition of LSF walls, load-bearing or non-load-bearing elements, steels grades and shapes, number and material of protection layers, as well the kind of insulation by fibers and most of they are or can be the basis to numerical studies

2.2. Previous Numerical Studies

For many centuries, the process to develop a new product or building has, at least, two principal steps before it is finished, the analytic calculus and full-scale prototype (sometimes reduced scale prototype). This kind of development has two problems: The complexity of real engineering problems makes their resolution, many times, impossible to solve analytically and they are sometimes solved by simplified methods, using safety factors, that get away from the real solution. The production of prototypes can be expensive in money and time, and sometimes impossible to many

projects.

In the digital transformation process, mainly in the last 40 years, the minted concept of Computational Aided Engineer (CAE) grows up impressive. The use of software to analyze physical problems by simulation solves complex engineering tasks, saving millions of dollars, years of research and improves the accuracy of studies. A few examples of the importance of numerical studies can be observed in the next few paragraphs.

Ariyanayagam and Mahendran [18] used the experimental results to validate the finite element models to steel studs exposed to a high-temperature developed in *Abaqus CAE*. The numerical results demonstrate a good prediction of time and failure mode, with the numerical model validated, the authors conducted a parametric study of this class of steel, and the results showed a reduction of 25% in the common load ratio to LSS in comparison with HSS stud walls for medium load ratios (0.4 to 0.6) as well as a reduction of critical temperature in the hot flange (HF). These authors also made a parametric study using high-strength steels (HSS) and low-strength steels (LSS).

Perera et al., in 2020 [21] provide a numerical investigation concerning the fire performance of six wall configurations of cold-frame (cavity insulation between the studs), warm-frame (insulation between gypsum plasterboards) and hybrid-frame maintaining the same material quantities. The warm frame showed the best performance of the other layouts for all load ratios. This kind of wall configuration exhibits a lower temperature difference between the hot flange (HF) and cold flange (CF), reducing the risk for thermal bridging, while the cold-frame showed the highest. This paper highlights several numerical and experimental studies to develop a relationship between the hot flange critical temperature and load level.

In 2021 Tao et al. [20] made an important development of numerical models for LSF walls using hollow sections with validation from the experimental results [9]. The thermal analysis confirmed the advantage of using cavity insulation in hollow sections of LSF walls. The Finite element analysis (FEA) showed that higher stud depth provides a better FRL by the reduction of

lateral displacement, and for a given load ratio, the authors did not find a relevant impact for the use of two different steel grades in hollow sections.

An investigation with experimental tests of reduced-scale specimens and numerical evaluation developed by Piloto et al. [19] presents a new proposal to determine the critical temperature in function of load level. These authors also showed the insulation ability usually increases with the number of studs and the measurement of the load-bearing capacity improvement with the number of protective layers.

3 Models, Material and Methods

Structures constructed using LSF exhibit a distinct assembly pattern. Essentially, they consist of a steel framework comprising studs and tracks, enclosed by one or more protective plates. These structures offer the flexibility to fill the internal cavity with thermally insulating materials. The provided Figure 3.1, illustrates a standard wall assembly featuring two layers of plasterboard arranged in different orientations, as advised by manufacturers. It also showcases an example of cavity insulation.

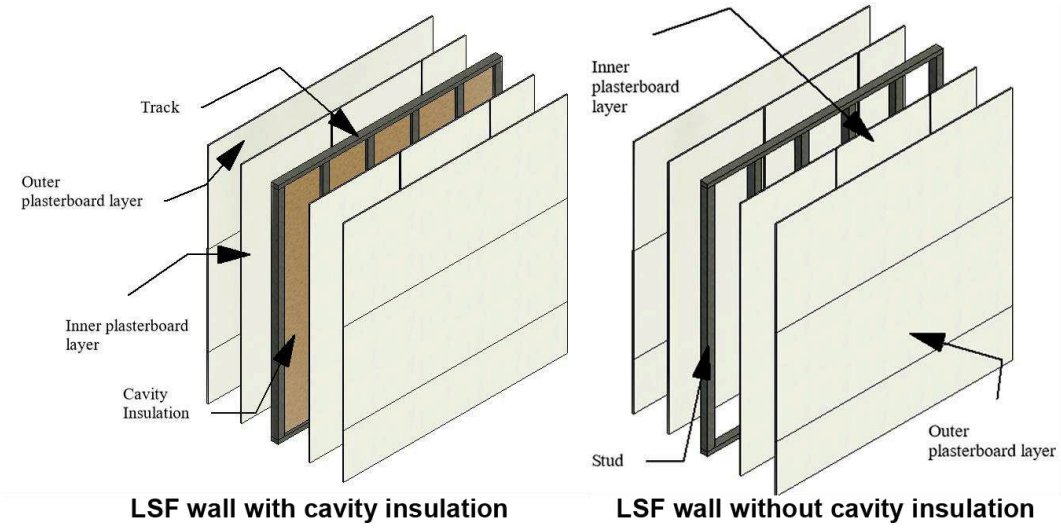

Figure 3.1 - Common configurations of LSF wall.

3.1. Specimens

This investigation wants to evaluate different types of assemblies. For that, six experimental fire tests with a variation of some parameters were chosen, such as steel stud grade, the shape of studs, with and without cavity insulation and other parameters summarized in Table 3.1. Even with differences between specimens, some similarities are maintained to allow comparisons at the end of the study. All of the specimens are walls with an arrangement of six studs were spaced every 600

mm from their center, using fire rated gypsum protective layers, see Figure 3.2.

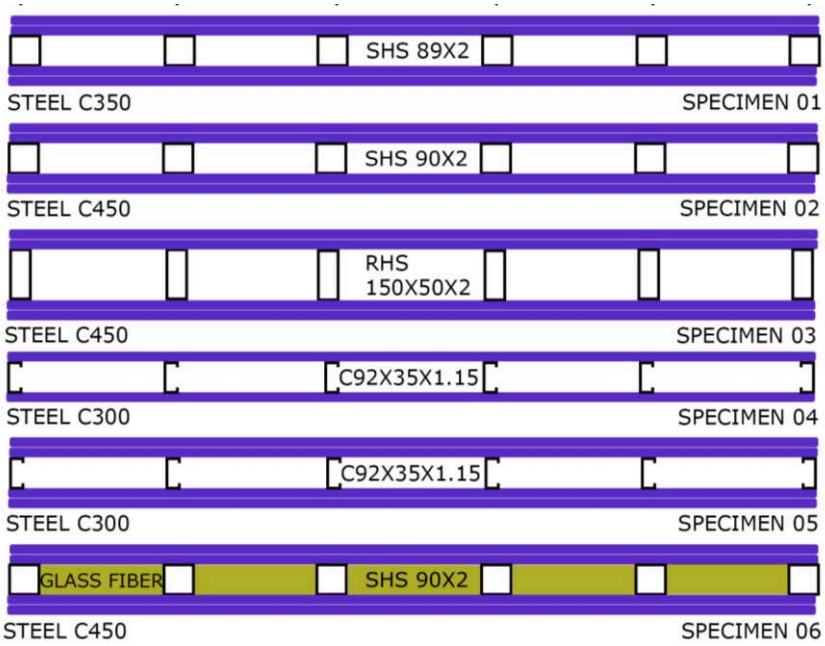

Figure 3.2 – Characteristics of specimens studied.

Specimen 01 is defined in agreement with the experimental investigation developed by Tao et al. [22]. The specimens made of hollow sections 02, 03 and 06 are presented in the work developed by Tao et al. in 2021 [9], and the specimens 04 and 05, with open shapes are presented in the work developed by Ariyanayagam and Mahendran [18]. The information on specimens and their results under fire test is summarized in Table 3.1.

Table 3.1 - Information on specimens

ID	STUD SHAPE	STEEL GRADE OF STUDS	Nº OF PROTECTIVE LAYERS	CAVITY	LOAD BEARING CAPACITY [kN]	LOAD LEVEL [%]	FIRE RESISTANCE [min]
01	SHS89x2.0	C350	2x16mm	\	187	20	237
02	SHS90x2.0	C450	2x16mm	\	193	40	158
03	RHS150x50x2.0	C450	2x16mm	\	182	40	152
04	C92x35x1.15	C300	1x16mm	\	40	20	77
05	C92x35x1.15	C300	2x16mm	\	40	40	124
06	SHS90x2.0	C450	2x16mm	Glass Fiber	193	40	147

In Table 3.1, the steel grade is presented with usual classification. The classification of steel is standardized by EN 10219-1 and follows the minimum required value for yield strength resistance in N/mm^2. This is known as how “nominal value” and is used for a conservative estimation, but a manufacturer of structural steel can use a different alloy and provide a better resistance for the same steel grade.

3.2. Standard Fire

Fire is a combustion process that involves the release of heat and flames, occurring when three factors coexist: fuel, a source of heat (ignition), and an oxidizing atmosphere. A fire event is complex to determine precisely, in a room that can be filled using different materials that when exposed to high temperatures, can release flammable gases as the fuel (1), that affects the flame spread and consequently the analysis of heat transfer by conduction, convection and radiation.

To simplify most of the analysis, some standard fire curves for different situations are presented: Standard temperature-time curve, external fire curve, hydrocarbon curve and natural fires in entire compartments or localized fire events affecting single elements.

Standard fire curves provide an approximate representation of natural curves, but they fail to

account for factors such as openings, space, fire load density within the compartment, and the decay phase. These curves specifically depict the temperature rise following the flashover period, during which the structure experiences intense heat and temperature stresses. Namely, according to EN 1991-1-2 [23], there are different types of curves, such as Natural Fire and Standard Fire time-temperature curves.

For this work, the standard temperature curve was selected, presented by the ISO 834-1 [24] and accepted by EN1993-1-2 [25] (Figure 3.3). This standard is given by the following equation (1), where T is the mean temperature in Celsius degrees and t is time in minutes:

$$T = 345 * \log(8t + 1) + 20 \quad (1)$$

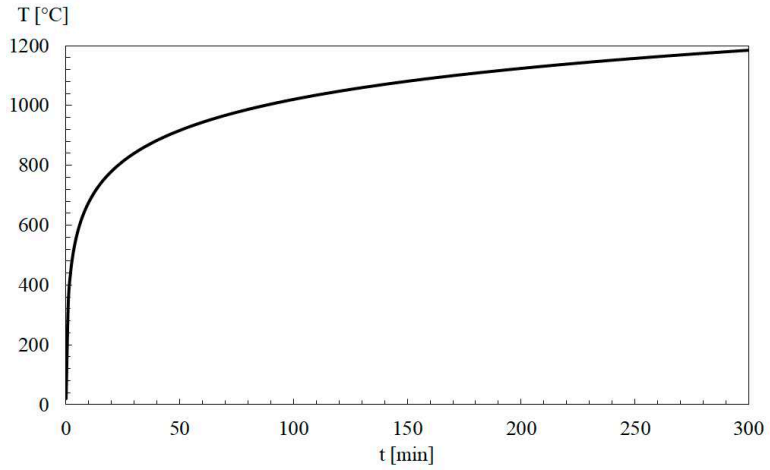

Figure 3.3 - ISO 834 standard time-temperature curve.

3.3. Fire Resistance Criteria

Following standard EN13501[7], the criteria of loadbearing capacity of vertical elements under fire (R) have two terms and are determined when one of the following criterium has been exceeded: Axial contraction limit or rate of axial contraction. The loadbearing criterion (R) measures

the ability of the element to support the imposed load. The ability is determined from the measurements of the maximum deflection (C) or by the rate of deflection (dC/dt), where h, in mm, represents the initial height of the test specimen, once the load is applied.

a) Axial Contraction: C = h/100 [mm]

b) Rate of axial contraction: dC/dt = 3h/1000 [mm/min]

Where h is the initial column height, in millimeters and C is the displacement.

The method consists of the application of a static load in the LSF wall at room temperature, after that the temperature rises, and with time, the mechanical properties of steel weaken to failure and steel elements try to expand. In an experimental test, the displacement C is mensurable by displacement sensors spread in the column.

The stud suffers a negative displacement at the beginning of the experiment when the load is applied. After that, the temperature rises and the steel tends to thermally expand turning the displacement, as positive. This trend continues until the structure is not able to support the load and collapses. When the maximum displacement gets C or the displacement rate gets dC/dt, the fire resistance is defined. This defines the time in complete minutes that the wall resists under fire, and each wall obtains the fire rating given by classification rating: R15, R20, R30, R45, R60, R90, R120, R180, R240 and R360.

3.4. Fire Integrity Criteria

Another criteria from [7] is the Integrity Criteria (E) is founded by experimental and observable methods based on the following of one of the three aspects:

a) Cracks or opening in excess of given dimensions;

b) Ignition of a cotton pad;

c) Sustained flaming on the unexposed side.

In an experimental environment, the researchers must be aware visually of the appearance of cracks or flames on the unexposed side over time, and at any given time, use a cotton pad emerged in alcohol to test the existence of hot gases in the unexposed side, passing the cotton close of the wall. If he ignites, means that have hot gasses or flames passing by the surface and it fails. The EN13501-2 [7] determine which integrity value is established when the first, whatever it is, fails. In numerical studies, this criterion is not possible to be evaluated, but in experimental tests, this criterion is used.

3.5. Fire Insulation Criteria

The performance of insulation is classified in [7] by the rise of temperature on the unexposed side, limited to 140 °C above the initial mean temperature or a maximum temperature at any point 180 °C above the initial mean temperature.

a) $T_{ave} = (T_o) \pm 140$ [°C];

b) $T_{max} = (T_o) \pm 180$ [°C].

A LSF wall could be rated by more than one criterion (REI). The corresponding letter is added and the value of the fire rating, changes to the lowest value achieved by the first criterium to have failed in time.

3.6. Thermal Properties

Different materials were used for fire insulation, the energy equation (2) which governs the conduction of heat in three-dimensional solid bodies, involves three temperature-dependent material properties: The thermal conductivity (λ), specific heat at constant pressure (C_p), relative density (ρ). Another thermal property is required to be used in the boundary condition: the emissivity (ε). Figure 3.4 presents the thermal properties used for gympsum in the numerical simulation.

$$\frac{\partial}{\partial x}\left(\lambda\frac{\partial T}{\partial x}\right)+\frac{\partial}{\partial y}\left(\lambda\frac{\partial T}{\partial y}\right)+\frac{\partial}{\partial z}\left(\lambda\frac{\partial T}{\partial z}\right)=\rho C_p\left(\frac{\partial T}{\partial t}\right) \quad (2)$$

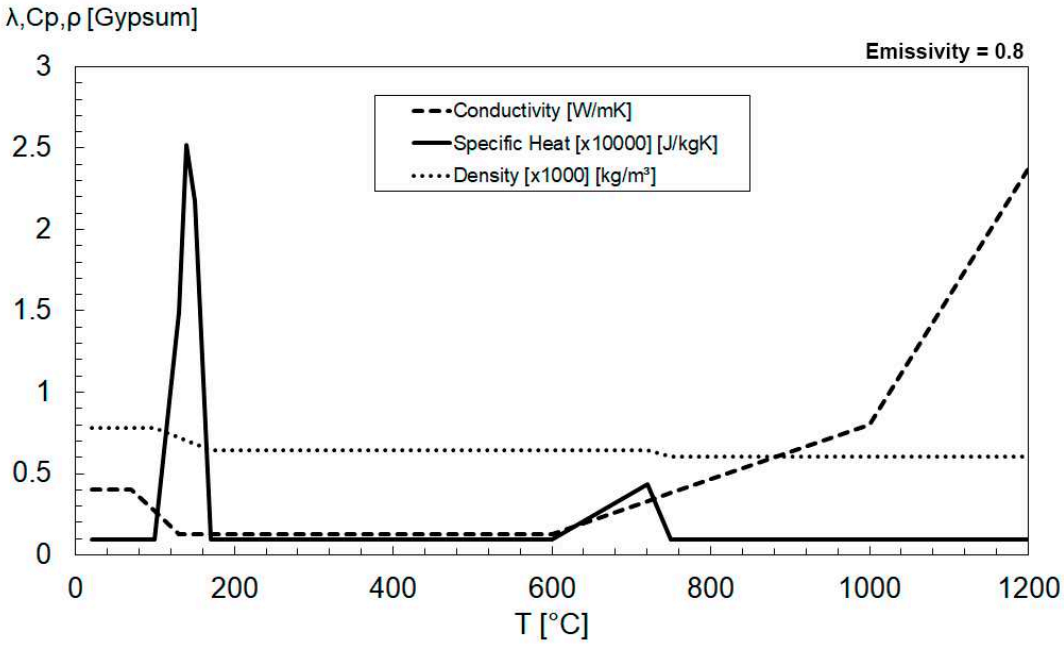

Figure 3.4 - Thermal properties of gypsum plasterboard with temperature, [26].

The standard prEN1995-1-2 [26] presents these thermal properties to gypsum plasterboard, it is the most common material used for fire protection in LSF. This material is made from a naturally non-combustible material, which presents a significant amount of water chemically bounded and free. When heated, this material requires significant heat energy to evaporate. This reaction delays the temperature evolution of the LSF structure [15]. The original density of gypsum consider was 781 kg/m³ [27]. The emissivity was taken as 0.8 for gypsum [28].

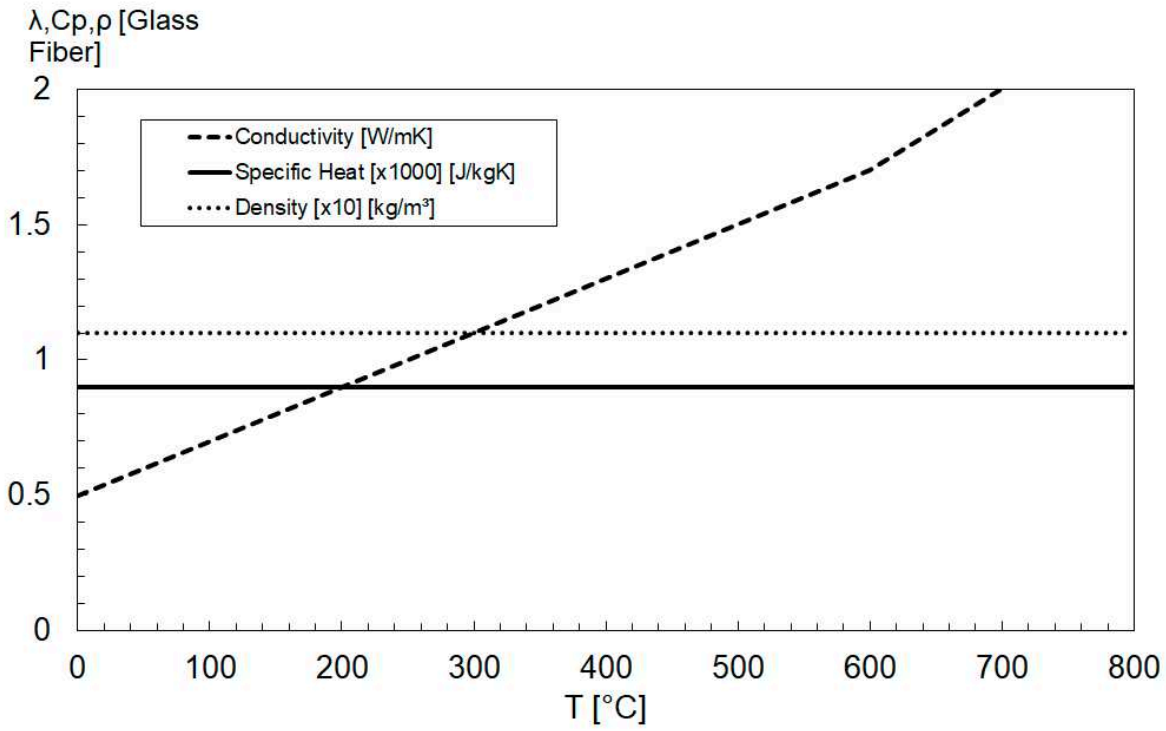

Figure 3.5 - Thermal properties of glass fiber with temperature, [29].

A high level of thermal insulation can be achieved using glass fiber insulation in the cavity region. This material is produced by melting glass and then spinning it into thin fibers. The thermal bridges created by the relationship of the cavity insulation to the steel structure can lead to a higher concentration of heat transfer in the plaster-steel contact area [30]. Figure 3.5 presents the values of glass fiber thermal properties used in this thesis.

The thermal properties used for the glass fiber are proposed in the work presented by Keerthan et al. [29]. The proposed thermal conductivity changes with temperature, followed by equation (3), the density of 11 kg/m³ and the specific heat of 900 J/kg°C remain constant. The authors reported that these properties may vary depending on the manufacturing method.

$$\begin{aligned} \lambda &= 0.5 + 0.0002\mathrm{T}\,;\, 0 < \mathrm{T} \leq 600\ [°\mathrm{C}] \\ \lambda &= -7.8 + 0.014\mathrm{T}\,;\, 600 < \mathrm{T} \leq 700\ [°\mathrm{C}] \\ \lambda &= 0.08\mathrm{T} - 54\,;\, 700 < \mathrm{T} \leq 800\ [°\mathrm{C}] \end{aligned} \tag{3}$$

The thermal properties used for the carbon steel were obtained from the standard EN1993-1-2 [25] and graphically depicted in Figure 3.6. The emissivity is equal to 0.7 and the density equals ρ_o= 7850 kg/m³.

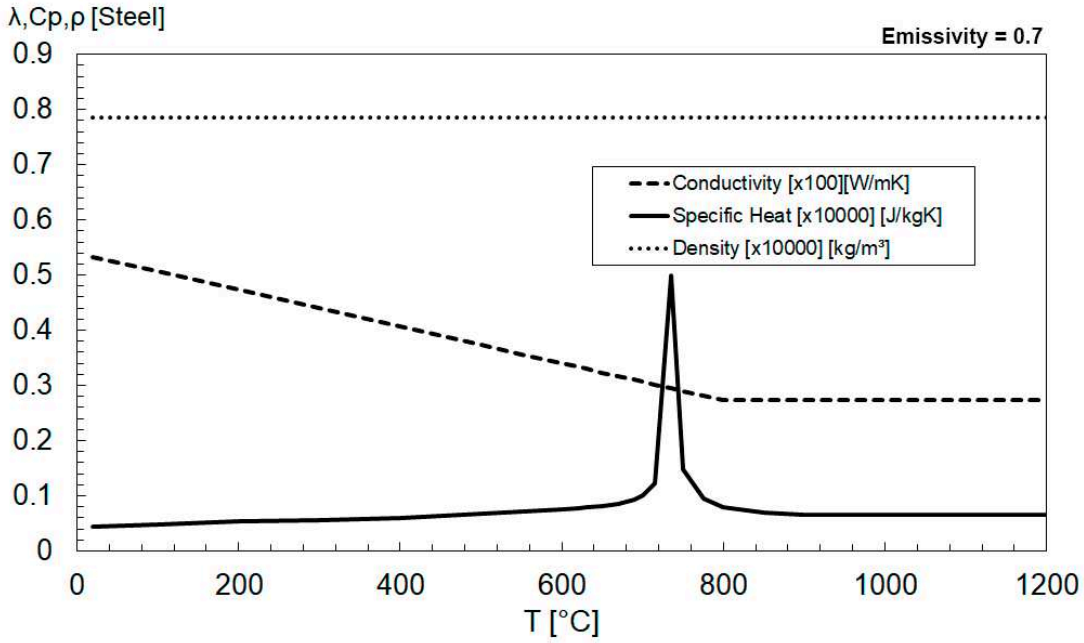

Figure 3.6 - Thermal properties of steel with temperature with temperature, [25].

Every steel grade has the same thermal properties, and follows equation (4) where Θ_a is the steel temperature. The peak shown in the figure is due to a crystallographic endothermic transformation of the steel at around 735 [ºC] for a value of 5000 [J/kgK]. For structural elements with failure temperatures close to these temperatures, this change can have a non-negligible effect on the fire resistance duration [25].

$$C_a = 425 + 7.73x10^{-1}(\Theta_a) - 1.69x10^{-3}(\Theta_a)^2 + 2.22x10^{-6}(\Theta_a)^3; 20 < \Theta_a \leq 600\ [°C]$$
$$C_a = 666 - \left[\frac{13000}{\Theta_a - 738}\right]; 600 < \Theta_a \leq 735\ [°C]$$
$$C_a = 545 + \left[\frac{17820}{\Theta_a - 731}\right]; 735 < \Theta_a \leq 900\ [°C] \quad (4)$$
$$C_a = 650; 900 < \Theta_a \leq 1200\ [°C]$$

The thermal conductivity of steel is high, however, this value tends to decrease as the temperature of the material increases, as shown in Figure 3.6. Equation (5) demonstrates linear decreasing behaviour up to 800 °C, and then a constant behaviour value beyond this temperature.

$$\lambda_a = 54 - 3.33\left[\frac{\Theta_a}{100}\right];\ 20 < \Theta_a \leq 800\ [°C]$$
$$\lambda_a = 27.3;\ 800 < \Theta_a \leq 1200\ [°C] \quad (5)$$

Even when a structural element is not subjected to any external load, steel undergoes deformation due to temperature effects. Although this property holds no practical significance when the element is unloaded, it becomes relevant for thermo-mechanical simulations. Therefore, this phenomenon will be considered by incorporating the corresponding equation (6) specified in the EN1993-1-2 standard [25]. A graphical representation of this equation can be found in Figure 3.7.

$$\varepsilon_{th} = 1.2x10^{-5}(\Theta_a) + 0.4x10^{-8}(\Theta_a)^2 - 2.416x10^{-4};\ 20 < \Theta_a \leq 750\ [°C]$$
$$\varepsilon_{th} = 11.0x10^{-3};\ 750 < \Theta_a \leq 860\ [°C] \quad (6)$$
$$\varepsilon_{th} = 2.0x10^{-5}(\Theta_a) - 6.2x10^{-3};\ 20 < \Theta_a \leq 750\ [°C]$$

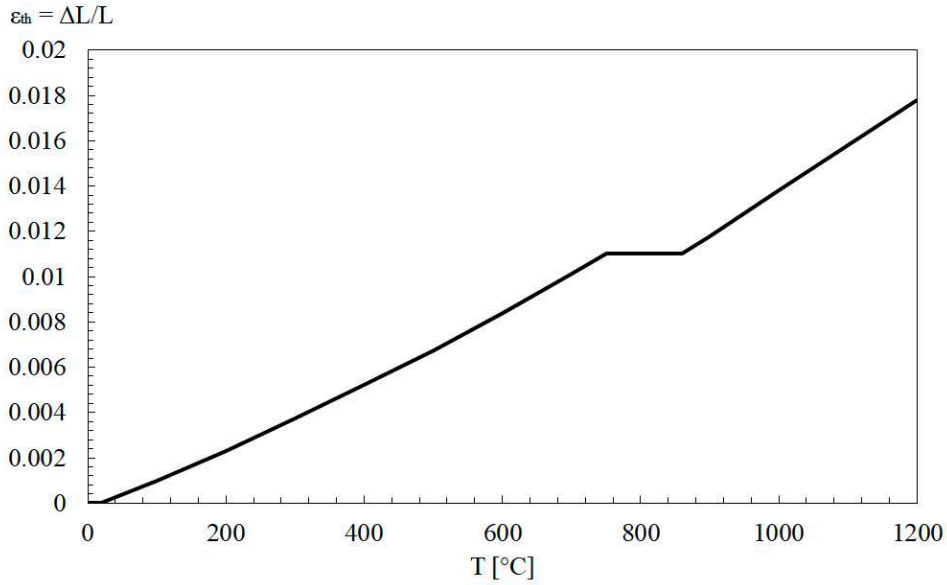

Figure 3.7 - Variation of the coefficient of thermal expansion with temperature.

3.7. Mechanical Properties

During the late 19th and early 20th centuries, the increased use of steel led to a rise in the number of steel grades available. These studies on the mechanical properties of steels at various temperatures and chemical compositions, aimed to understand and develop new metallic alloys with the desired properties. However, it is not always practical or feasible to conduct experimental studies on every type of steel before engaging in numerical analysis.

Is not practical or always possible the experimental study of a kind of steel before the numerical studies, because several constitutive laws were developed and adjusted over the years, one of the most applied is the constitutive law of Ramberg-Osgood to describe the stress-strain relationship using three parameters: Young's modulus (E), the material yield strength (fy) - typically taken as the 0.2% proof stress - and the hardening exponent (n). By using this method, researchers can construct a stress-strain curve for a material at room temperature, allowing them to investigate its properties without considering the shape or size of the material.

Using these parameters, it is possible to plot a stress-strain curve for a material at room temperature. However, when the temperature is increased, the values need to be adjusted using reduction factors. It is well-known that certain properties of steels, such as yield strength and elastic modulus, decrease rapidly in the presence of heat. As a result, stiffness and strength of steel is significantly affected by elevated temperatures.

The upcoming sections will present a comparison between existing standards and the latest research findings. The objective is to emphasize the importance of carefully selecting numerical methods when constructing a stress-strain curve. In this study, in cases where the authors did not provide specific values for higher temperatures, reduction factors were linearly extrapolated from 20°C to 1200 °C, for the lack of equations covering those ranges.

Yield Strength

Figure 3.8 shows that experimental tests provide smaller reductions factors to yield strength than the standard based on hot-rolled steels [25]. It's important to emphasize that the Imran et al. [31] curve used the average between the CHS, SHS and RHS results until 800 °C and the McCann et al. [32] provides different curves to each section until 1000 °C, the curve plotted was determined from RHS. In this manuscript, the Imran curve will be used.

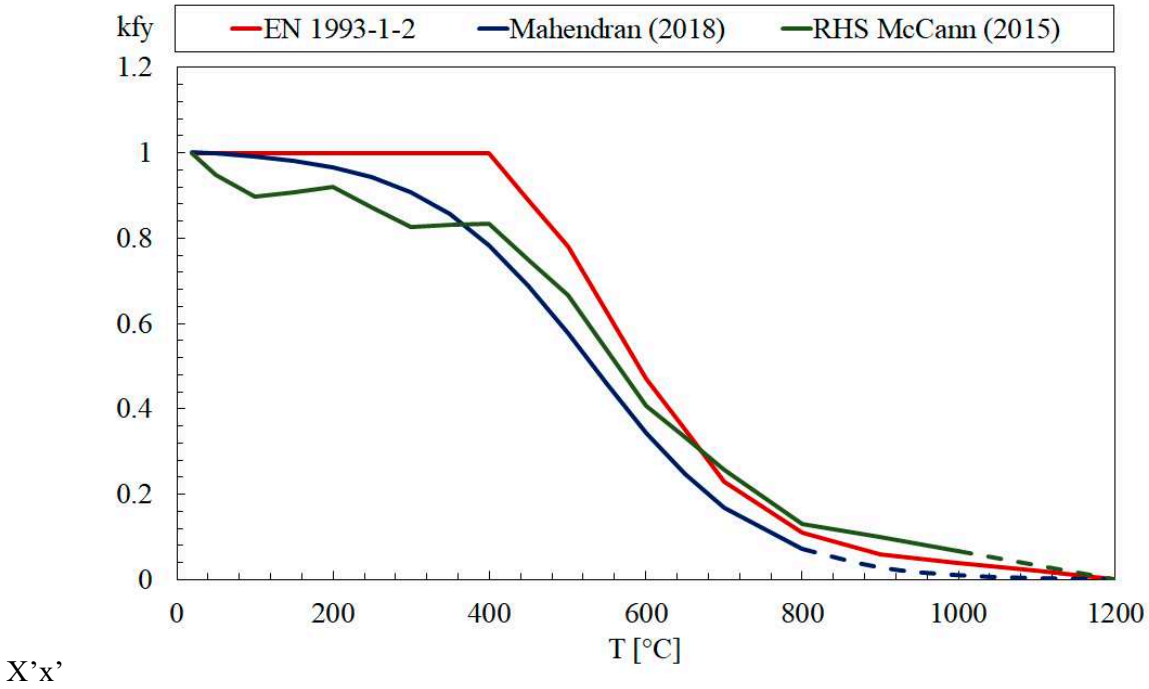

Figure 3.8 - Reduction Factor to Yield Strength, comparison between standard and researchers.

Ultimate Strength

Annex A from EN1993-1-2 [25] provides reduction factors based on the yield strength and will be unconsidered in this comparison. Both works cited above present the results in Figure 3.9, show different variations, mainly at low temperatures, while McCann et al. [32] show a smooth decrease since the 22 °C, Imran et al. [31] provide an increase of ultimate strength up to 300° followed by a rapid fall. At higher temperatures the curves converge to similar values. Again, the Imran et al. curve will be used in this analysis.

Here, a possible point of lack of explanation from the authors [31], [32] deserves attention, in the following sections, will be drawing the stress-strain curve of the different materials to different temperatures, after applying the equations with the values of yield and ultimate strength given for the steel material. In the works of fire tests on LSF walls, the reductions factors to 600 °C and 700 °C could make the yield strength slightly bigger than the ultimate strength, of course, this is impossible and bring another problem, to get around this problem, when this happens, the value of ultimate strength was considered how equal to yield strength, this modification is the same applied in the

standard EN1993-1-2 to all values above 400 °C.

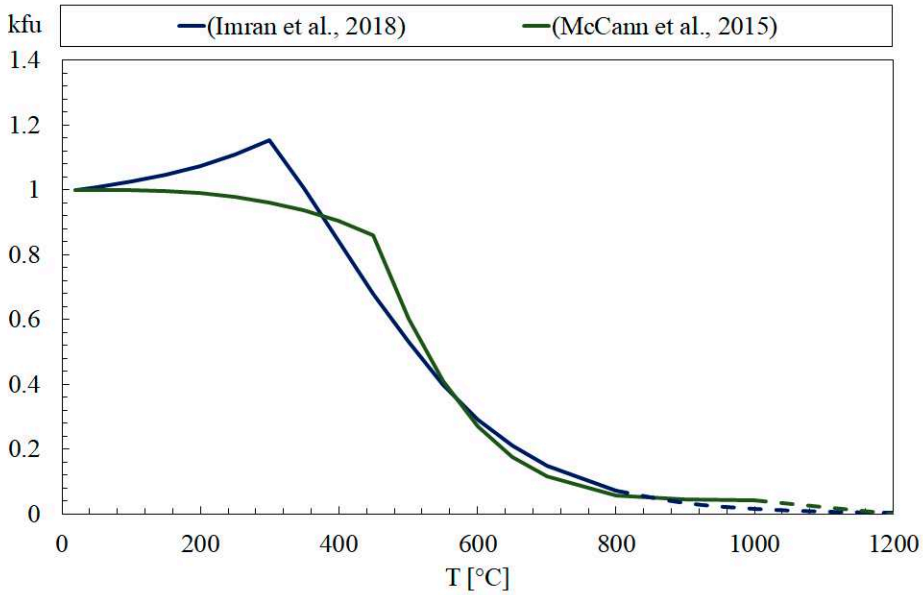

Figure 3.9 - Reduction Factors to Ultimate Strength

Elastic Modulus

Figure 3.10 shows the temperature dependence of the elastic modulus comparison between the standard EN1993-1-2, the average curve between sections circular, rectangular, and square developed in [31], and the reduction factors to rectangular hollow sections from [32]. In this manuscript the Imran et al. [31] curve will be used.

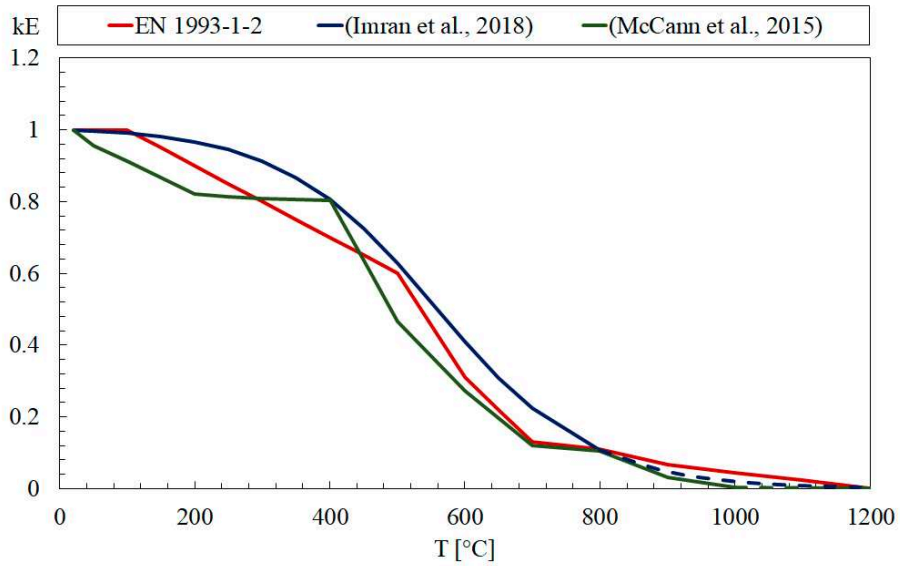

Figure 3.10 - Elastic Modulus Reduction Factor, comparison between standard and research.

Figure 3.11 summarizes the reduction factor for the three mechanical properties used in the development of the stress-strain curve.

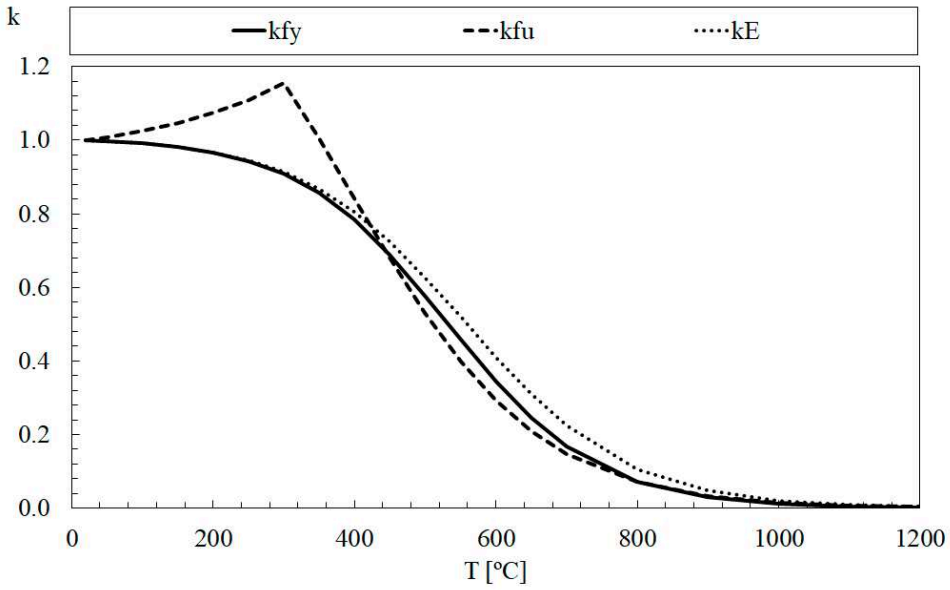

Figure 3.11 - Reduction Factors used for steels.

Stress-Strain Curves

In the latest decades, a large number of proposals to predict a stress-strain curve were

published. The stress-strain curve will be guided by a two-stage equation and parameters from [31] with the assumption of 0.2% proof stress is equal to yield strength because only values of yield strength were provided in the fire test documents. The first stage is defined by equation (7).

Phase 01

$$\varepsilon_T = \frac{f_T}{E_t} + 0.002\left[\frac{f_T}{fy_T}\right]^n \quad for\ f_T < fy_T \tag{7}$$

Where n is the strain hardening exponent component, represents how the microstructure of a metallic material responds to a uniform elastic deformation with equation (8) values:

$$\begin{gathered} n = 7; 20 \le T \le 500\ [°C] \\ n = 7 + 4 * \frac{T - 500}{50}; 500 < T < 700\ [°C] \\ n = 23; T \ge 700\ [°C] \end{gathered} \tag{8}$$

The second stage is defined by the tangent modulus, given by equation (9).

Phase 02

$$\varepsilon_T = \frac{f_T - fy_T}{E_{0.2}} + \alpha\left[\frac{f_T - fy_T}{fu_T - fy_T}\right]^m \quad for\ fy_T < f_T \le fu$$

$$\alpha = -9\ x\ 10 - 5\ T + 0.079; \tag{9}$$

$$m = 3;$$

Where m is the plastic strain hardening represents the behavior in the plastic region and $E_{0.2}$ is the slope of the stress-strain curve at 0.2% proof stress given by equation (10):

$$E_{0.2,T} = \frac{E_T}{1 + 0.002 * n * \left(\frac{E_T}{fy_T}\right)} \quad (10)$$

This curve shows the mechanical behaviour of a steel material. An experimental curve can be obtained by a uniaxial tensile test, which is called *Engineering Stress-strain Curve*, where the stress is calculated by the load divided by the original cross-section area, and the strain is developed by the variation of length divided by the original gauge length. Such measurements don't recognize the variation of the area with load increase, how the "necking" is formed caused when the load hits the ultimate stress.

The *True Stress – True Strain* is calculated by the instantaneous deformed dimensions. This curve is required for accurate numerical modelling of large strain problems such as failure analysis of steel structures [33] under fire, which indicates that is recommended for this investigation. The true stress and strain values are given for the relationship with engineering values for the equations where σ_E is the engineering stress and ε_E is the engineering strain.

$$\sigma = \sigma_E(1 + \varepsilon_E) \text{ ; [MPa]} \quad (11)$$

$$\varepsilon = Ln(1 + \varepsilon_E) \quad (12)$$

Table 3.2 presents values used to create the constitutive law of all steel grades, it's important to emphasize that some information about the properties is not given by authors from the steel C300 used in the studs of specimen 01, which can lead to a level of error.

Table 3.2 - Properties of steels

STEEL GRADE	YIELD STRENGTH [MPa]	ELASTIC MODULUS [MPa]	ULTIMATE STRENGTH [MPa]
C300	339	200.000*	395*
C350	395	201.150	439
C450	457	203.265	517
C500	500*	210.000*	576*

*Value not given by the author, estimated by literature review.

Another piece of information missing by the authors is the shape and steel properties of the tracks, for that, one assumed the steel C500 with nominal values of strength and the geometry of the cross-section was taken as a U-shape that fit well to the studs with a flange of 50mm to all specimens. The initial ultimate strength was estimated by equation (13) given by Gardner & Yun [34] when this property is unknown. That approximation has a minor influence on the final result because the track is not the fundamental element from the LSF for the load support. Thermal expansion is also included, but only applied to the studs, in thermo mechanic simulation.

$$\frac{fu}{fy} = 1 + \left(\frac{130}{fy}\right)^{1.4} \tag{13}$$

The steel C300 used in studs in specimens 04 and 05 is presented in Figure 3.12, C350 to studs of specimen 01 is in Figure 3.13, and specimens 02, 03, and 06 have the C450 from Figure 3.14. All specimens have the same standard C500 as the track material, see Figure 3.15.

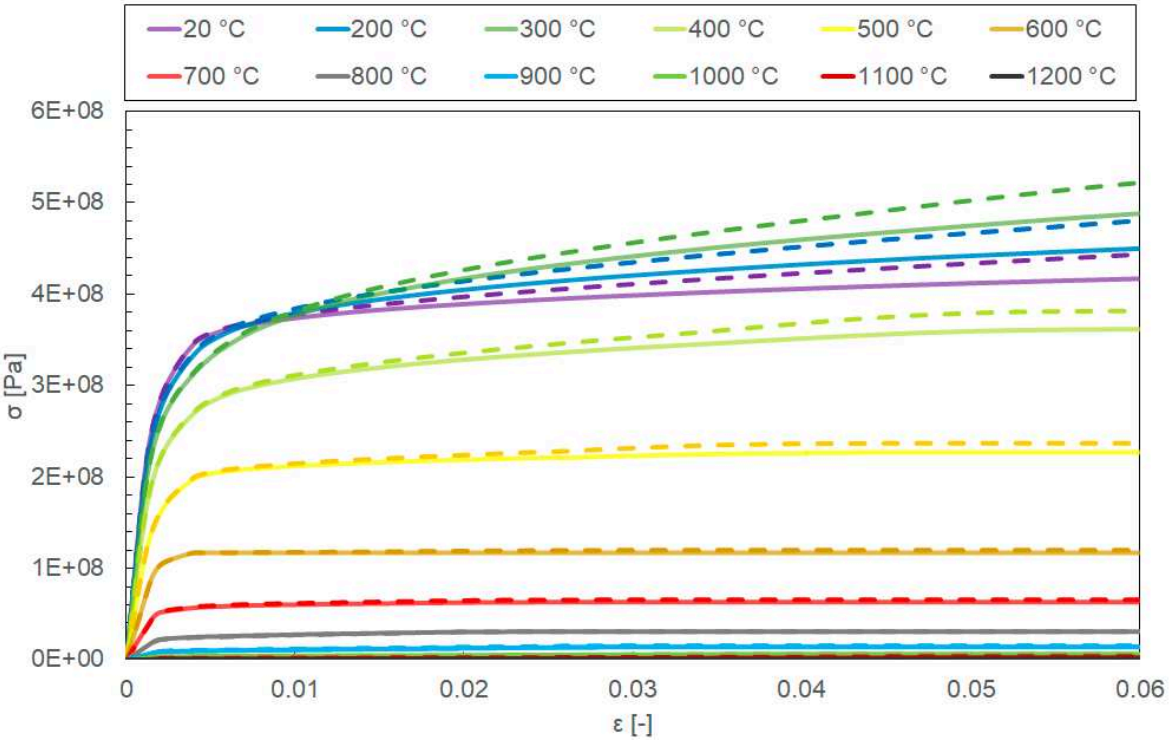

Figure 3.12 – Constutive Law C300

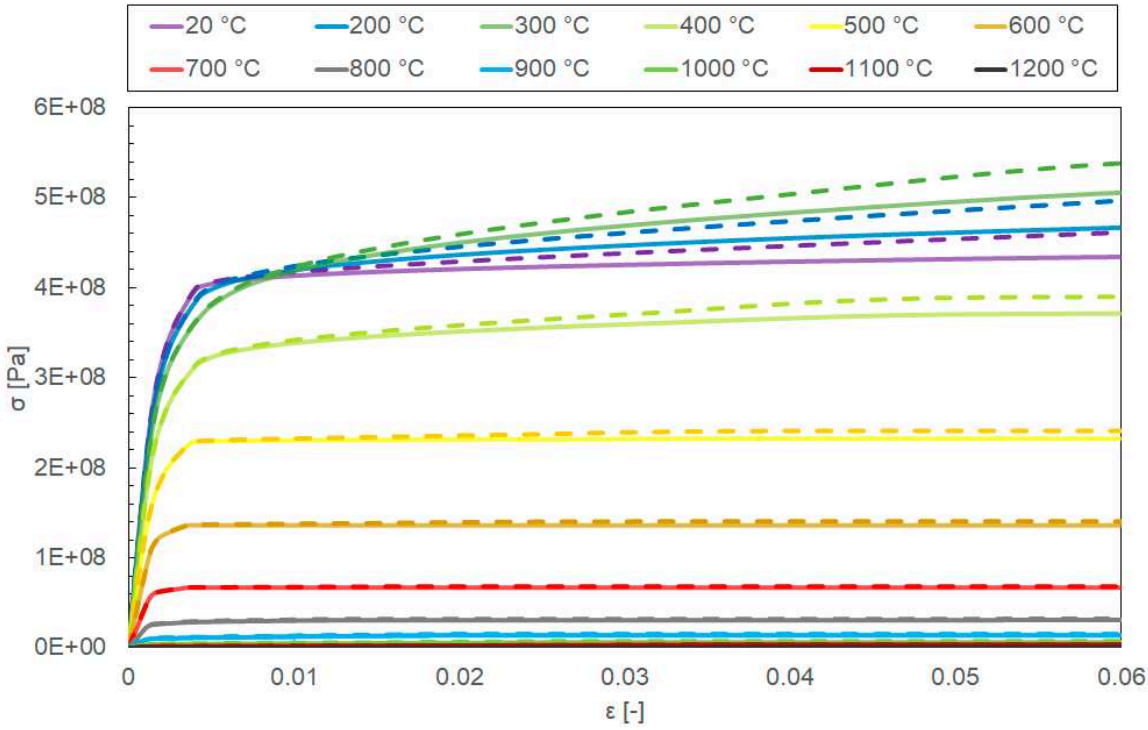

Figure 3.13 - Constutive Law C350

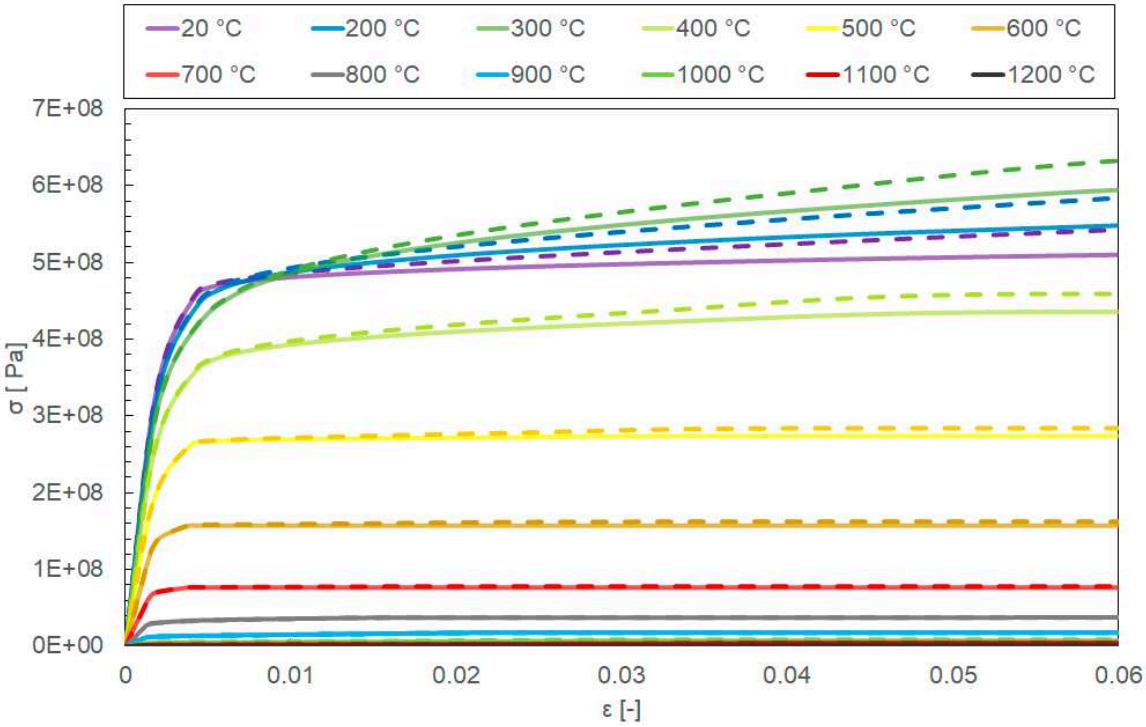

Figure 3.14 - Constutive Law C450

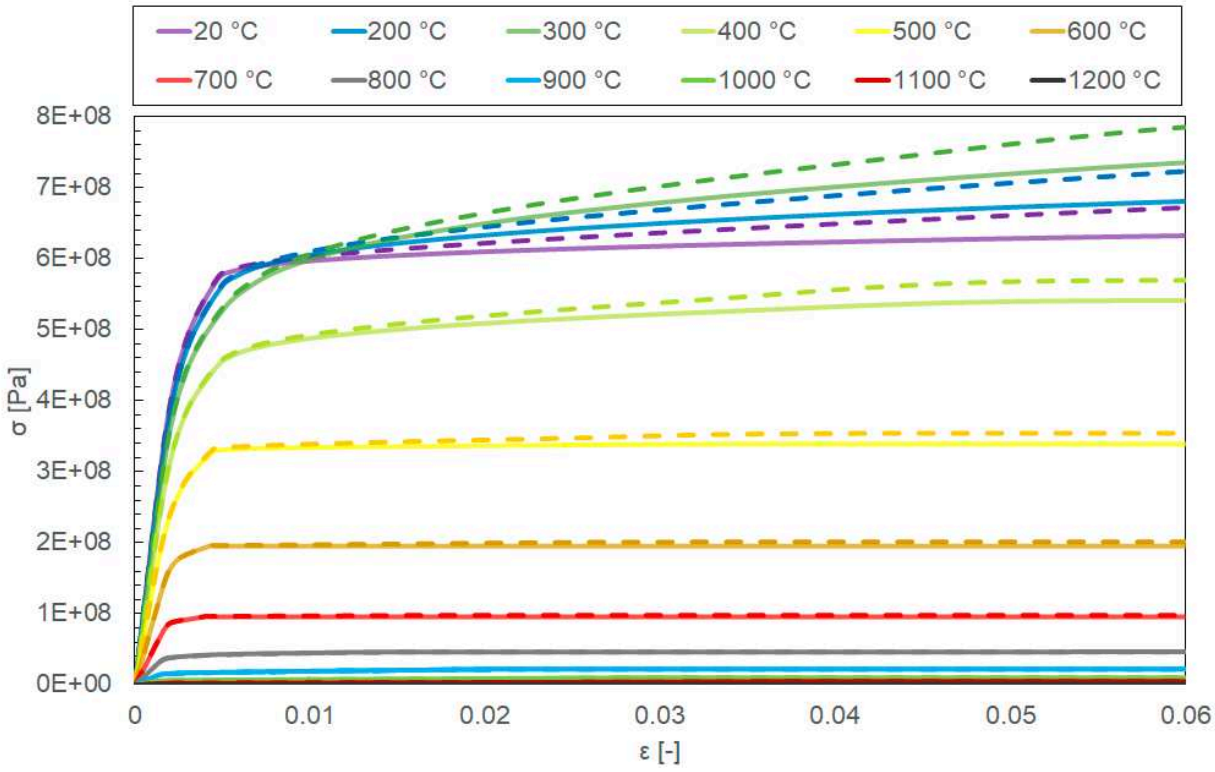

Figure 3.15 - Constutive Law C500

3.8. Newton-Raphson Method

The thermo mechanical simulation is classified to be a GMNIA analysis. To solve this type of analysis, one needs to consider different solution methods. In Newton's method, the incremental loading is represented as follows: The external load vector F^{ext} is incrementally augmented from 0 to achieve a desired value F*. For the sake of simplification, assuming that the direction of F^{*} remains constant throughout the analysis while only its magnitude changes, we can denote F^{ext}= q = a known quantity. By introducing a scalar parameter λ, we can control the gradual increase or decrease of the external load vector. Consequently, the equilibrium system of equations can be expressed as (14) [35].

$$R(u) = F^{int}(u) - F^{ext} \Rightarrow R(u) = F^{int}(u) - \lambda F^{ext} = 0 \quad (14)$$

Where R(u) is the residual vector and changing the magnitude of λ the load is increased or decreased. At each increment, of the parameter λ, the equation (14) is solved to determine u (deformed configuration). Assuming that the last converged solution is u_0, λ_0, the load increment is calculated using equation (15).

$$\lambda' = \lambda_0 + \Delta\lambda \quad (15)$$

Therefore, the displacements are given by equation (16).

$$u' = u_0 + \Delta u \quad (16)$$

So, equation 14 is upgraded to (17).

$$R(u') = R(u_0 + \Delta u) = 0 \Rightarrow F^{int}(u_0 + \Delta u) - (\lambda_0 + \Delta\lambda)F^{ext} = 0 \quad (17)$$

But, $F^{int}(u_0 + \Delta u)$ can be expressed in terms of $F^{int}(u_0)$ by a Taylor series expansion as:

$$F^{int}(u_0 + \Delta u) = F^{int}(u_0) + \left[\frac{\partial F(u)}{\partial u}\right] * \Delta u = F^{int}(u_0) + [K_T]_{u_0} * \Delta u \quad (18)$$

In which, $[K_T] = \left[\frac{\partial F(u)}{\partial u}\right]$ is the Jacobian matrix, also known as the Tangential Stiffness Matrix [35]. Combining equations (16) and (17) is possible to solve Δu using equation (19).

$$\begin{aligned} & F^{int}(u_0) + [K_T]_{u_0} * \Delta u - -(\lambda_0 + \Delta\lambda)F^{ext} = 0 \\ & = F^{int}(u_0) - \lambda_0 F^{ext} + [K_T]_{u_0} * \Delta u - \Delta\lambda F^{ext} \Rightarrow \Delta u = [K_T]_{u_0}^{-1} * (\Delta\lambda F^{ext}) \end{aligned} \quad (19)$$

Using equation (19), one can compute the displacement correction Δu. However, despite assuming that Δu would satisfy equation (17), the linear approximation in the Taylor expansion hinders the immediate attainment of equilibrium. Consequently, if we assess the system (17) at the new point (u_0, λ_0), we will obtain a residual vector $R'(u')$ that is not equal to zero. By utilizing this residual vector, we can determine a new displacement correction δu through the following equation:

$$\delta u = [K_T]_{u'}^{-1} * R'(u') \quad (20)$$

Commercial finite element analysis software relies heavily on the quadratic convergence rate of Newton's Method to achieve rapid convergence within just a few iterations. Large systems of nonlinear equations are often solved using Newton's Method because of its fast convergence,

although every attempt increases computational time. Despite these advantages, however, there exists one considerable drawback - it struggles to follow an "equilibrium" path with adequate precision when encountering zero tangent stiffness.

This issue arises from Newton-Raphson Method and its constraints on changing λ monotonically with each incrementing value This forces us to adjust our loading patterns based on whether we consider limit points as local maximums or minimums in u-λ space while disregarding saddle points entirely.

A proper understanding and visual illustration of this challenge can be gleaned from Figure 3.16.

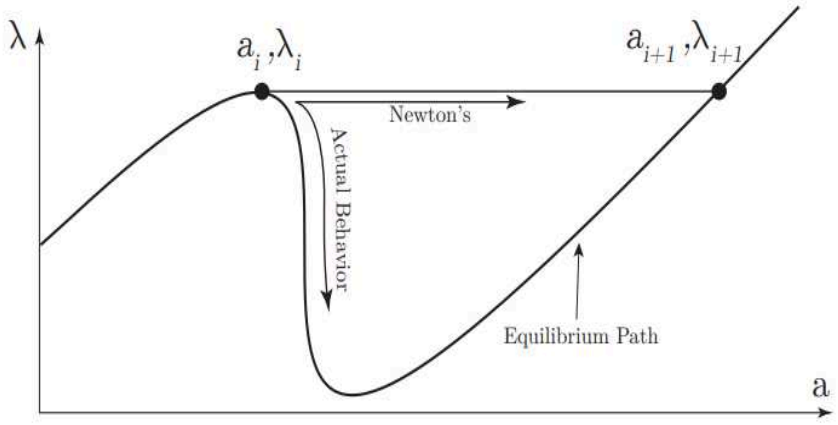

Figure 3.16 - Newton-Raphson method fails to predict the equilibrium path. Adapted from [35]

Within Ansys, there are three different methods for calculating the norm: infinite norm, L1 norm, and L2 norm. However, for all simulations, the default L2 norm is used. In the L2 norm, the square root of the sum of the squared values of the terms is considered: $|R| = (\Sigma R_i^2)^{1/2}$. The reference value (Rref) is determined based on the norm of the external force, $|F^{ext}|$, except for degrees of freedom (DOF) with displacement constraints, where the reference is taken as $|F^{int}|$. In certain cases, Ansys may assume a minimum value for Rref, which is selected as 1.0 for all simulations [36].

To the thermomechanical solution, default values of tolerance to Force and Momentum were used, which is $1x10^{-3}$. The reference values to force and moment were 1 N and 1 Nm. The incremental solution is running over true time increments, with an update for the thermal and mechanical load, using a normal and maximum time increment of 60 seconds with a minimum of 0.01 seconds.

3.9. Arc Length Method

The Arc-Length was used to determine the load capacity of the LSF walls in room temperature. It is a very useful method when encountering non-linear systems of equations, an exceptionally effective approach is to address cases where the problem exhibits one or more critical points. In the context of a basic mechanical loading-unloading problem, a critical point can be defined as the juncture where the loaded object becomes unable to withstand additional external forces, leading to a state of instability.

The Arc-Length method uses the same principles as the Newton method, for that the same equilibrium (14) can be applied using the variation of u and λ from (15) and (16) to a new residual vector given by [35].

$$R(u', \lambda') = F^{int}(u_0 + \Delta u) - (\lambda_0 + \Delta\lambda)F^{ext} = 0 \quad (21)$$

If (21) is satisfied for the variables u_0, Δu, λ_0, Δλ the solution for the current iteration is considered complete, and the subsequent iteration commences. However, it is important to note that this sequential progression is not always feasible. Consequently, to rectify this, the necessary corrections must be incorporated, that is, adding Δu and δλ for a new equation (22).

$$R(u'', \lambda'') = F^{int}(u_0 + \Delta u + \delta u) - (\lambda_0 + \Delta\lambda + \delta\lambda)F^{ext} = 0 \quad (22)$$

Using Taylor expansion and keeping only the linear terms, the equation results in (23) [29].

$$-R(u', \lambda') = [K_T]_{u_0+\Delta u} * \delta u - \delta\lambda F^{ext} \quad (23)$$

Nevertheless, it should be noted that the equation in question entails a greater number of unknown variables compared to the available equations. Consequently, this system cannot be solved directly. To address such cases, various approaches can be employed. However, the focus will be on the method employed by Ansys. In this particular method, the value of u is determined using equation (24).

$$\delta u = \delta\overline{u} + \delta\lambda * \delta u_t \quad (24)$$

To determine δλ, the software uses the norm of a vector Δl, which represents the distance between the previous equilibrium point and the next point to be solved. The range of vector Δl is pre-determined and varies within a maximum and minimum value. A graphical representation of this method can be observed in Figure 3.17. The size of the arc is determined by the norm of vector Δl and remains constant throughout the substeps that the solver executes to progress towards the next equilibrium point (i+1). It is important to note that the norms of Δl, and subsequent vectors are numerically equal; however, the vectors themselves differ since each substep corrects the values of u and λ by δu and δλ. The solver has the flexibility to traverse any point within the circle's radius, and if a solution cannot be found, the software adjusts l based on the predefined maximum and minimum values.

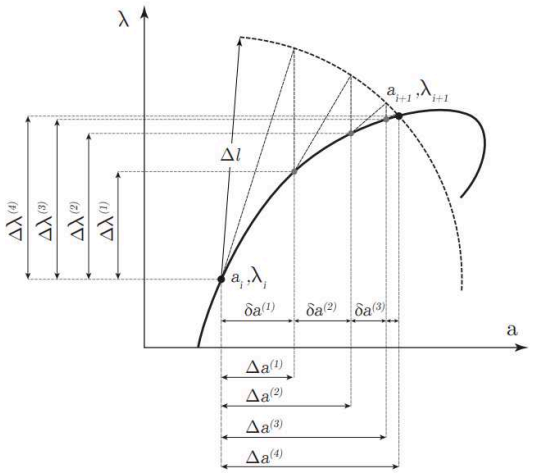

Figure 3.17 - Arc-Length method in a graphical representation. Adapted from [35].

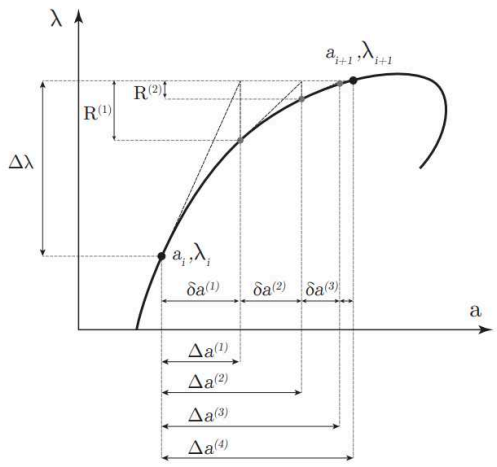

Figure 3.18 - Newton-Raphson method in a graphical representation. Adapted from [35].

A clear distinction between the arc-length and Newton methods is evident when comparing Figure 3.17 with Figure 3.18. In the arc-length method, there are corrections for both the load and displacement, whereas, in the Newton method, these corrections do not occur simultaneously. For that advantage the arc-length method was chosen for the mechanical simulations.

To enhance the quality of the simulations, certain modifications were made to the default maximum and minimum arc values. The previous values of 25 and 0.1 [37], were adjusted to 10 and 0.01, respectively, allowing for a more gradual progression. The tolerance, ε, was established as 0.1 (10%) and a reference value of $1x10^{-3}$ was adopted for all simulations. Additionally, the time at the end of the simulation was defined as 100000 [N], utilizing 1000 substeps. This corresponds to an arc with an incremental load ranging from a minimum of 1 [N] to a maximum of 100 [N]. Four distinct loads were applied, resulting in a minimum increment of 4 [N] and a maximum of 400 [N].

4 Numerical Validation

To validate the numerical models and execute the parametric study, a four-step numerical simulation method is presented. The first step is made by a linear elastic buckling analysis to determine the critical load and main instability mode shape of the LSF structure. This instability mode is then used to define the imperfection of the structure. The second step is defined by the load-bearing capacity of the LSF wall at room temperature, which is determined through a Geometric and Material Non-Linear Imperfection Analysis (GMNIA), neglecting the mechanical resistance of the gypsum protection layers and insulation (glass fiber). The maximum load-bearing capacity is compared and validated from experiments. The third step is defined by the non-linear thermal analysis, incorporating all non-linear thermal properties to predict the thermal effects of a fire on the LSF structure. The hybrid solution method is used, which requires an additional temperature measurement to track the evolution of the bulk temperature in the cavity and select appropriate heat flow coefficients. This measurement is crucial to capture all major events that occur during experimental tests such as cracks and ignition of combustible materials (when included). Finally, the thermal model is validated with experimental results, comparing the temperature evolution in various parts of the LSF structure, including the Hot Flange (HF), Web (WEB), Cold Flange (CF), and the unexposed surface. To demonstrate the accuracy of the model, the root mean square error is determined for the temperature evolution over time from several measured points, and the relative error is determined concerning the fire resistance. The fourth step used a GMNIA analysis is used to predict the ability to support the load during the fire. Several load levels have been used to determine the effect of this parameter.

4.1. Element and meshes

The finite element method (FEM) has been used to evaluate the thermal and mechanical resistance of the LSF wall assemblies.

Shell finite elements are commonly used in Finite Element Analysis to cold-formed steel studs due to their advantages, such as modified integration and better convergence, while still providing sufficient degrees of freedom to simulate the nonlinear behaviour of steel studs. Before modelling, the mesh size was slightly adjusted based on convergence and the required precision. However, shell elements are not, usually, appropriate for displaying the temperature gradient along the thickness direction at elevated temperatures, but this element can track the temperature gradient due to the existence of layers. While this is not a critical issue for thin-walled steel studs, it becomes problematic for thicker fire-protective boards, such as gypsum plasterboards. To address this modification of physical dimensions, 3D solid finite elements were used to model plasterboards and insulation materials under fire conditions. Furthermore, the mesh size for these wall components was varied, with higher mesh density only applied to areas that have significant interaction with steel studs.

In this research the software ANSYS APDL 2021 was used for mechanical and thermal analysis, the shell finite element chosen was “Shell 181” in mechanical analysis and turned to “Shell 131” for thermal analysis. The 3D solid finite element used in the thermal analysis is the “Solid 70” from Ansys and the corresponding mechanical solid element was deleted in the thermomechanical analysis. The numerical model uses thermal analysis in a decoupled process from structural analysis for the calculation of the fire resistance. This means that there is no temperature modification produced by the increased deformation of the LSF structure.

The shell finite element is a finite element type that is primarily used for the analysis of thin-walled structures. It is particularly suitable for modelling structures such as plates, shells, and composite laminates, where the thickness is small compared to the other dimensions. This element is based on the classical thin plate theory, assuming that the displacement variations through the thickness are negligible compared to the in-plane displacements. The shell element has six degrees of freedom at each node, including translations in the x, y, and z directions, as well as rotations about

the x, y, and z axes. These degrees of freedom allow for the representation of both membrane and the bending behaviour of the shell [38]. The interpolating functions are linear and the integration scheme is based on the GAUSS method.

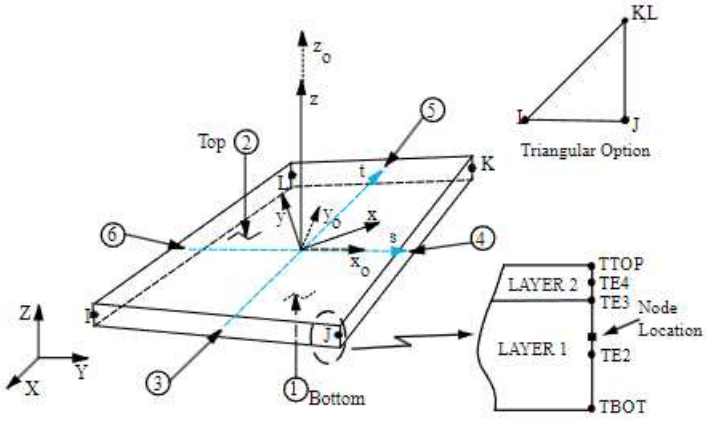

Figure 4.1 - Shell 131 geometry. Modified from [38].

The solid finite element is a three-dimensional solid element widely used for structural analysis. It is a higher-order, 10-node tetrahedral element that provides accurate results for a variety of solid structures. The element is based on the isoparametric formulation, which allows for efficient and accurate representation of complex geometries. The solid element has three degrees of freedom at each node, including translations in the x, y, and z directions. These degrees of freedom allow for the representation of both translational and rotational displacements in three-dimensional space [39].

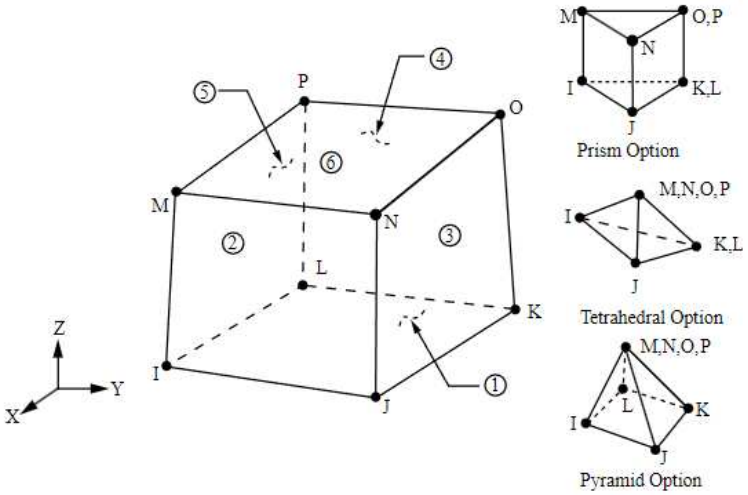

Figure 4.2 - SOLID70 geometry. Modified from [39].

4.2. Mechanical finite element model

The experimental tests were conducted following the general requirements for fire tests outlined in EN 1363-1 [40]. During the load-bearing fire tests, a constant load was applied to the geometric centroid of the steel studs by a hydraulic actuator as shown in Figure 4.3, using loading plates at the bottom end of the wall. To prevent any additional bending moment in the fire test, an interface beam was used to distribute the load over the entire wall.

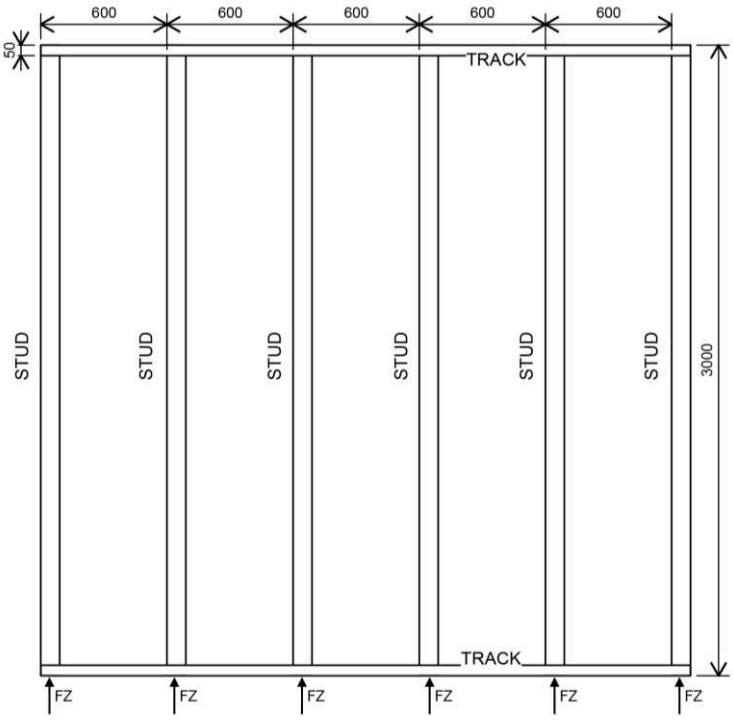

Figure 4.3 - LSF wall dimensions and direction of applied load.

The arrangement of the six studs is made by disposing of them 600 mm far from each other, with 3 meters of height, without noggings. The studs were screwed in both extremities (bottom and top) using the tracks made by U-shape, C500 steel grade with 1.95 mm thickness to hollow sections specimens and 1.15 mm thickness to open shape studs specimens. The connections are modelled by superposition of both steel parts (studs and tracks), using double thickness, sharing the same nodes.

To be as close as possible to real tests, a few restrictions were applied to the model. In the top track, the web surface is considered partially restrained, and the UX (horizontal), UY (depth), and UZ (vertical) displacement is considered as zero and no rotational restriction. The horizontal restriction (UX=0) is applied to the screw positions fixing the plasterboard layers to studs. The model and boundary conditions are depicted in Figure 4.4.

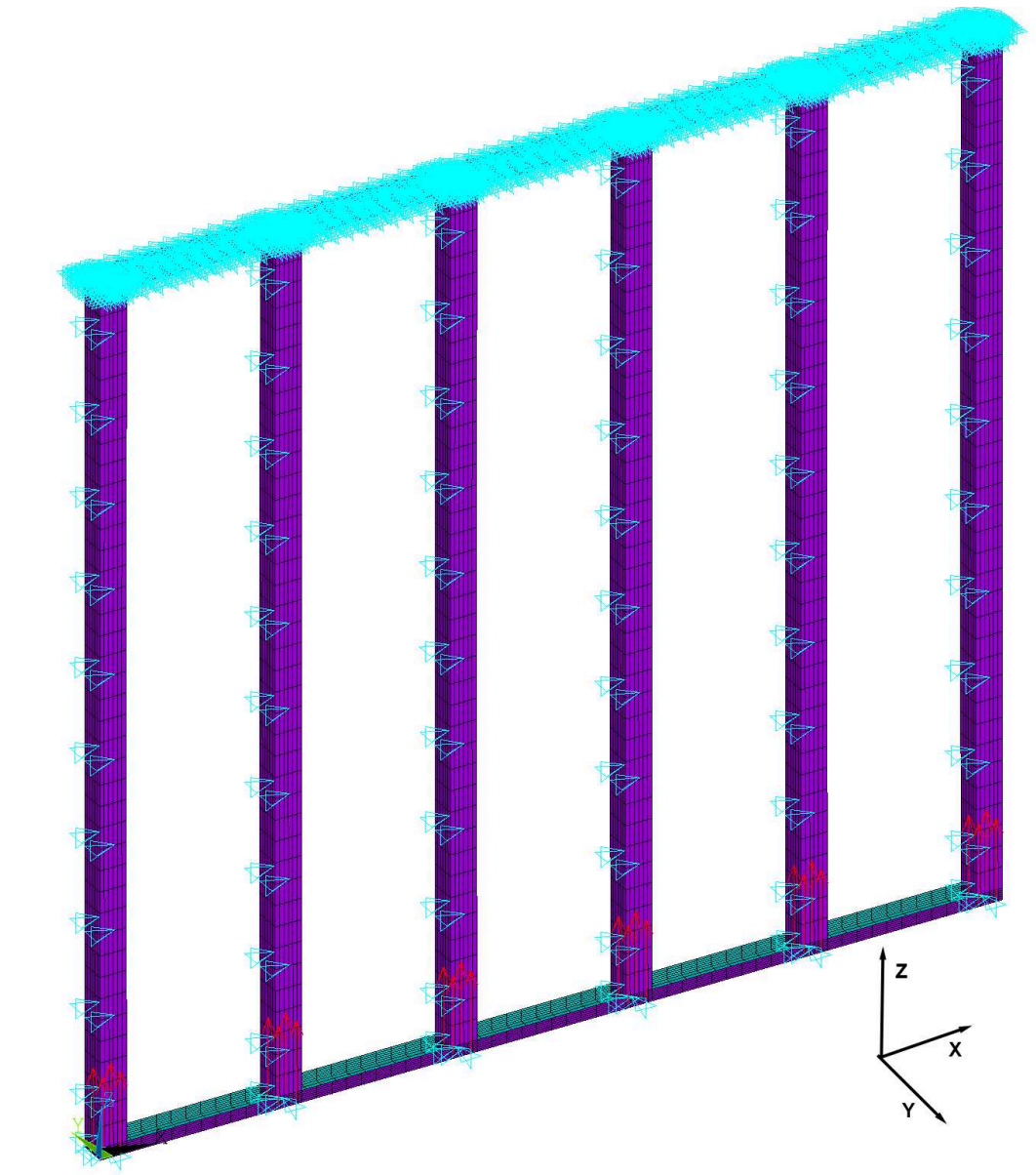

Figure 4.4 - Mechanical model with movement restriction, specimen 01.

In detailed Figure 4.5, the colours of elements are representing the thickness of the different sections used for the shell finite element. For each stud the load was applied in 4 nodes, using the interface beam (web of the track with extra thickness of 30 mm) to distribute the load over the track and avoid concentration of stress. An additional restrain (UY=UX =0) was given to the central node of the stud, to prevent forces from moving out of plane.

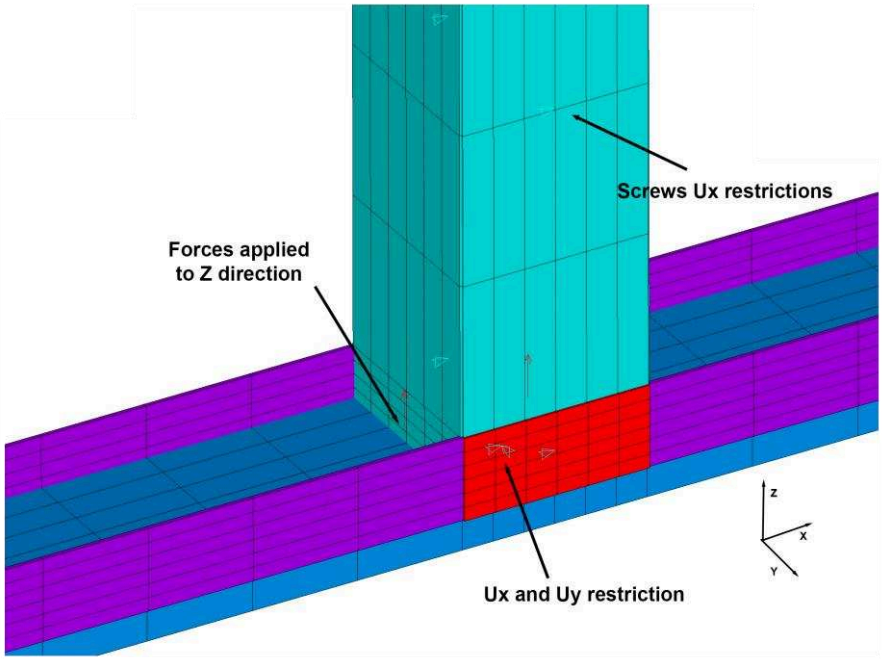

Figure 4.5 - Detail of shell thickness and boundary conditions in mechanical model, Specimen 02.

In the physical model, the elements are fixed by screws. To simplify the analysis, the screws are modelled as in plane restrain in the horizontal direction (UX=0) for the screw position, using the two connecting surfaces overlapped. The region works with double thickness and receives the properties from the strongest material between stud and track, assuming that the screw should stronger than flanges, this connection reduces your load capacity with the increase of temperature [41].

4.3. Initial Imperfections

Schafer and Pekoz [42] presented two categories of geometric imperfections (see Figure 4.6) and provide a simple rule to define the maximum local geometric imperfections (type 1) in cold-formed steels given by equation (25) where W is the depth of the web in millimeters. For studs subject to global buckling, a global imperfection with a maximum amplitude of L/1000 has been applied where L is the length of free buckling distance of the stud.

$$d1 = 0.006 * \mathrm{W} \tag{25}$$

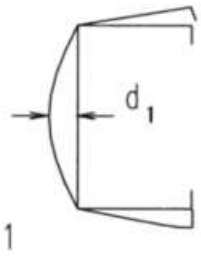

Figure 4.6 – Geometric imperfections, type 1 on the left and type 2 on the right. Adapted from [42]

The adequate instability mode will be used to apply the geometric imperfections. For that, a three-dimensional linear elastic eigen buckling analysis was solved using the Block Lanczos extraction method. From the fire tests, a global buckling failure mode was identified for specimens 01, 02 and 06, while a local web buckling failure mode was identified for specimens 03 to 05. Both instability modes are depicted in Figure 4.7 and Figure 4.8.

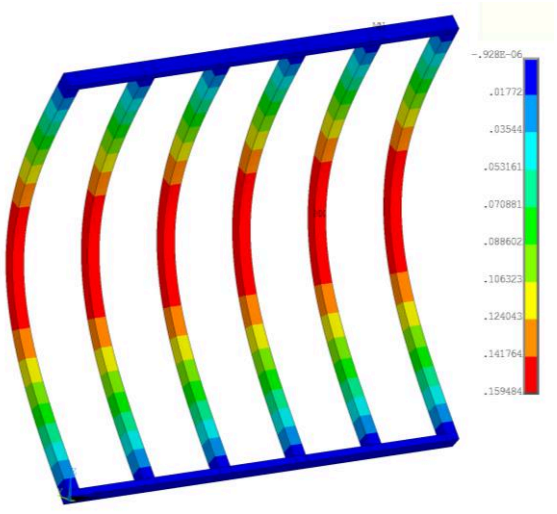

Figure 4.7 - Global mode of instability and displacement in the X-axis of specimen 01 to initial imperfection.

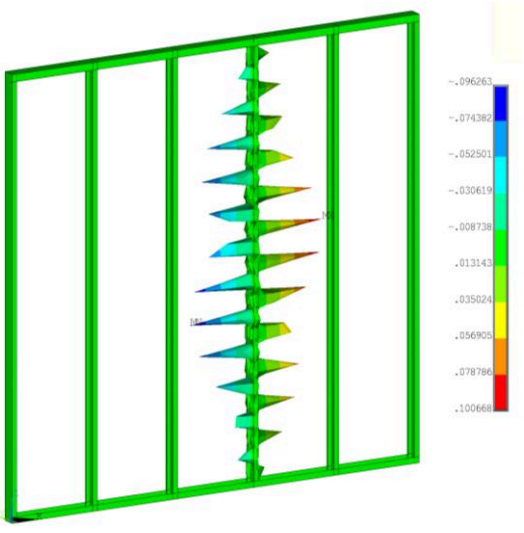

Figure 4.8 - Local buckling mode of instability and displacement in the Y-axis of specimen 04 to initial imperfection.

4.4. Mechanical Validation at Room Temperature.

The Arc-length method was used to estimate the load-bearing capacity at room temperature, using the convergence criterion based on displacement with a tolerance of 5% and a reference value of 10^{-3} m. The load increment was defined as 100 [N] with a possible change between 10 and 1000 [N].

The failure load for specimen 01 was found to be 192 kN, very similar to 187 kN, found in the room temperature experimental test specimen. Figure 4.9 shows the comparison between the experimental test and numerical test from Tao et al. [22] and two numerical analyses from Piloto et al. [19]. The initial part of the experimental curve may be explained by any kind of loading plate slippage or by the initial slackness in the test specimen.

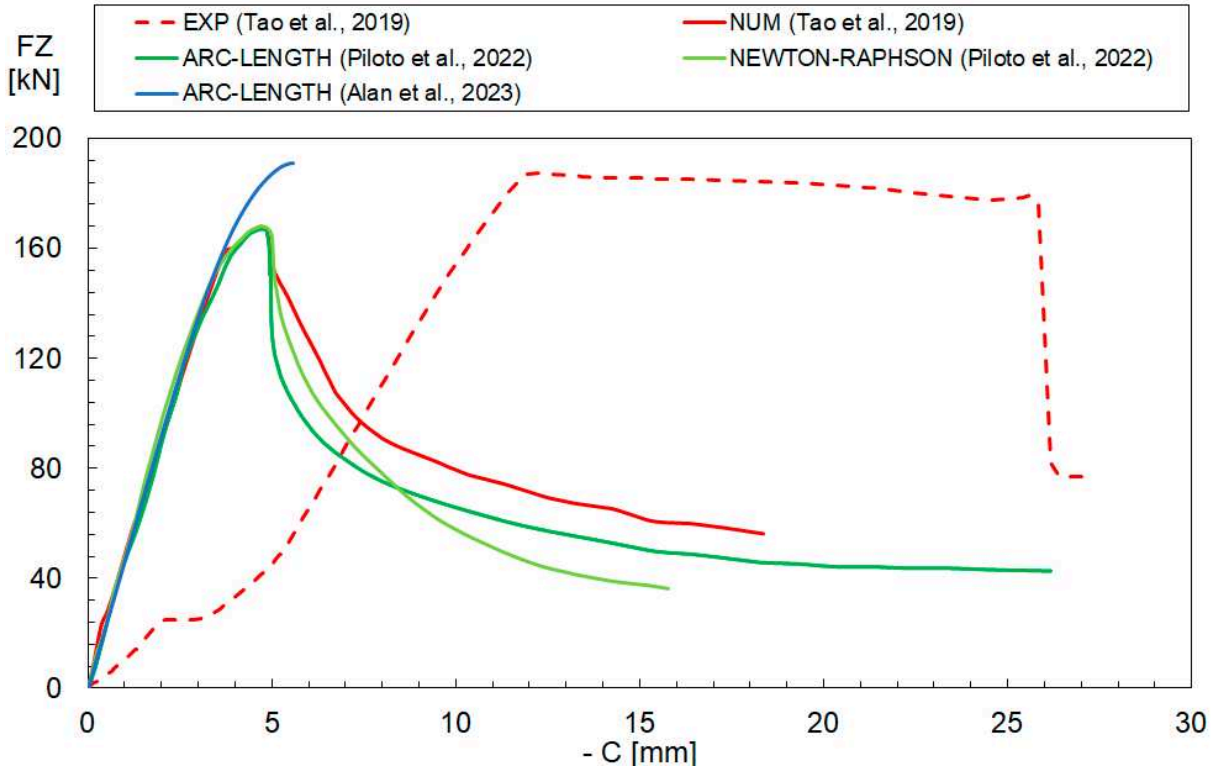

Figure 4.9 – Experimental and numerical results at room temperature for specimen 01. [19], [22].

The maximum load-bearing capacity from specimen 02 was 220 kN for each stud in LSF the structure. This value was determined by the arc-length method, and the experimental maximum load was 193 kN [9]. This value is considered to be underestimated, and Tao et al. [9] considered a value of 200 kN to determine the load levels. The numeric simulations developed by Tao el al. [20] reached a maximum load of 208 kN. The same maximum load has been considered to specimen 06.

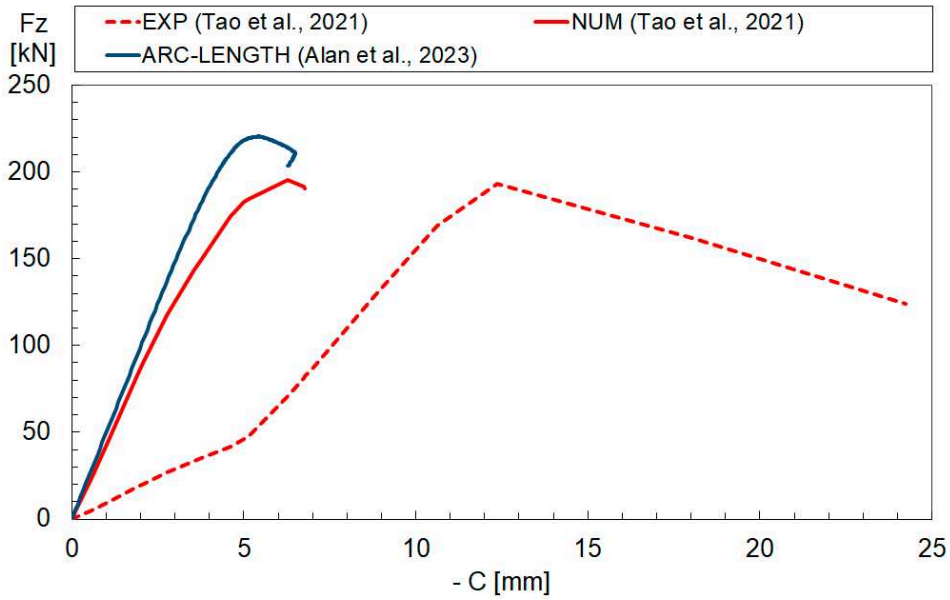

Figure 4.10 - Experimental and numerical results at room temperature for specimen 02. [9], [20].

For specimen 03, Tao et al. [9] do not provide the curves of load versus displacement, for that, the unique comparison is the value of max load applied. To this specimen, three different initial imperfections were tested to find a better agreement with the experimental tests. The initial imperfection of w/250 (where w is the depth of stud) reached a value of 180 kN per stud, closest to 182 kN from Tao et al. [9]. Figure 4.11 shows the comparison between different initial imperfections, experimental tests and numerical simulations from the author.

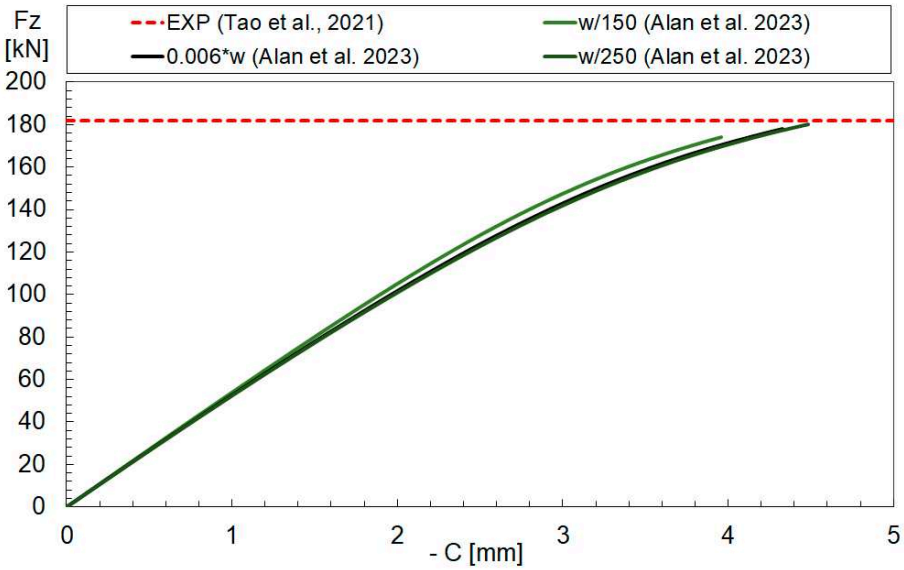

Figure 4.11 - - Experimental and numerical results at room temperature for specimen 03. [9].

Specimens 04 and 05 have the same LSF structure, with the difference that specimen 05 was a double protective layer of gypsum plasterboard. The LSF structure presents the same load-bearing capacity, as determined by the experimental tests developed by Ariyanayagam & Mahendran [18] at room temperature, which is 40 kN.

Table 4.1 summarizes the results of this section, which may be considered a good agreement between numerical simulations and experimental results. The parametric study is based on the proposed load ratios, and the maximum loads considered in the parametric study were based on the numerical simulations, because the experimental tests had occurrences that are impossible to replicate in simulation, such as slippage.

Table 4.1 - Details of ambient temperature load capacity.

Specimen ID	Experimental test load capacity [kN]	Numerical load capacity [kN]	Difference [%]	Load considered [kN]
S01	187	192	2.67	192
S02	193	220	13.99	220
S03	182	180	-1.10	180
S04	40	40	0.00	40
S05	40	40	0.00	40
S06	193	220	13.99	220

4.5. Thermal Models

A good thermal model is essential for conducting an accurate and reliable thermomechanical analysis. The hybrid thermal model has been selected based on previous investigations [19]. This hybrid model considers the three heat transfer modes in the analysis of LSF walls, and also implicitly considers the simulation of the major ablation events during tests.

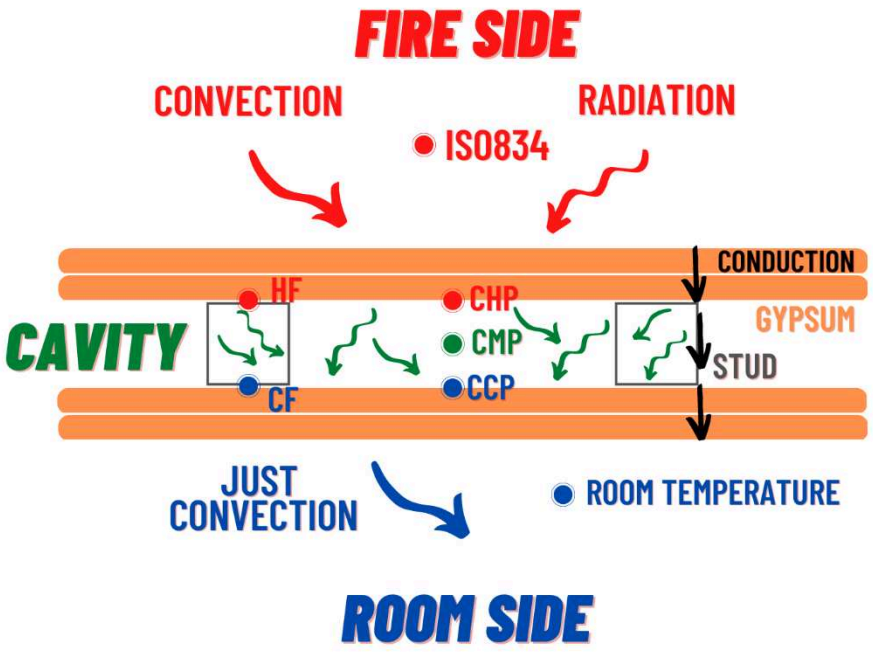

Figure 4.12 - Diagram of the hybrid model.

Figure 4.12 shows an example of heat transfer through a wall made with hollow section studs without cavity insulation. The heat flow reaches uniformly the external side of the most exposed plasterboard by convection and radiation. The heat flow goes through the wall thickness, either using insulation material in the cavity or no material in this region (void cavity). For the case of insulation material, the model only considers heat flow by conduction, while for the case of a void cavity, the heat flow by convection and radiation is assumed. The heat flow in the unexposed surface is considered by convection, using the appropriate coefficient to include the radiation effect. The best model to accurately predict the thermal behaviour of the void cavity LSF wall under fire includes the heat flow by convection and radiation in this cavity region. This model requires the calculation or the definition of the bulk temperature inside the cavity. The difference between the calculated and the definition might be significant, because the definition may include important events expected during the experimental tests, previously developed with typical fire protection materials. The definition can be obtained by experimental measurement (requires extra plate thermocouples in the cavity region) or by the average temperature measurements between the HF (Hot Flange) and CF (Cold Flange). The value of the convection coefficient of the cavity is taken as 17 W/m2K and the flame emissivity value on the fire side is equal to 1. The convection coefficient represents the average value between the exposed and the unexposed coefficients. This value may be justified by the loss of integrity in the most exposed plasterboards during the fire test. In the beginning, the convection coefficients may be similar to 9 (full integrity), but at the end may be similar to 25, assuming the complete loss of integrity.

The thermal models for the thermal analysis used the same steel geometry of studs and tracks made of shell finite elements but for the study of the temperature gradient between element nodes, the load influence is not required, for that, the studs are exposed to thermal analysis without any load.

All of 16mm gypsum layers are modelled as rectangular plates, using the solid finite element Solid 70 from Ansys, with the standard setup, these plates cover the wall area as shown in Figure

4.13. In the numeric model, the contact between the gypsum layers and the interface gypsum-steel are considered as perfect contact. In reality, that kind of contact is really hard to obtain.

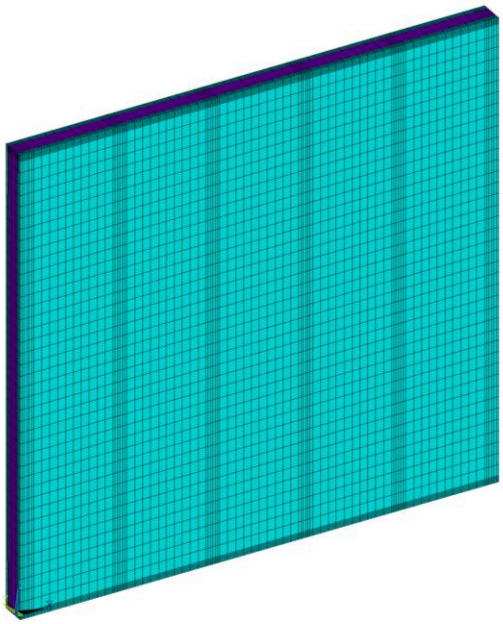

Figure 4.13 - External view of the thermal model, specimen 01.

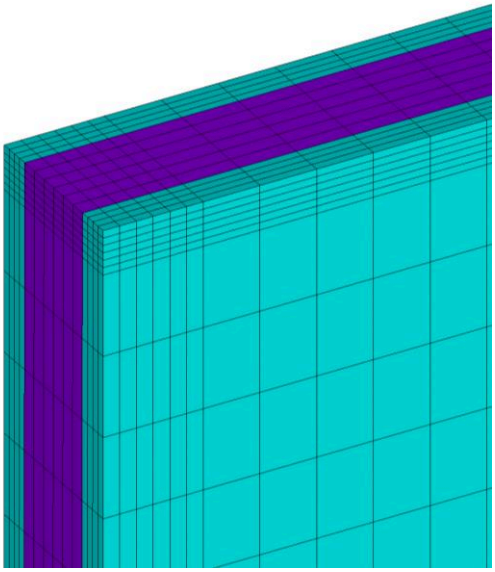

Figure 4.14 - Detail showing the difference between steel and gypsum elements, specimen 01.

The detail of interface gypsum-steel can be observed in Figure 4.14, the image shows one of the model borders, where the studs meet the track (purple shell finite element) and both are covered by the gypsum layer (blue solid finite element). Note the high refining of the mesh in the area of the studs, in these places, the thermal bridge by conduction is the main mode and biggest influence in the heat transfer.

To achieve a good result in the thermal validation the set of boundary conditions needs to be in accordance with the experimental fire tests to accurately predict the temperature distribution and heat transfer in the LSF wall system.

Specimens 01, 02 and 03 have the particularity of being made of hollow section without wall

cavity insulation, this kind of section presents radiation and convection in the wall cavity but also in the stud cavity.

The convection was applied to the fireside surface with a coefficient of 25 W/m²K and bulk temperature evolution with time, following the furnace fire curve. The radiation is also applied to the fireside surface with an emissivity equal a 1. In the unexposed surface, only convection is applied, using the coefficient of 9 W/m²K to include the radiation effect, assuming a constant bulk temperature of 20 °C. Essentially, it's incorrect because the temperature in the room can slighter increase over time, but it doesn't have this kind of measurement and have a minor influence. Figure 4.15 shows the convective heat transfer coefficient through the LSF wall.

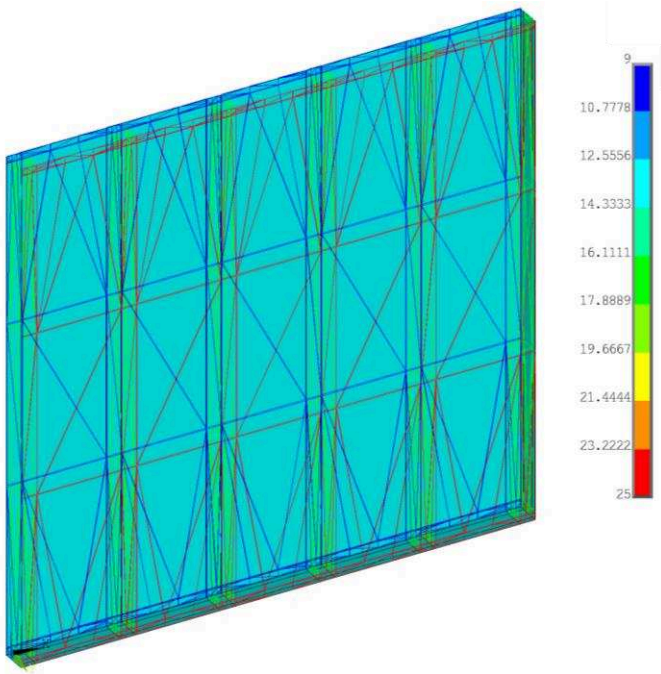

Figure 4.15 - Convective coefficients scheme applied to surfaces of hollow section specimens without wall cavity insulation.

Inside the cavity, each area must be evaluated separately, only the elements from gypsum or steel that are in contact with the empty cavity have convection and radiation. The measurement of cavity temperature can be complicated by its location, and most authors of fire tests don't have a

sensor positioned for this value. In order to represent the evolution of temperature in a cavity over time, this model will consider the mean value between the hot and cold flange temperatures for each time step [19], obtained from thermocouples measurement during the in all fire tests. The value of the convection heat transfer coefficient of the cavity is taken as 17 W/m²K. The radiation was applied to the same elements with an emissivity of 1. The convection coefficient is justified from the appearance of cracks in the plasterboard after a period of fire exposure, allowing the fire to enter the cavity. Another possible solution is creating a temperature-dependent emissivity coefficient evaluating the time that the cracks appear [20].

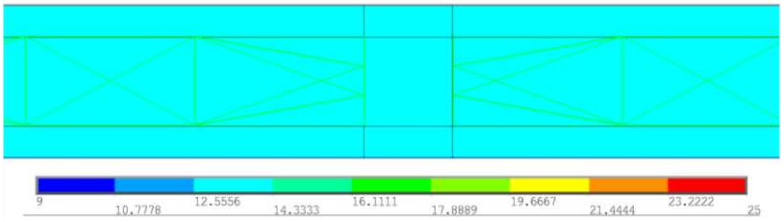

Figure 4.16 – Upper view detail of the scheme applied to surfaces in hollow section specimens without cavity insulation.

Figure 4.16 shows the upper view from the LSF wall, representing the convective coefficient. Please note the absence of convection inside the tube, the blue and red thin line, represents the exposed convection coefficient and the coefficient in the unexposed surface and exposed surface respectively. Inside the cavity region, the green line in the gypsum and track cavity surfaces.

The same upper view (Figure 4.17), represents the radiation inside the wall cavity and in the exposed surface.

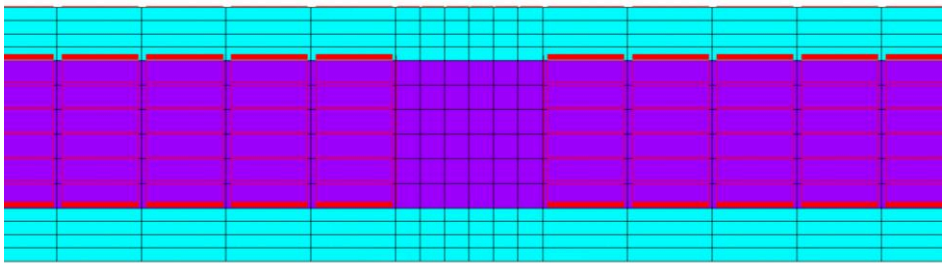

Figure 4.17 - Radiation applied to elements hollow section specimens without cavity insulation.

The same external boundary conditions were applied to specimens 04 and 05, but in the cavity region some differences were applied. The open steel section, has convection and radiation in the internal surfaces exposed to the empty cavity facing steel and gypsum. Figure 4.18 (track areas are removed to get a better view) shows the different convective heat transfer coefficients in external and internal surfaces.

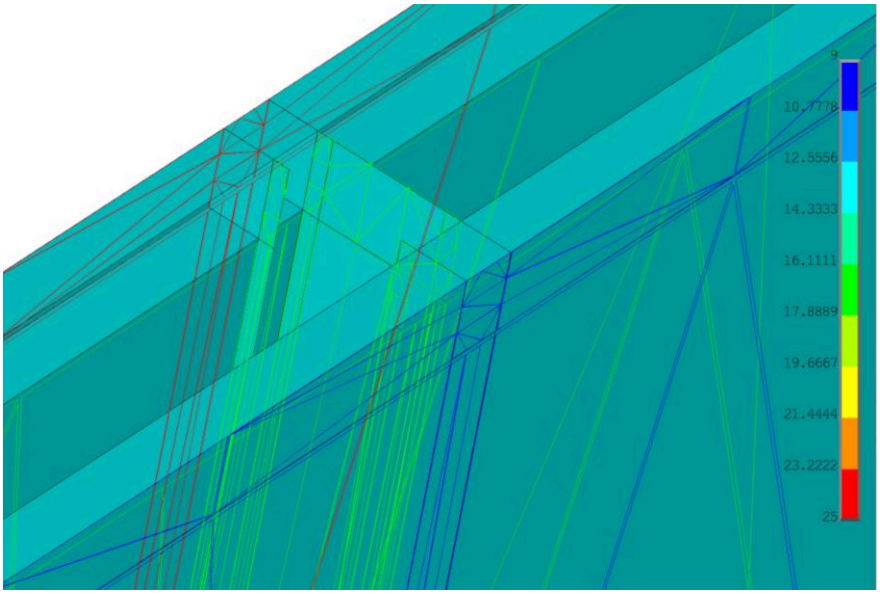

Figure 4.18 - Detail of different convective heat transfer coefficient (h) in C-lipped channels,

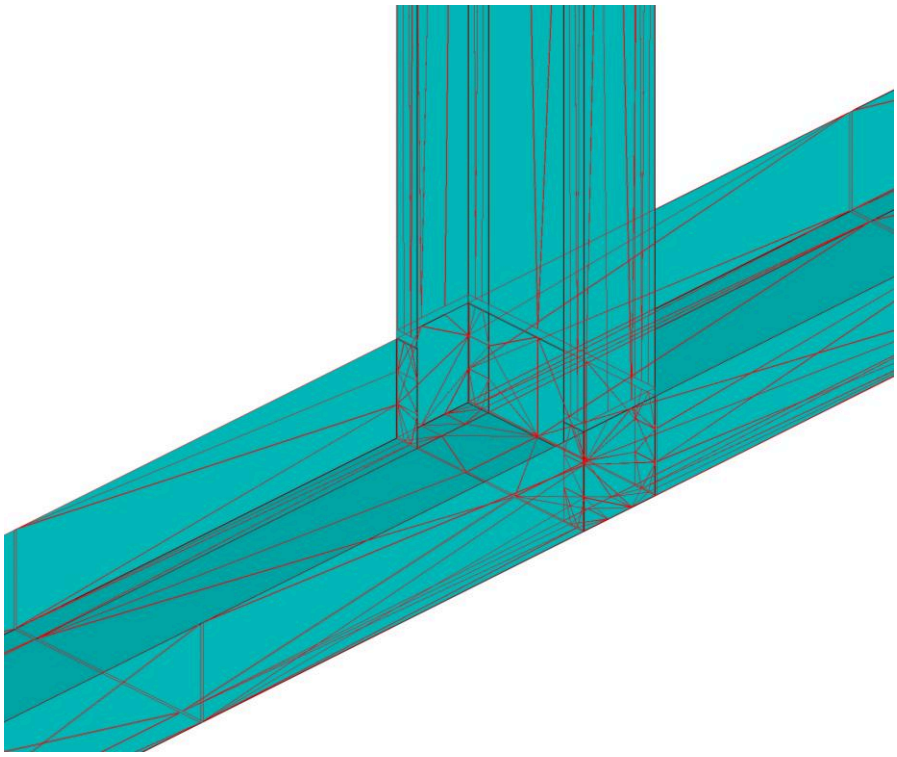

Figure 4.19 - Detail of convection applied in steel surfaces in C-lipped channels without cavity insulation.

Omitting the gypsum surfaces, Figure 4.19 and Figure 4.20 shows the details of track-stud surfaces and elements with convective coefficient and emissivity. Note that the values are applied only in the internal surfaces of the cavity, because the purple side have contact with other surfaces.

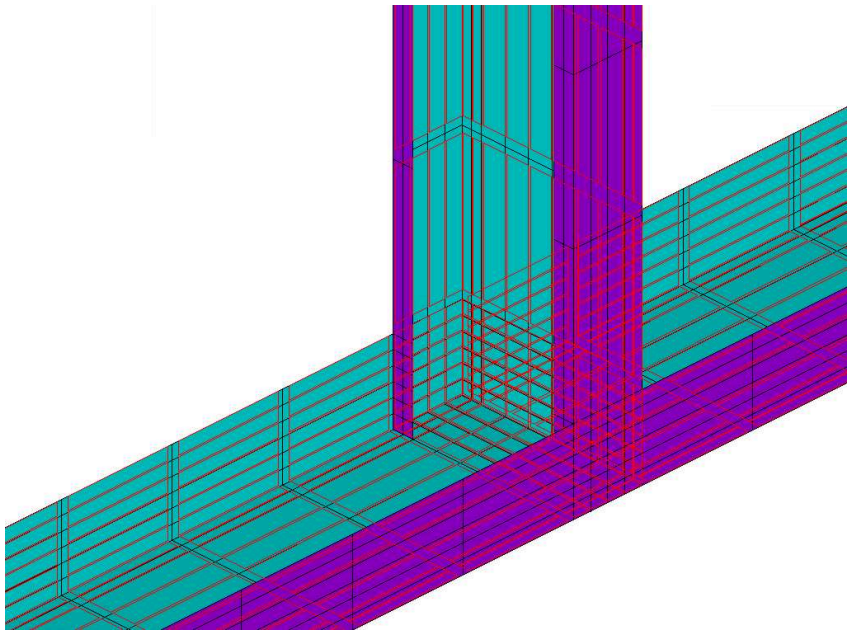

Figure 4.20 - Detail of radiation emissivity applied in lipped channel stud without cavity insulation.

Specimen 06 shares the same configuration as specimen 02, except for the addition of glass fiber insulation. This insulation effectively hinders the processes of convection and radiation, resulting in reduced heat transfer. Consequently, heat conduction becomes the primary mode of heat transfer, and using a material with low conductivity. The cavity material was modelled with the Solid 70 finite element. This element is depicted in Figure 4.21 where the gypsum is omitted to improve the visibility.

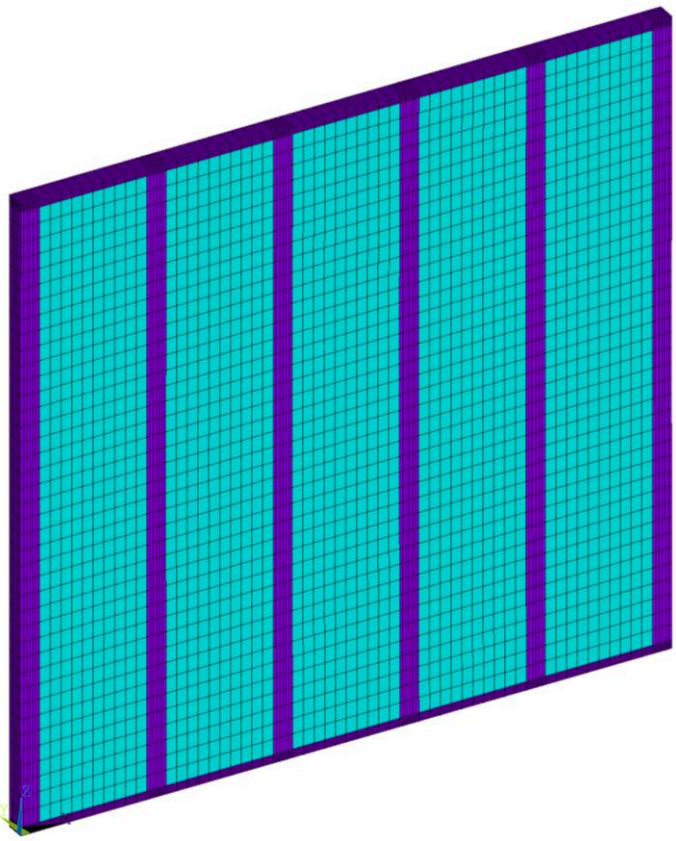

Figure 4.21 - Specimen 06 omitting gypsum.

In the numerical model, the cavity insulation is idealized with perfect geometry, filling all spaces available, without accounting for any empty spaces in the cavity (Figure 4.22). However, in reality, the assembly is not perfect, and this simplification leads us to expect worse outcomes for this particular specimen.

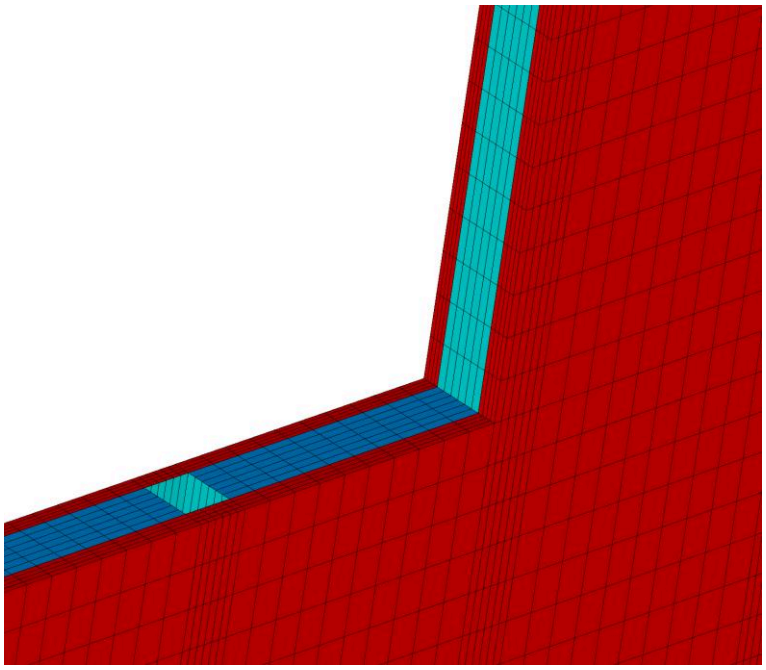

Figure 4.22 - Cut view of specimen 06 with the three materials, gypsum (red), glass fiber (dark blue) and steel (light blue).

The external boundary conditions remain the same as the previous specimens, but with cavity insulation material, for this specimen, one can be applied convection and radiation in the stud hollow cavity, unlike S01, S02 and S03. For the like of better estimates, convection was applied with 17 W/m²K as shown in Figure 4.23.

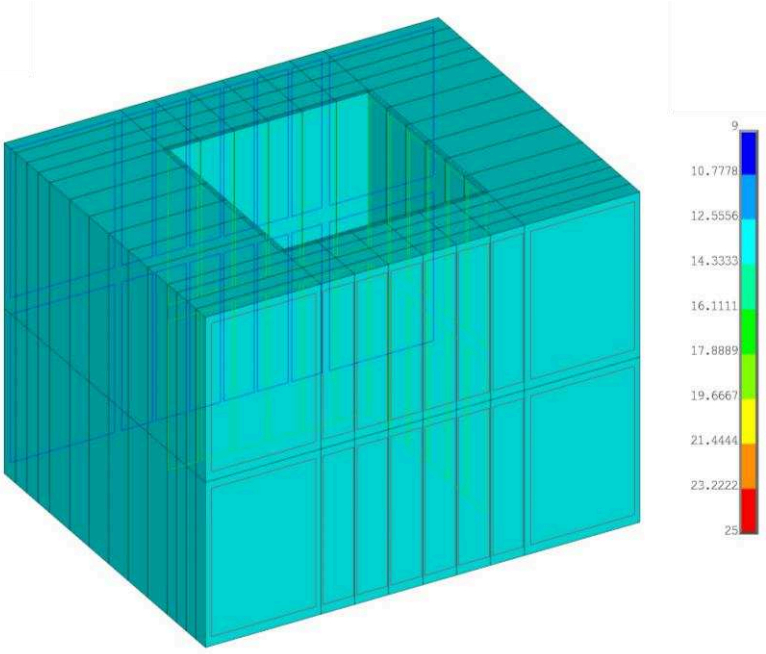

Figure 4.23 - Detail of convection applied to hollow section specimen with wall cavity insulation

As in this case (hollow steel section) there will be no cracks, a lower emissivity was chosen to be 0.5. In a preliminary analysis this configuration showed better temperature results than not applying these conditions, see details in Figure 4.24.

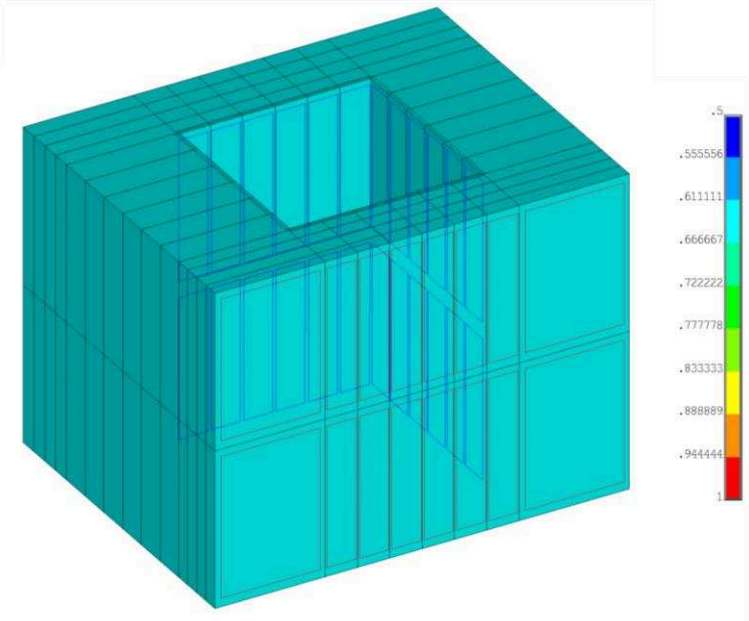

Figure 4.24 - Detail of radiation emissivity applied to hollow section specimen with wall cavity insulation.

Appendix A has relevant information about the number of elements of each type and material besides the computational size of the main simulations performed.

4.6. Thermal Validation

Following the standard to fire tests [40] is necessary to apply the temperature fire curve [24], but sometimes the experimental furnace tests present a difference between the furnace curve and ISO 834 curve. This difference can occur for several reasons, like combustion of materials, furnace problems, or leakages, but this difference is especially significant in specimen 01, where the curves differ by more than 100 °C after 240 min. This difference was explained by author with a problem in the low-pressure supply of gas furnace [22].

To apply the closest numerical scenario to the fire experiment, the fire curve temperature applied to numerical analysis was the furnace curve taken from the real fire tests, even when it differs so much.

The real experimental temperatures used for comparison are collected by different thermocouples distributed by the following locations and nomenclature (Figure 4.25) and sometimes in more than one similar position (average temperature is sometimes used). The numerical temperatures are determined by collecting the temperatures over time from nodes closest to the position of the real sensors.

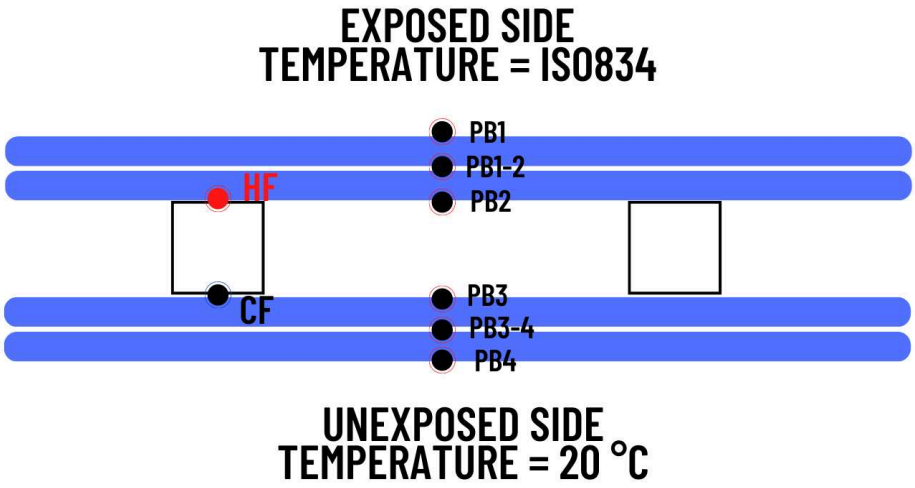

Figure 4.25 - Nomenclature of sensors in a fire test.

All the possible information is taken from the original tests through the sensors positioned in the configuration shown in Figure 4.25, most values are presented in graphs, to take these values the open-source software *Engauge Digitizer* was used. This software transforms an image and its pixels into numerical values, and the positioning of the axis is calibrated manually, this can lead to minor errors when done carefully (Figure 4.26). The reading of the curves is done automatically by the software by color contrast, and the point values are calculated to the axis values, the program makes the linear interpolation between points to extract the values when necessary.

The thermal solution was considered transient and nonlinear, using an incremental time step of 60 seconds, with the possibility to be reduced to 1 second with the time at end equal to the experimental fire test. The convergence criteria were based on the heat flow, with a tolerance value of 10^{-3} (0.001%) and a reference value of 10^{-6} [W].

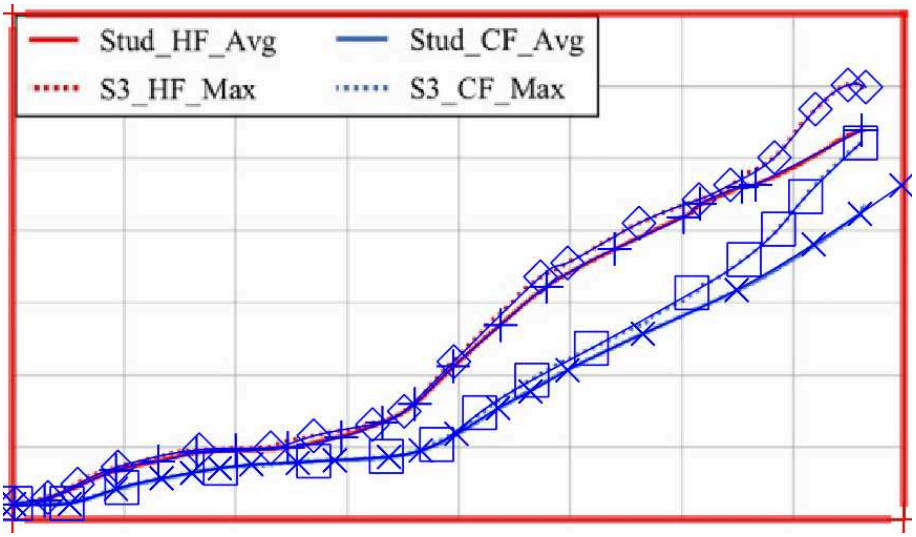

Figure 4.26 - Data collected with Engauge Digitizer.

Figure 4.27 to Figure 4.38 compare the temperature results over time of all specimens to steel parts (HF and CF), assuming the cavity temperature (CAVITY) and plasterboard temperatures.

All of the specimens exhibited similar behavior, thereby indicating the favorable repeatability of the selected thermal model. It was observed that, for all numerical specimens, the Hot Flange consistently aligned with the experimental results until approximately 65 minutes. However, beyond this point, it displayed values exceeding the experimental results, leading to an anomaly in the monitoring process. Notably, this development yielded improved outcomes for specimen 04 (Figure 4.34), which had a simulation duration of 75 minutes. The cold flange exhibits consonant behavior as well, delivering exceptional results for temperatures below 200 °C. However, rather than encountering a distinct point of departure from the experimental curve at a specific time, it experiences a rapid temperature increase upon reaching the 200 °C threshold. This occurrence could potentially be attributed to a reduction in the specific heat of the plasterboard material.

The temperature readings obtained from the sensors placed within the plasterboard layers also exhibited a satisfactory correlation until reaching approximately 200 °C, after which their temperatures increased. This observation provides support for the hypothesis that this phenomenon can be attributed to the completion of the first peak of specific heat in the plaster material.

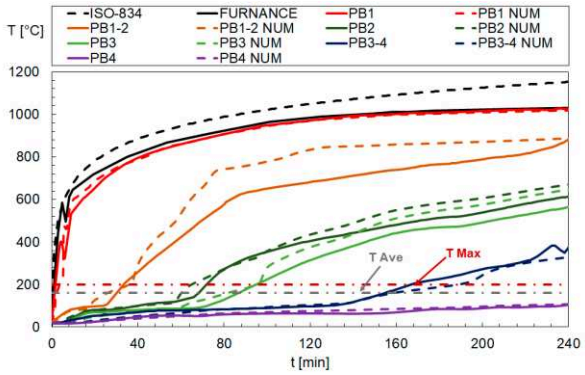

Figure 4.27 - Temperatures for components of specimen 01.

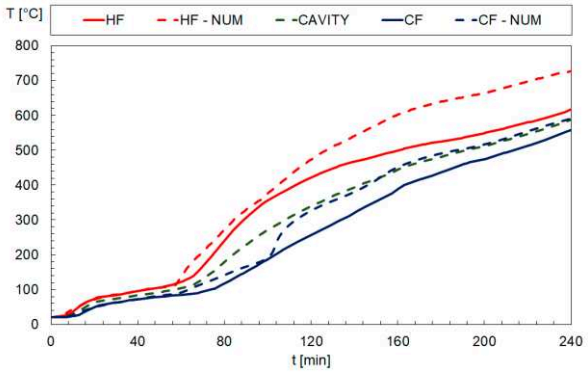

Figure 4.28 - Temperatures of the cavity, specimen 01.

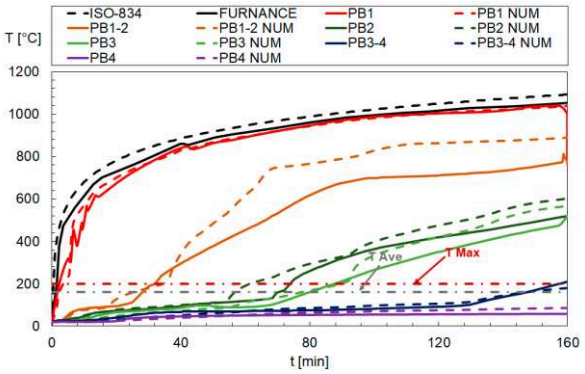

Figure 4.29 - Temperatures for components of specimen 02.

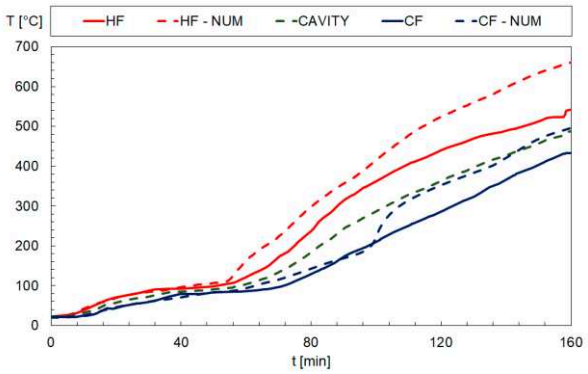

Figure 4.30 - Temperatures of the cavity, specimen 02.

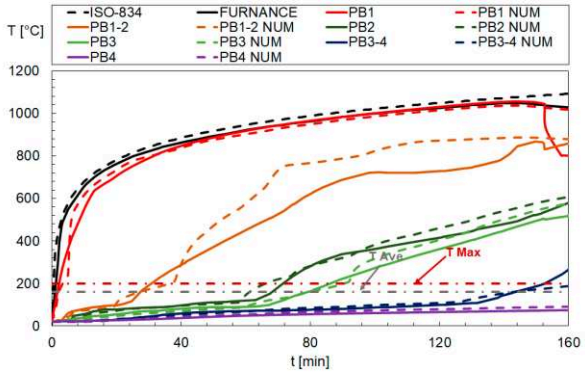

Figure 4.31 - Temperatures for components of specimen 03.

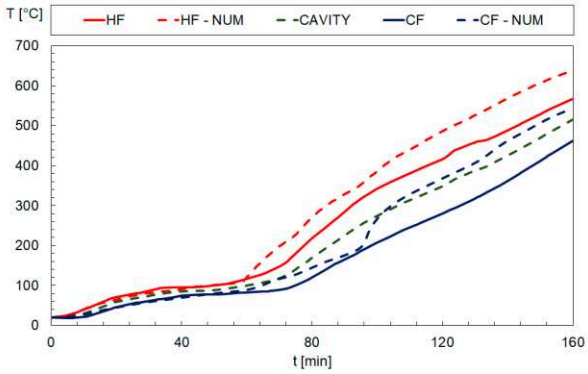

Figure 4.32 - Temperatures of the cavity, specimen 03.

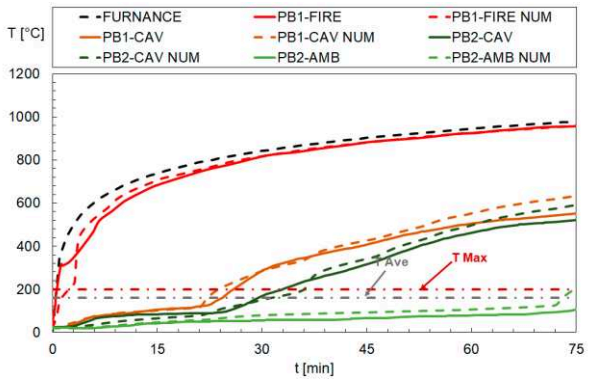

Figure 4.33 - Temperatures for components of specimen 04.

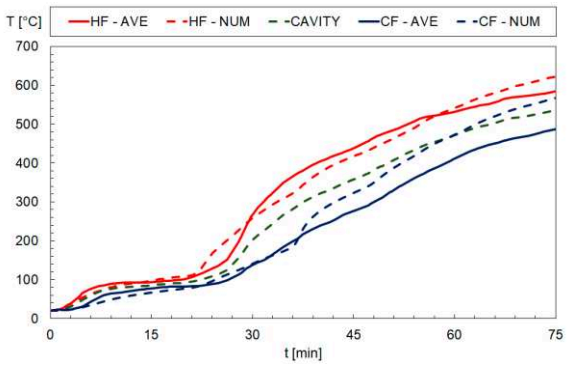

Figure 4.34 - Temperatures of the cavity, specimen 04.

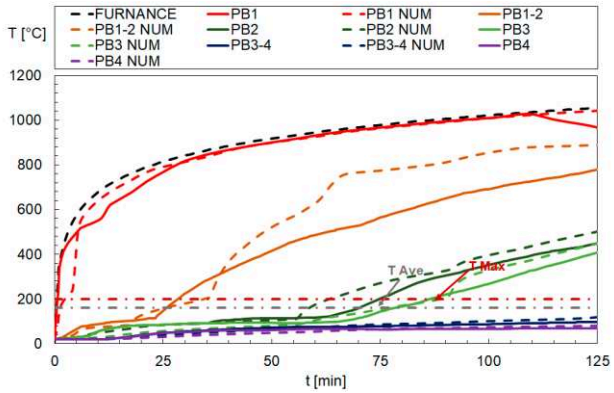

Figure 4.35 - Temperatures for components of specimen 05.

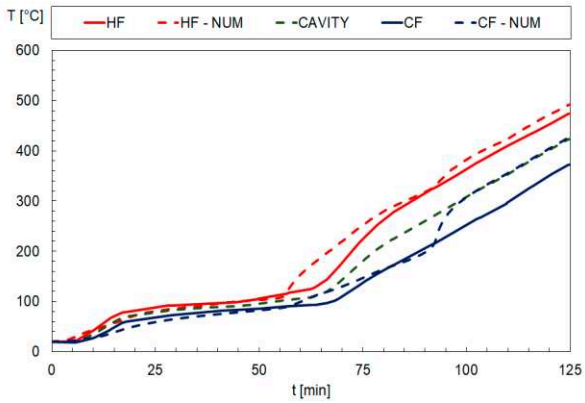

Figure 4.36 - Temperatures of the cavity, specimen 05.

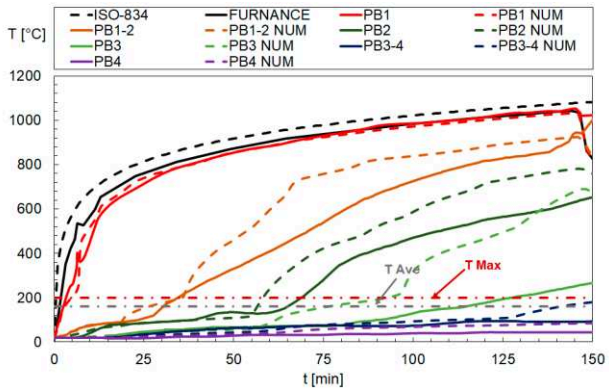

Figure 4.37 - Temperatures for components of specimen 06.

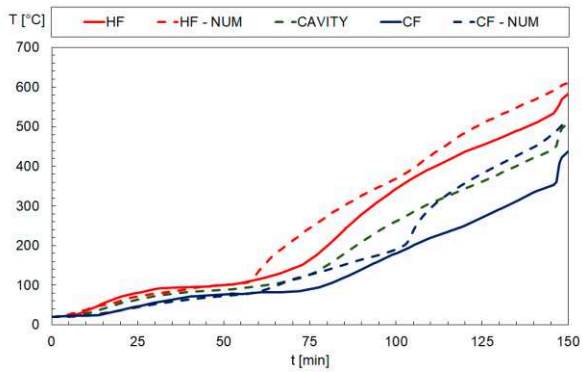

Figure 4.38 - Temperatures of the cavity, specimen 06.

It is worth noting that the numerical model employed in this study featured a meticulously positioned plasterboard material with thermal properties defined in accordance with established standards. However, it is important to acknowledge that real-world plaster may possess slightly different properties, and the assembly process itself can potentially introduce variations that impact the results obtained.

The experimental results have validated the numerical thermal model in terms of temperature evolution over time and insulation ability, most researchers don't use a quantitative method to validate the models, only approving or disapproving by qualitative parameters. In this paper, the root mean square error (RMSE) has been calculated with equation (26) for the temperature histories of the steel stud, by comparing the finite element analysis and experimental results every 10 minutes.

$$RMSE = \sqrt{\frac{1}{n}\sum_{i=1}^{n}(T_{FEA} - T_{test})^2} \tag{26}$$

The results are presented in Table 4.2, indicating an accurate approximation and all specimens. It is worth noting that the recorded temperature by any thermocouple in the furnace shall not deviate from the standard temperature versus time curve by more than 100°C after the first 10 minutes of any standard fire test [40]. Using the criterion from standard EN1363-1, one can consider a good approximation when the RMSE is smaller than 100ºC.

Table 4.2 - RMSE error for the temperature evolution in all components.

SPECIMEN ID	Number of instants [n]	RMSE HF [°C]	RMSE CF [°C]	RMSE PB1 [°C]	RMSE PB1-2 [°C]	RMSE PB2 [°C]	RMSE PB3 [°C]	RMSE PB3-4 [°C]	RMSE PB4 [°C]
01	24	75.76	39.99	12.67	102.06	45.04	56.77	25.15	8.75
02	15	47.61	27.93	27.53	124.46	52.14	47.18	13.00	16.08
03	15	36.47	42.70	21.26	109.27	32.97	30.64	9.70	10.52
04	7	20.54	43.59	8.54	-	33.18	32.18	-	23.88
05	12	11.08	19.40	31.77	134.73	39.12	31.03	9.75	10.21
06	15	40.01	57.52	17.37	114.17	111.43	210.62	30.59	24.37

The results of the temperature evolution in PB1-2 show the biggest error and stay above the 100°C of difference by the RMSE, this may have occurred because, in the numerical model, the contact between layers is modelled as perfect, providing a uniform and total heat transfer by conduction. In the fire test, the layers are attached by screws and the position of thermocouples between layer 1 and 2 can move away from the perfect contact. Furthermore, the temperature in this position isn't required to evaluate the fire resistance criteria. This phenomenon possibly can also occur in the interface PB3-4, but the temperature is less than 100 ºC and it is not as evidenced in the RMSE results. Figure 4.39 to Figure 4.42 shows a comparison of temperature distribution between 4 of the 6 specimens after 100 minutes of simulation. More images of thermal simulations can be found in Appendix B.

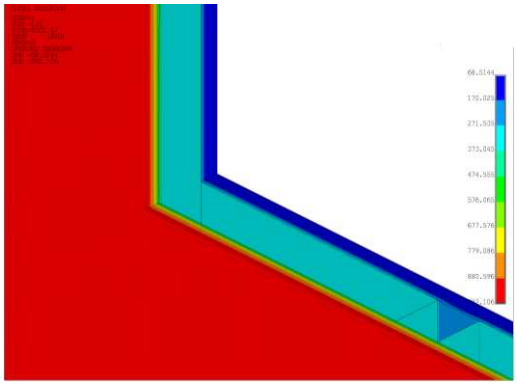

Figure 4.39 - temperature spread after 100 minutes to specimen S02.

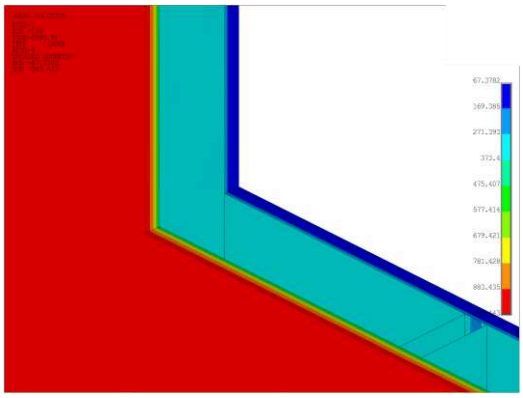

Figure 4.40 - temperature spread after 100 minutes to specimen S03.

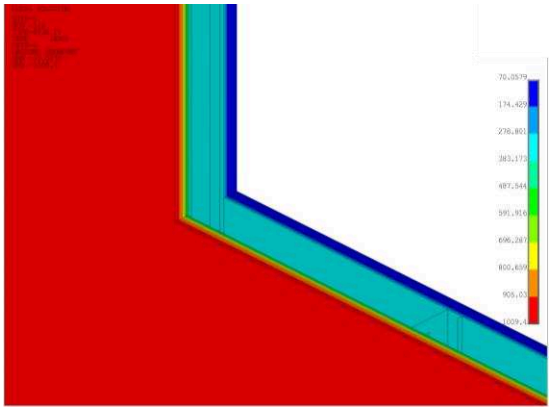

Figure 4.41 - temperature spread after 100 minutes to specimen S05.

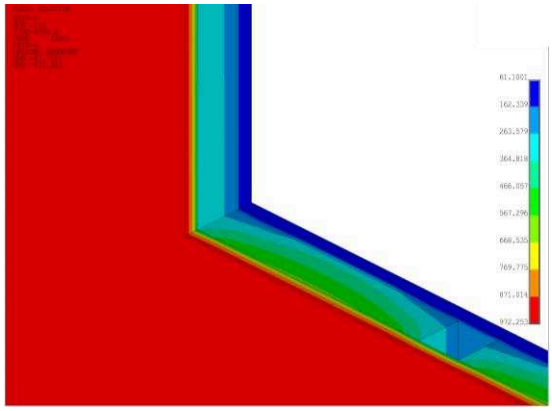

Figure 4.42 - temperature spread after 100 minutes to specimen S06.

4.7. Thermomechanical Validation

To conduct the thermo-mechanical analysis, the model is modified by removing the solid finite elements. In this analysis, it is assumed that the gypsum layers and cavity insulation do not contribute to the load-bearing capacity of the LSF wall. However, their thermal effects are considered during the thermal analysis phase. The boundary conditions for displacements remain consistent with those used in the load-bearing simulation, which results in a partially restrained effect within the plane of the wall.

With the same load level applied in the experimental test, the model undergoes a step-by-step

and interative process for thermo-mechanical analysis. The time step used is initially set to 60 seconds, but it can be decreased to 0.01 seconds if necessary. The Newton-Raphson method is employed, utilizing a convergence criterion based on internal efforts. The force and moment are measured using a reference value of 1 [N] and 1 [Nm] respectively. A tolerance level of 0.1% is considered.

Specimens S01, S02, and S06 consist of a hollow square section with an identical moment of inertia for both axes. Experimental tests conducted at room temperature [9] revealed that when subjected to a low buckling length, this profile can exhibit local failures. However, when subjected to a greater free buckling length, such as in 3-meter walls, its primary failure mode shifts to global (flexural) failure.

Furthermore, fire tests demonstrated that the presence of gypsum alone does not provide sufficient stiffness to prevent out-of-plane displacement, as all three specimens exhibited the same failure characteristics. This finding in numerical simulations was consistent with it, as depicted in Figure 4.43.

Figure 4.43 – Critical failure modes of stud 4 from fire test specimen [9] and stud 4 at failure time from FEM.

The rectangular section specimen no longer possesses symmetrical properties in both axes, resulting in reduced resistance to web buckling along the longer dimension. As a consequence, its compressive strength limit is determined by local failure. The numerical results closely align with the findings from experimental tests, as depicted in Figure 4.44.

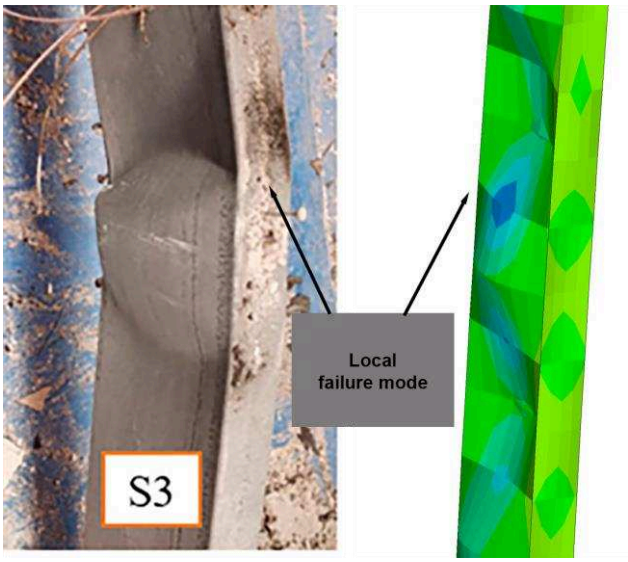

Figure 4.44 – Critical failure mode of stud 3 from fire test specimen [9] and stud 3 at failure time from FEA.

Specimens 04 and 05 have a C-shaped profile, characterized by upper and lower flanges and a longer web. This design provides greater bending stiffness to the flanges about the web. When subjected to compression or bending, the load is primarily transmitted to the flanges. Consequently, the flanges tend to experience localized deformation, especially in load points. Figure 4.45 show the similarity of the FEM model and the experimental fire test.

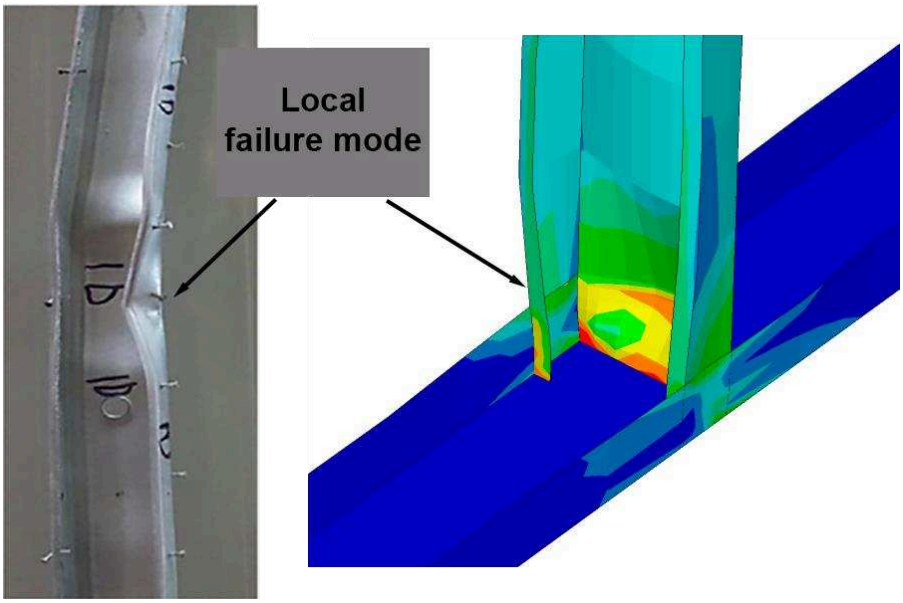

Figure 4.45 - Critical failure modes of stud 4 from fire test specimen [18] and stud 4 at failure time from FEA.

The failure mode of the lipped channel studs could be considered as the interaction of local buckling and out-of-plane flexural buckling (Figure 4.46) with a higher influence of local buckling, such predicted by [42]. The web buckling failure of rectangular stud shape can be observed in Figure 4.47.

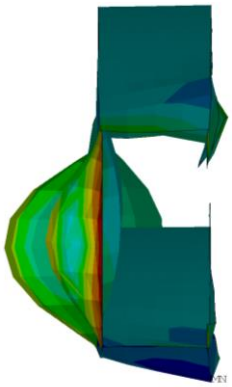

Figure 4.46 - Upper view of web and flexural buckling of a lipped channel.

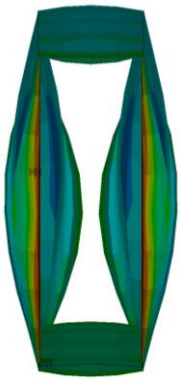

Figure 4.47 - Upper view of web buckling of a rectangular channel.

All the specimens show a good agreement failure mode, for that, the parametric study with different load levels can be conducted. With all validation approved, the fire resistance of the models is evaluated by subjecting it to various load levels ranging from 20% to 80% of the LSF structure's maximum load-bearing capacity at room temperature.

Specimens 01, 03, 04, and 05 exhibited non-convergence during the thermal simulation, which coincided with the duration of the experimental tests. Nevertheless, by analyzing the von Mises stress for each specimen, as depicted in Figure 4.48 and considering the parametric analysis provided in the subsequent section, the conclusion can be drawn that a load-bearing failure is expected to be achieved shortly after the respective time. This numerical outcome implies that the system is prone to undergo structural failure within a relatively brief period.

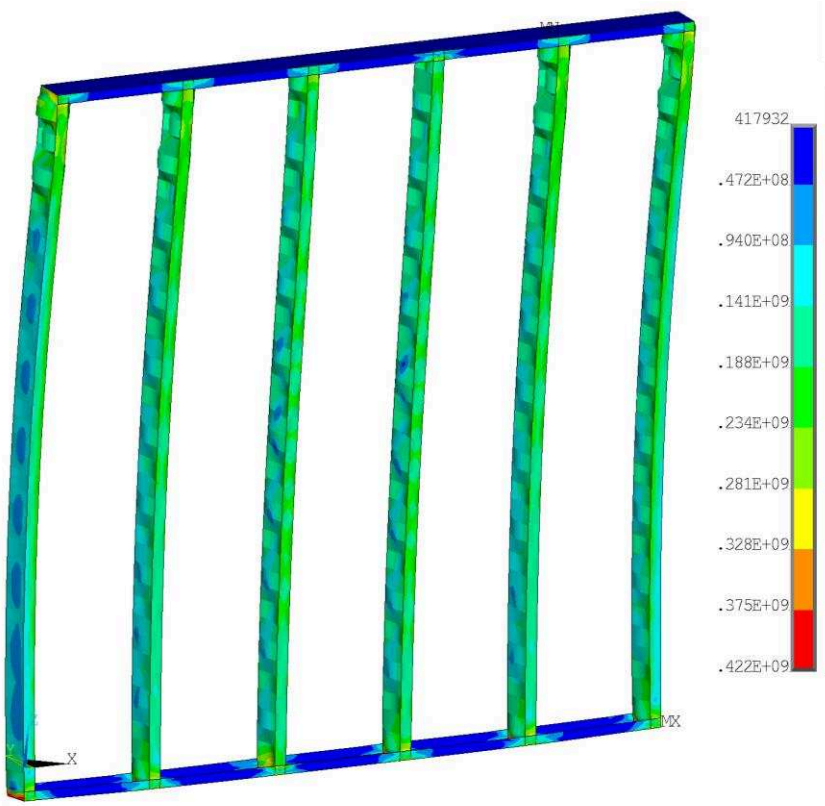

Figure 4.48 – von Mises stress at 147 minutes. Specimen 03.

5 Parametric Study and Results

The fire resistance of the models is evaluated by subjecting them to various load levels ranging from 20% to 80% of the LSF maximum load-bearing capacity at room temperature. To conduct the thermo-mechanical analysis, the model is modified by removing the solid finite elements (nonstructural materials). In this analysis, it is assumed that the gypsum layers and cavity insulation do not contribute to the load-bearing capacity of the LSF wall. However, their thermal effects are considered during the thermal analysis phase. The boundary conditions for displacements remain consistent with those used in the load-bearing simulation, which results in a partially restrained effect within the plane of the wall. Table 5.1 to Table 5.6 presents all the simulations developed in this parametric study the for each load level with final resistance time, hot flange and cold flange temperatures. The insulation criteria is only achivied before the resistance criteria to the specimen 04, who have only one 16 mm gypsum layer, the average temperature in the unexposed side is more than 160 °C after 73 minutes as presented in Table 5.4.

Table 5.1 - Parametric results to critical time and temperature (R) of the load-bearing LSF walls (specimen 01).

SPECIMEN ID	LOAD LEVEL μ [%]	TIME TO FAILURE (R) [min]	HF TEMP. [°C]	CF TEMP. [°C]
01	20	250+	731	602
	25	236	723	585
	30	217	692	549
	35	198	662	514
	40	177	635	486
	45	164	612	462
	50	155	589	435
	55	143	551	390
	60	133	520	362
	65	123	487	337
	70	115	453	309
	75	94	346	173

Table 5.2 - Parametric results to critical time and temperature (R) of the load-bearing LSF walls (specimen 02).

SPECIMEN ID	LOAD LEVEL μ [%]	TIME TO FAILURE [min]	HF TEMP. [°C]	CF TEMP. [°C]
02	40	141	601	426
	45	133	571	393
	50	123	535	362
	55	114	498	331
	60	98	402	197
	65	89	352	167
	70	81	306	147

Table 5.3 - Parametric results to critical time and temperature (R) of the load-bearing LSF walls (specimen 03).

SPECIMEN ID	LOAD LEVEL μ [%]	TIME TO FAILURE [min]	HF TEMP. [°C]	CF TEMP. [°C]
03	40	160+	638	544
	45	156	627	530
	50	150	606	506
	55	145	589	485
	60	140	570	463
	65	134	544	430
	70	131	531	413
	75	126	511	392
	80	119	483	365

Table 5.4 - Parametric results to critical time and temperature (R) of the load-bearing LSF walls (specimen 04).

SPECIMEN ID	LOAD LEVEL μ [%]	TIME TO FAILURE [min]	HF TEMP. [°C]	CF TEMP. [°C]	TIME TO INSULATION FAILURE (I) [min]
04	20	78+	635	583	73
	25	78+	635	583	73
	30	75	623	568	73
	35	69	598	540	/
	40	66	582	521	/
	45	62	558	493	/
	50	58	526	455	/
	55	56	512	440	/
	60	33	295	163	/
	65	31	273	150	/
	70	29	245	134	/
	75	28	230	126	/
	80	26	200	113	/

Table 5.5 - Parametric results to critical time and temperature (R) of the load-bearing LSF walls (specimen 05).

SPECIMEN ID	LOAD LEVEL μ [%]	TIME TO FAILURE [min]	HF TEMP. [°C]	CF TEMP. [°C]
05	50	125+	493	428
	55	124	489	424
	60	122	480	414
	65	116	451	383
	70	80	278	164
	75	76	251	147
	80	73	239	140

Table 5.6 - Parametric results to critical time and temperature (R) of the load-bearing LSF walls (specimen 06).

SPECIMEN ID	LOAD LEVEL μ [%]	TIME TO FAILURE [min]	HF TEMP. [°C]	CF TEMP. [°C]
06	40	147	598	494
	45	141	571	453
	50	132	537	413
	55	125	508	382
	60	116	463	336
	65	94	343	174

5.1. Effect of the load level

12 simulations were conducted on Specimen 01, starting from a load level of 20% and increasing by 5% in each simulation, up to 75%. The software failed to converge at the desired load level of 80%. Experimental fire resistance tests were carried out, at a load level of 20%, presenting a fire resistance of 246 minutes. The simulation developed with the same load level required more than 250 minutes. When the load level was raised to 25%, the fire resistance dropped to 236 minutes, accompanied by a hot flange temperature peak of 723 °C. As the load level further increased to 75%, the fire resistance decreased to 94 minutes, with a significant drop occurring between 70% and 75%. At the critical temperature of 346 °C, observed at the 75% load level, which represents a decrease of 377 °C from the critical temperature determined to the load level of 20%. The specimens displayed consistent displacement over time, indicating good agreement with the expected behavior, see Figure 5.1.

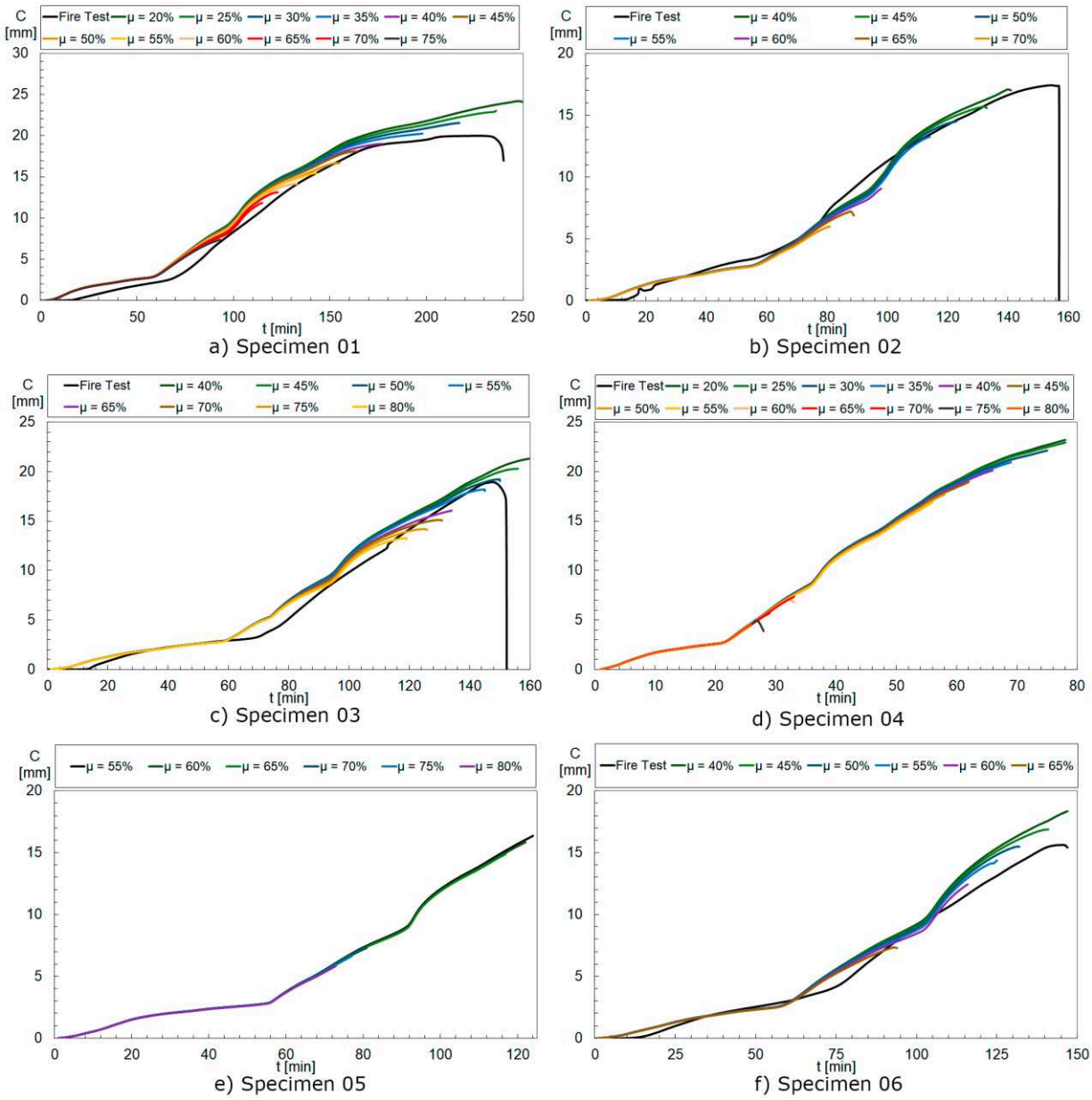

Figure 5.1 - Vertical displacement of critical stud.

The simulations of the specimen 02 started at a load level of 40% and gradually increased by 5% until reaching 70%. However, the software failed to converge beyond this point. The Fire resistance at 40% load level was predicted by simulation to be 141 minutes, which is 17 minutes smaller than the fire test. The fire resistance decreased steadily until reaching 55% load level, at

which point there was a significant drop to 60%. Continuing to increase the load level to 70%, resulted in a final resistance time of 81 minutes. The critical temperature change during the simulations was notable, with the highest temperature recorded at the HF by 601°C for 40% load level, reducing to a critical temperature of 306°C for the case of 70%.

The simulations of specimen 03 started at a load level of 40% and changed to 80%. The fire resistance time when using the load level of 40% did not converge before the 160 minutes of simulation. At a load level of 45%, the fire resistance was determined by 156 minutes, accompanied by a high critical temperature of 627°C. This specimen exhibited a slight and almost constant decrease in fire resistance as the load level increased, resulting in a higher critical temperature when compared to the other specimens. At 80% load level, the fire resistance reached 119 minutes with a critical temperature of 483°C, which represents a difference of only 144°C. This difference is smaller when compared to the other specimens.

Specimen 04 underwent simulations at various load levels ranging from 20% to 80%. However, it was only at the 30% load level that the simulation successfully converged before reaching the final 80 min. This indicates an overestimation of the fire resistance for this particular specimen, a trend observed in Specimen 05 as well, which shares the same grade and stud shape. From 30% to 80% load level, there was a significant reduction in fire resistance, dropping from 75 min to 26 min. Similarly, the critical temperature was reduced from 623°C to 200°C. This specimen exhibited a similar drop in fire resistance, as Specimen 02 did, but in this case, the drop was more pronounced, resulting in a 41% reduction in fire resistance compared to a 14% reduction in the previous specimen. Another notable observation is that the fire resistance at the 65% load level was the same as that at the 60% load level, both reaching 33 minutes.

Specimen 05 stands out as the most overestimated specimen. The simulation for this specimen started at a load level of 40%, equal to the fire test, which lasted 124 minutes. The fire resistance for 55% load level, was determined to be 124 min, corresponding to a critical temperature

of 489°C. The fire resistance for this specimen was predicted to be 73 min, achieved at an 80% load level, with a corresponding critical temperature of 239°C. It is worth noting that another significant drop in fire resistance occurred between the 65% and 70% load levels. This may be justified by the reduction coefficients expected at the corresponding critical temperatures.

In the case of specimen 06, the simulations began at a load level of 40% and progressively increased to 65%. The fire resistance decreased from 147 min at 40% load level, to 94 min at 65% load level. Notably, there was a significant drop in fire resistance between the 60% and 65% load levels. The corresponding hot flange temperature changed from 598°C to 343°C, indicating a substantial critical temperature decrease.

Figure 5.2 presents the results obtained from 54 thermomechanical simulations, a series of experiments, depicting the relationship between the load level and the critical temperature, which is defined as the hot flange temperature. This visual representation allows for a clear understanding of how the critical temperature varies with different load levels.

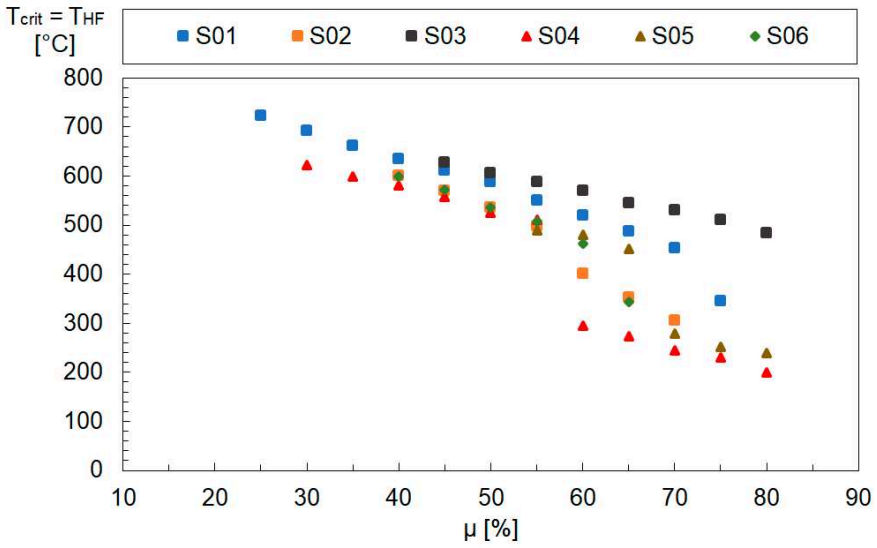

Figure 5.2 - Critical Temperature of the steel stud for all specimens

6 Discussion of results

Numerical analysis results indicate that the failure mode in the symmetric hollow sections model typically involves a global instability mode, with some presence of local modes of instability. On the other hand, the primary failure mode observed in the C-Shapes and rectangular hollow section (which has a much higher moment of inertia in one direction than in another) is local buckling, specifically web buckling and distortional buckling. To accurately validate this new proposal, additional load-bearing tests should be conducted using different shapes of studs.

One notable finding in this study, which deviates from existing literature, is the occurrence of abrupt drops in fire resistance for specimens S01, S02, S04, S05, and S06. These drops occurred within a similar critical temperature range of approximately 500°C, but at different load levels and for different specimens. These drops are likely related to the chosen reduction factors and their behaviour within this temperature range. This hypothesis is supported by the fact that specimen S03, which did not exhibit any drops in fire resistance, consistently maintained its critical temperature above this range for all load levels.

Although the precise impact of these drops on the accuracy of the results could not be evaluated, it is recommended for future research to explore the use of different reduction factors to determine if similar drops occur. This investigation would provide valuable insights into the influence of reduction factors on fire resistance behaviour and help improve the precision of future experimental studies in this field. The reduction factors may have contributed to the high critical temperature values, by having its yield stress value increased in a certain temperature range.

Effect of cavity insulation

Specimens S02 and S06 share the same square hollow tube configuration, differing only in the presence of cavity insulation in Specimen S06, made of fiberglass. Surprisingly, Specimen S06

consistently achieved a higher FRL in all load levels analyzed, with a minimum increase of 5 minutes compared to S02. These findings diverge from existing literature on cavity insulation, which typically indicates a reduction in FRL for profiles due to the high thermal gradient. However, the results obtained for this particular type of tube align with the experimental data.

This discrepancy can be attributed to the increased heat transfer between the exposed and unexposed sides of the specimen since the critical temperature of the flanges was very similar in both experiments, slightly lower for S06. The rectangular section of the tube behaves as if it has two webs that serve as heat bridges, in contrast to C, U or open profiles that have only one. Additionally, the absence of filling material within the tube's cavity allows for some level of convection and radiation, facilitating heat exchange between the ends.

Overall, these findings suggest that the presence of insulation inside the cavity of square hollow tubes, as seen in Specimen S06, may enhance fire resistance, contrary to general expectations.

Effect of double protective layer

The specimens S04 and S05 had the same C-profile stud configuration, with the difference being that S05 had double the protection with 16mm gypsum boards. In the experiment, S05 withstood 124 minutes at a load level of 55%, while S04 only lasted 56 minutes with a higher HF value, approximately 4 minutes per additional millimeter of protection on the exposed side. Although the value of S05 may be considered overestimated since this FRL should correspond to a lower load level according to fire tests, it aligns with the increased FRL due to the additional layers of protection on the exposed side.

Effect of the hollow cavity in stud

In a study conducted by Tao et al. [9], it was proposed that the use of cavity insulation in

hollow section studs with closed cavities facilitates heat transfer through multiple mechanisms such as thermal convection, radiation, and thermal conduction. This is in contrast to single channel studs where heat transfer is primarily reliant on thermal conduction alone. The multiple heat transfer mechanisms in closed cavity hollow section studs minimize the temperature difference between the hot and cold flanges, thereby reducing the occurrence of thermal bowing effects. Consequently, while cavity insulation has a significant impact on reducing the fire resistance level (FRL) of single-channel stud walls, its effect on the FRL of hollow section stud walls is comparatively minor.

Example a) of Figure 6.1 shows the scheme used for specimens 01, 02 and 03 without the use of heat transfer inside the cavity because of the limitation of the shell finite element as discussed earlier. In reality, a level of radiation and convection is expected, this limitation leads to less heat transfer in the whole and possibly a higher temperature gradient between flanges.

Example b) shows specimen 06 with the most suitable heat transfer conditions, because by the existence of insulation in the cavity, convection and radiation amounts were applied.

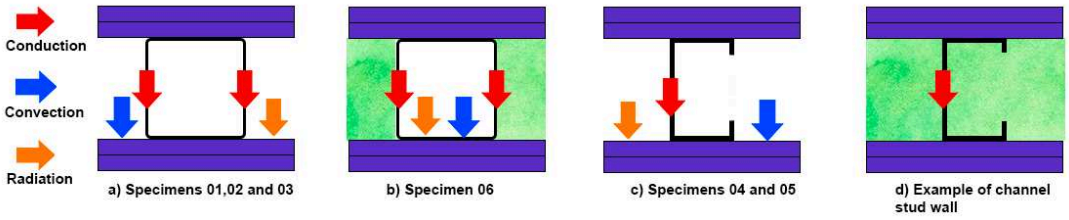

Figure 6.1 - Heat transfer mechanism in the hollow section and channel with and without insulation.

Example c) refers to specimens 04 and 05 with the three modes of transfers on all surfaces because of the open profile while example d), refers to what is expected in this type of profile when there is the presence of insulation in the cavity, can be observed in example b) of Figure 6.2 in a simulation performed on a wall with the same configuration as specimen 04 with the same glass fiber used in specimen 02.

Figure 6.2 exemplifies using a sectional image of the simulations performed of the different heat distributions in these types of profiles. In addition to the different heat flow, a greater temperature gradient between the flanges can be seen.

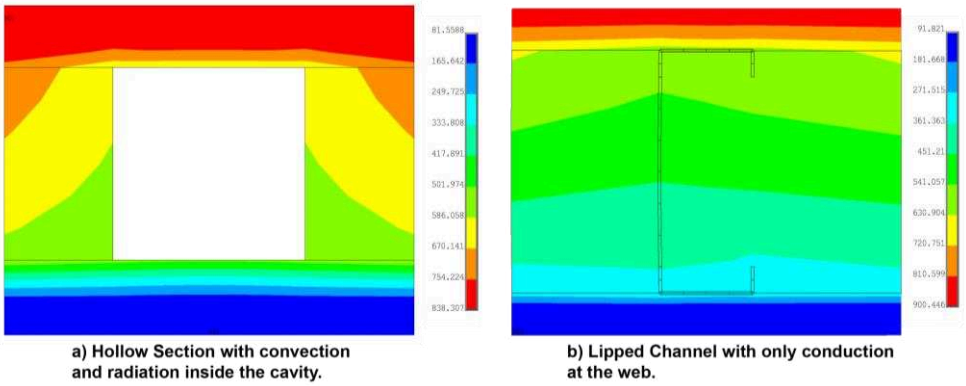

Figure 6.2 – Cut of temperature distribution in thermal analysis of specimen 02 after 150 min and a lipped channel after 50 min.

Effect of Stud Shape

Specimen S03 has the same steel as S02 and S06, but it is made with a rectangular profile instead of a square one. Despite its slightly lower strength compared to its counterparts, it exhibited superior results in several aspects. Its Fire Resistance Level was higher, and the decrease in FRL with increasing load was smaller than in other experiments, as reflected in Figure 5.2, where the average critical temperature was significantly higher. This may be attributed to the longer web length of the specimen, allowing for better heat transfer between surfaces. This is evident when comparing the differences between Hot Flange and Cold Flange temperatures, which were substantially lower in specimen S03 compared to S02 (and S06), in Figure 6.3 thus reducing the bowing effect.

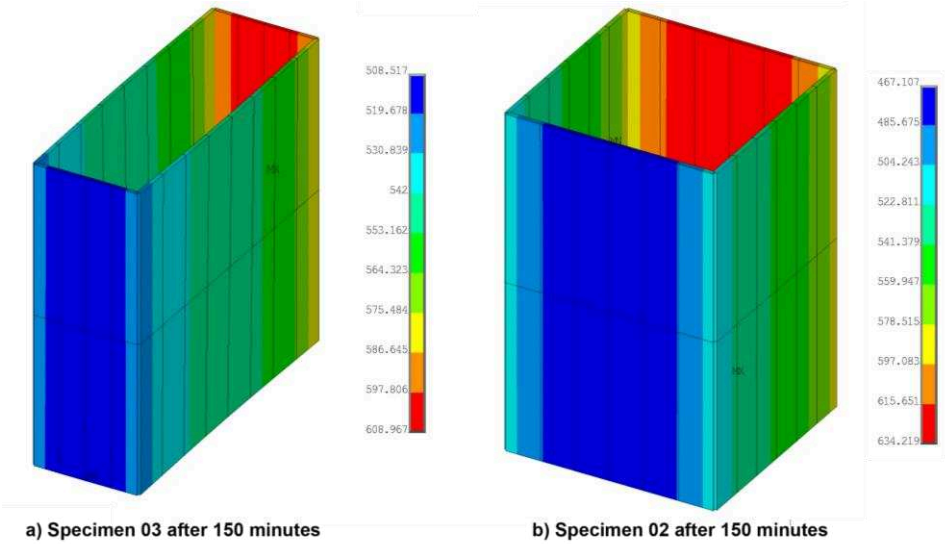

Figure 6.3 - Temperature gradient through finite elements to specimen RHS and SHS after 150 minutes, sectional image.

This profile seems to be a promising candidate for further studies on its application for fire safety. However, there is a lack of experimental studies on this design, necessitating future research to investigate the effects of different variables, such as different steel grades, protective layers, and cavity insulation to new numerical validation.

Effect of steel grade

The specimens S01 and S02 have very similar pillar shapes; therefore, for this study, they will be considered as equivalent, with the only difference being the steel grade of the pillars: C350 and C450, respectively. The experimental results for maximum load at room temperature were relatively close, considering the difference in yield strength of 62 MPa. However, there was a larger difference in this study due to the numerical results.

For the same load level values, specimen S01 exhibited a significantly higher Fire Resistance Level compared to its counterpart. For instance, at a 40% load level, S01 lasted 174 minutes, whereas S02 lasted 141 minutes. As the validation values were satisfactory, this difference may be due to the significant variation in temperature curves in the furnace during the S01 experiment. Another study

that eliminates this temperature deficiency or a numerical analysis considering the ISO834 curve is needed to more accurately evaluate the influence of the steel grade. Some authors suggest that reduction factors may differ for high and low-strength steels.

The new proposal to predict the critical temperature of LSF structure

Numerous previous studies have investigated the relationship between HF temperature and the load level. The figure labeled as Figure 6.4, showcases the maximum critical temperature achieved by all specimens.

Perera et al. [21] compiled dozens of load-bearing fire test results from various research and established a correlation between the critical temperature (HF) and the load level. Figure 6.4 presents the results obtained by Chen et al. in 2013 [11], who utilized single-channel section studs C89 and C140 for load levels of 32% and 65%, respectively. Additionally, Figure 6.4 incorporates the findings of Gunalam & Mahendran in 2014 [43], who conducted tests using four stud specimens with dimensions of C90x40x15x1.15mm. The load levels ranged from 6% to 100%, resulting in critical HF temperatures of 784°C and 20°C. Gunalam's research in 2011 [44], involving C90x40x15x1.15 and C92x50x15x1.15 stud specimens, also revealed that structurally similar LSF structures tend to fail at nearly identical critical temperatures, regardless of the number of protective layers or types of insulation materials used. These results are also included in Figure 6.4. Moreover, the study conducted by Ariyanayagam et al. in 2018 [18], focusing on six stud LSF structures constructed with C92x35x1.15 profiles, emphasizes the significance of the steel grade in determining the critical temperature for specimens under the same load level.

Figure 6.4 not only includes the compilation of previous studies but also incorporates more recent research findings. For instance, Piloto [19] uses the same hollow section LSF structure from specimen S01 employing the hybrid model. The results of Piloto' study, ranging from 25% to 80% load levels, are included in Figure 6.4. Furthermore, Dias et al. [12] examined three full-scale

specimens comprising web-stiffened studs at a 40% load level. Two of the specimens incorporated steel sheets inside and outside of plasterboard protection, demonstrating higher load capacity while maintaining the same fire resistance level. The fire test values collected from [9], which served as the source for specimens S01, S02, S03, and S04, are also incorporated in Figure 6.4. The numerical study of author also was incorporated [20]. By encompassing these additional studies, Figure 6.4 provides an overview of the latest findings in the field.

Figure 6.4 serves as a comprehensive visual representation, encompassing the aforementioned research outcomes and highlighting the influence of factors such as load level, steel grade, and structural configuration on the critical temperature of LSF specimens.

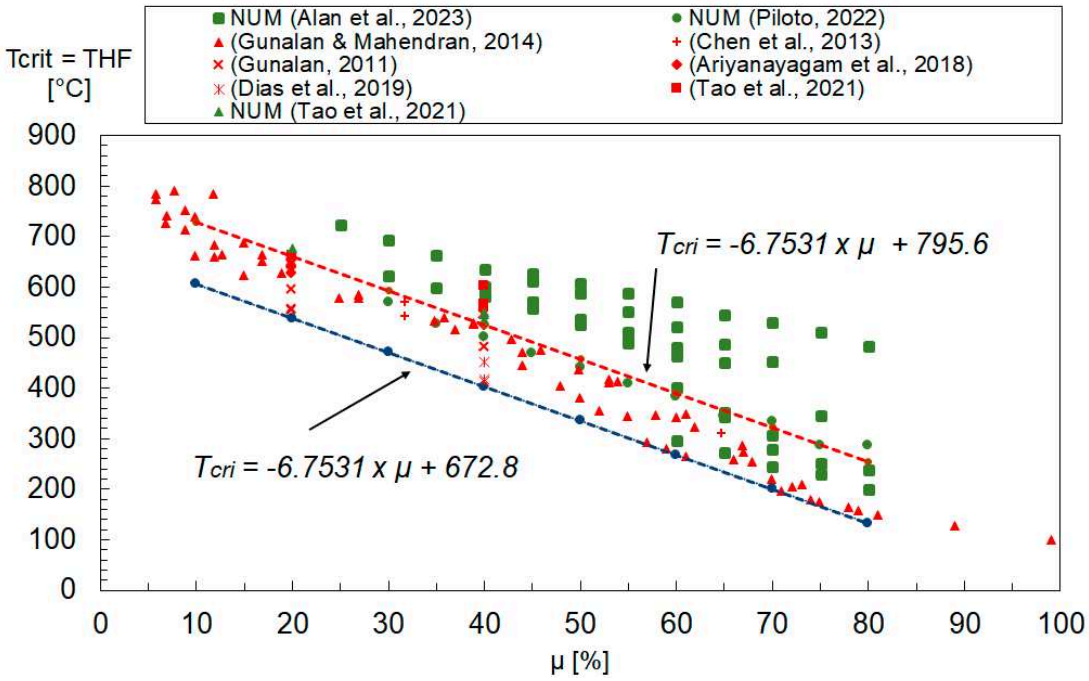

Figure 6.4 - Critical temperature to all LSF structures.

A new empirical formula has been proposed to determine the critical temperature based on the load level, specifically using the hot flange (HF) temperature as a representative value. This formula incorporates the results obtained in this study and data from 94 other authors' research.

The numerical simulations conducted on the LSF structures consistently exhibited a similar pattern in terms of the critical temperature (HF temperature) concerning the load level, as shown in Figure 6.4. The fire resistance of the structures depends on both the load level (μ) and the critical temperature (T_{cri}), which can be estimated using equation (27) to fit a normal trend line for all specimens. Alternatively, considering the average value of the HF temperature for each load level minus two times the standard deviation of the numerical results, equation (28) provides a reasonable approximation with a high level of safety. These formulas effectively estimate the critical temperature for all the specimens.

The critical temperature analysis reveals that the current limit stated in EN1993-1-2, which sets the fire resistance verification threshold at a cross-section temperature not exceeding 350°C, proves to be overly conservative for most simulated cases and unsafe for load levels higher than 55% in the case of class 4 cross-sections.

$$Tcri = -6.7531\, x\, \mu + 795.6, Tcrit\ [°C]; O.1 \leq \mu \leq 0.9 \quad (27)$$

$$Tcri = -6.7531\, x\, \mu + 672.8, Tcrit\ [°C], O.1 \leq \mu \leq 0.9 \quad (28)$$

The critical temperature results obtained in this study consistently exceeded those reported by other authors, particularly for the hollow profile specimens as previously mentioned. Notably, the papers [19], [20] stand as the single references for numerical tests conducted on hollow square section profiles, which also demonstrated higher critical temperature values compared to the others. This observation suggests a potential trend indicating that this profile type may follow a distinct equation for calculating critical temperature, distinct from open profiles like C or U sections. However, additional experimental and numerical studies are necessary to validate this hypothesis.

7 Conclusion

This dissertation presents a numerical investigation of six full-scale LSF tests with widely range of load levels, stud shapes, material grades, and composite protection layers.

The models underwent successful validation at room temperature, demonstrating favourable results in terms of maximum load and displacement. They also exhibited good performance in predicting temperature distribution, with slightly lower accuracy for components that were modelled as perfectly connected but are challenging to replicate in reality, such as gypsum layers and glass fiber.

In terms of thermomechanical analysis, the model proved capable of accurately predicting displacements. It effectively captured the deformed shape mode at the time of failure, including out-of-plane displacement caused by bending moments resulting from thermal bowing and load eccentricity. Notably, the model accounted for the displacement of the neutral axis towards the colder side during fire simulations.

Considering the hot flange temperature as the critical temperature for LSF walls, a new equation was proposed to determine the fire resistance based on the results obtained in this paper and a new compiled of almost a hundred other results from known literature. This proposed relationship enables the prediction of the fire resistance time at a certain load level through a preliminary thermal analysis of LSF wall types.

Numerical analysis results indicate that the failure mode in the square hollow sections model typically involves a global instability mode, with some presence of local modes of instability. On the other hand, the primary failure mode observed in the lipped channels and hollow sections with higher moments of inertia is local buckling, specifically web buckling and distortional buckling.

The results for structures with hollow section showed a higher critical temperature than those with open section, which may be a better solution for fire protection, especially the analysis of the

rectangular section that besides showing a higher critical temperature, also showed a lower decrease in FRL with the load increase. The lack of fire tests of this type of section makes it impossible to make a concrete statement that this profile is the most suitable for the increase of resistance.

Besides the better results regarding the critical temperature, the presence of insulation in the cavity with fiberglass in the square hollow section increased the resistance against fire about 5 minutes, this phenomenon is not observed in open sections, which have their resistance decreased by the bowing effect.

The software used for these simulations proved to be difficult to use, and errors between versions were recurrent, thus delaying the development of the research. Besides presenting convergence limitations for the thermomechanical studies for higher load levels and the impossibility of applying heat transfer phenomena on both sides of the shell finite element. The use of newer software with improved methods may be preferable for future research.

Overall, this investigation provides valuable insights into the fire behaviour of LSF walls with composite protection, highlighting the influence of load levels and insulation on their fire performance. The findings contribute to enhancing the design and construction practices for LSF structures, promoting improved fire safety standards in the industry.

References

[1] S. P. Ngian, L. T. Thong, M. M. Tahir, and A. Saggaff, 'Structural perfomance of cold-formed wall frame under combined gravity and lateral loading', in *IOP Conference Series: Materials Science and Engineering*, Institute of Physics Publishing, Nov. 2019. doi: 10.1088/1757-899X/620/1/012062.

[2] R. M. Lawson, 'Modular construction using light steel framing : an architect's guide', Steel Construction Institute, 1999.

[3] E. Yandzio, R. Lawson, and A. Way, 'Light Steel Framing in Residential Construction', London, 2015.

[4] Steel Framing Industry Association, 'The History of Cold-Formed Steel'. https://sfia.memberclicks.net/history (accessed Jun. 16, 2023).

[5] M. R. Vargas and V. P. Silva, *Fire resistence of steel structures (Portuguese Reference)*. Rio de Janeiro: CENTRO BRASILEIRO DA CONSTRUÇÃO EM AÇO, 2005. [Online]. Available: www.cbca-acobrasil.org.br

[6] A. S. Usmani, J. M. Rotter, S. Lamont, A. M. Sanad, and M. Gillie, 'Fundamental principles of structural behaviour under thermal effects', 2001.

[7] CEN, *13501-2: Fire classification of construction products and building elements*. Brussels: Comité Européen de Normalisation, 2010.

[8] S. T. Vy, M. Mahendran, E. Steau, and A. Ariyanayagam, 'Full-scale tests of load-bearing LSF walls made of built-up CFS channel sections under fire conditions', *Thin-Walled Structures*, vol. 187, Jun. 2023, doi: 10.1016/j.tws.2023.110763.

[9] Y. Tao, M. Mahendran, and A. Ariyanayagam, 'Fire tests of cold-formed steel walls made of hollow section studs', *J Constr Steel Res*, vol. 178, Mar. 2021, doi: 10.1016/j.jcsr.2020.106495.

[10] W. Chen, J. Ye, Y. Bai, and X. L. Zhao, 'Full-scale fire experiments on load-bearing cold-formed steel walls lined with different panels', *J Constr Steel Res*, vol. 79, pp. 242–254, Dec. 2012, doi: 10.1016/j.jcsr.2012.07.031.

[11] W. Chen, J. Ye, Y. Bai, and X. L. Zhao, 'Improved fire resistant performance of load bearing cold-formed steel interior and exterior wall systems', *Thin-Walled Structures*, vol. 73, pp. 145–157, 2013, doi: 10.1016/j.tws.2013.07.017.

[12] Y. Dias, M. Mahendran, and K. Poologanathan, 'Full-scale fire resistance tests of steel and plasterboard sheathed web-stiffened stud walls', *Thin-Walled Structures*, vol. 137, pp. 81–93, Apr. 2019, doi: 10.1016/j.tws.2018.12.027.

[13] M. Feng, Y. C. Wang, and J. M. Davies, 'Thermal performance of cold-formed thin-walled steel panel systems in fire', *Fire Saf J*, vol. 38, no. 4, pp. 365–394, Jun. 2003, doi: 10.1016/S0379-7112(02)00090-5.

[14] S. Gunalan, P. Kolarkar, and M. Mahendran, 'Experimental study of load bearing cold-formed steel wall systems under fire conditions', *Thin-Walled Structures*, vol. 65, pp. 72–92, 2013, doi: 10.1016/j.tws.2013.01.005.

[15] M. Rusthi, A. Ariyanayagam, M. Mahendran, and P. Keerthan, 'Fire tests of Magnesium Oxide board lined light gauge steel frame wall systems', *Fire Saf J*, vol. 90, pp. 15–27, Jun. 2017, doi: 10.1016/j.firesaf.2017.03.004.

[16] N. Soares, P. Santos, H. Gervásio, J. J. Costa, and L. Simões da Silva, 'Energy efficiency and thermal performance of lightweight steel-framed (LSF) construction: A review', *Renewable and Sustainable Energy Reviews*, vol. 78. Elsevier Ltd, pp. 194–209, 2017. doi: 10.1016/j.rser.2017.04.066.

[17] P. Samiee, S. Esmaeili Niari, and E. Ghandi, 'Thermal and structural behavior of cold-formed steel frame wall under fire condition', *Eng Struct*, vol. 252, Feb. 2022, doi: 10.1016/j.engstruct.2021.113563.

[18] A. D. Ariyanayagam and M. Mahendran, 'Fire performance of load bearing LSF wall systems

made of low strength steel studs', *Thin-Walled Structures*, vol. 130, pp. 487–504, Sep. 2018, doi: 10.1016/j.tws.2018.05.018.
[19] P. A. G. Piloto, M. S. Khetata, and A. B. Ramos-Gavilán, 'Analysis of the critical temperature on load bearing LSF walls under fire', *Eng Struct*, vol. 270, Nov. 2022, doi: 10.1016/j.engstruct.2022.114858.
[20] Y. Tao, M. Mahendran, and A. Ariyanayagam, 'Numerical study of LSF walls made of cold-formed steel hollow section studs in fire', *Thin-Walled Structures*, vol. 167, Oct. 2021, doi: 10.1016/j.tws.2021.108181.
[21] D. Perera *et al.*, 'Fire performance of cold, warm and hybrid LSF wall panels using numerical studies', *Thin-Walled Structures*, vol. 157, Dec. 2020, doi: 10.1016/j.tws.2020.107109.
[22] Y. Tao, M. Mahendran, and A. Ariyanayagam, 'Load-bearing walls made of cold-formed steel hollow section studs exposed to fire', *Proceedings of 9th International Conference on Steel and Aluminium Structure*, pp. 1533–1544, 2019.
[23] CEN, 'Eurocode 1: Actions on structures -Part 1-2: General actions - Actions on structures exposed to fire', Brussels, 2002.
[24] ISO, *ISO 834-1 Fire-resistance tests-Elements of building construction-Part 1: General requirements Essai de résistance au feu-Éléments de construction*. Brussels: International Organization for Standardization, 1999.
[25] CEN, *EN 1993-1-2: Eurocode 3: Design of steel structures - Part 1-2: General rules - Structural fire design*. Brussels: Comité Européen de Normalisation, 2005.
[26] CEN, *prEN 1995-1-2: Eurocode 5 – Design of timber structures*. Brussels: Comité Européen de Normalisation.
[27] M. Rusthi, P. Keerthan, M. Mahendran, and A. Ariyanayagam, 'Investigating the fire performance of LSF wall systems using finite element analyses', *Journal of Structural Fire Engineering*, vol. 8, no. 4, pp. 354–376, Sep. 2017, doi: 10.1108/JSFE-04-2016-0002.
[28] M. A. Sultan, 'A Model for Predicting Heat Transfer Through Noninsulate Unloaded SteeI-Stud Gypsum Board Wall Assemblies Exposed to Fire', 1996.
[29] P. Keerthan and M. Mahendran, 'Thermal Performance of Composite Panels Under Fire Conditions Using Numerical Studies: Plasterboards, Rockwool, Glass Fibre and Cellulose Insulations', *Fire Technol*, vol. 49, no. 2, pp. 329–356, Apr. 2013, doi: 10.1007/s10694-012-0269-6.
[30] A. P. Gomes, H. A. De Souza, and A. Tribess, 'Impact of thermal bridging on the performance of buildings using Light Steel Framing in Brazil', *Appl Therm Eng*, vol. 52, no. 1, pp. 84–89, 2013, doi: 10.1016/j.applthermaleng.2012.11.015.
[31] M. Imran, M. Mahendran, and P. Keerthan, 'Mechanical properties of cold-formed steel tubular sections at elevated temperatures', *J Constr Steel Res*, vol. 143, pp. 131–147, Apr. 2018, doi: 10.1016/j.jcsr.2017.12.003.
[32] F. McCann, L. Gardner, and S. Kirk, 'Elevated temperature material properties of cold-formed steel hollow sections', *Thin-Walled Structures*, vol. 90, pp. 84–94, 2015, doi: 10.1016/j.tws.2015.01.007.
[33] P. Arasaratnam, K. S. Sivakumaran, and M. J. Tait, 'True Stress-True Strain Models for Structural Steel Elements', *ISRN Civil Engineering*, vol. 2011, pp. 1–11, Aug. 2011, doi: 10.5402/2011/656401.
[34] L. Gardner and X. Yun, 'Description of stress-strain curves for cold-formed steels', *Constr Build Mater*, vol. 189, pp. 527–538, Nov. 2018, doi: 10.1016/j.conbuildmat.2018.08.195.
[35] N. Vasion, 'Nonlinear Analysis of Structures', 2015, Accessed: Jun. 19, 2023. [Online]. Available: https://scholar.harvard.edu/files/vasios/files/ArcLength.pdf
[36] Ansys, 'Newton-Raphson Procedure', *Release 18.2*. https://www.mm.bme.hu/~gyebro/files/ans_help_v182/ans_thry/thy_tool10.html (accessed Jun. 20, 2023).
[37] Ansys, 'Arc-Length Procedure', *Release 18.2*.

https://www.mm.bme.hu/~gyebro/files/ans_help_v182/ans_cmd/Hlp_C_ARCLEN.html (accessed Jun. 20, 2023).
[38] Ansys, 'SHELL181'. https://www.mm.bme.hu/~gyebro/files/ans_help_v182/ans_elem/Hlp_E_SHELL181.html (accessed Jun. 07, 2023).
[39] Ansys, 'SOLID70'. https://www.mm.bme.hu/~gyebro/files/ans_help_v182/ans_elem/Hlp_E_SOLID70.html (accessed Jun. 07, 2023).
[40] CEN, *EN 1363-1: Fire resistance test - Part 1: General requirements*. Brussels: Comité Européen de Normalisation, 2020.
[41] S. T. Vy and M. Mahendran, 'Screwed connections in built-up cold-formed steel members at ambient and elevated temperatures', *J Constr Steel Res*, vol. 192, May 2022, doi: 10.1016/j.jcsr.2022.107218.
[42] B. W. Schafer and T. Peköz, 'Computational modeling of cold-formed steel: characterizing geometric imperfections and residual stresses', *J Constr Steel Res*, vol. 47, pp. 193–210, 1998.
[43] S. Gunalan and M. Mahendran, 'Fire performance of cold-formed steel wall panels and prediction of their fire resistance rating', *Fire Saf J*, vol. 64, pp. 61–80, 2014, doi: 10.1016/j.firesaf.2013.12.003.
[44] S. Gunalan, 'Structural Behaviour and Design of Cold-formed Steel Wall Systems under Fire Conditions', Queensland University of Technology, Queensland , 2011. Accessed: Jun. 04, 2023. [Online]. Available: https://eprints.qut.edu.au/49799/

Appendix A
Computational data

Table A.1 – Computational data of main simulation

ID	Number of shell (steel) elements	Size of mechanical simulation [GB]	Number of solid (gypsum) elements	Number of solid (glass fiber) elements	Size of thermal simulation [GB]
01	9720	16.30	35776	\	29.30
02	9720	12.40	35776	\	20.40
03	8896	7.37	28416	\	12.70
04	9544	3.37	30784	\	8.82
05	9544	3.37	30784	\	9.84
06	9720	12.40	35776	61096	24.10

Appendix B

Imagens of thermo and thermo-mechanical simulations

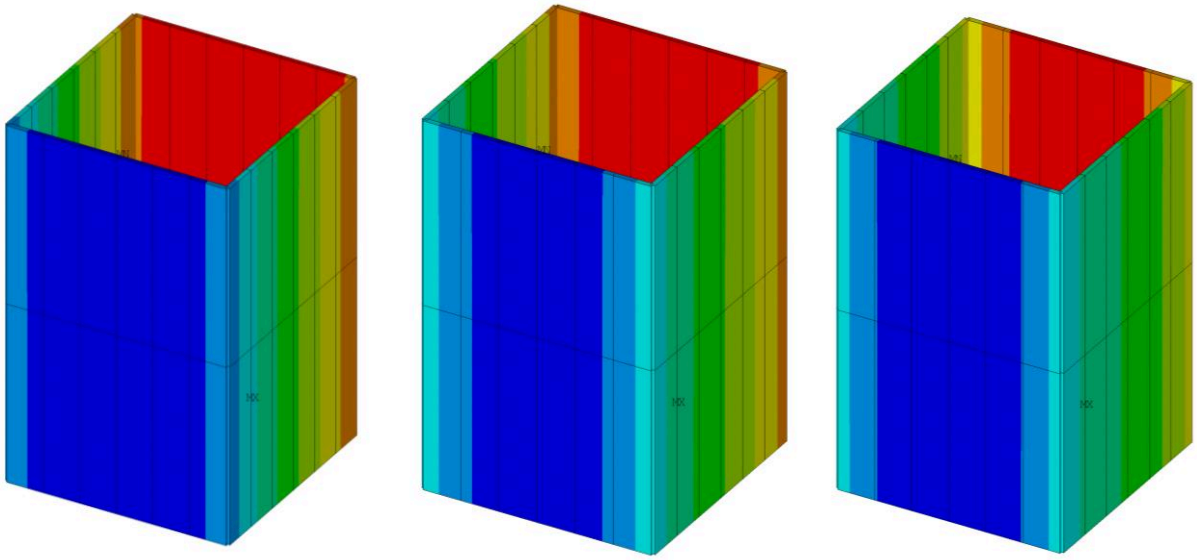

Figure B.1 – Temperature distribution at steel stud after 50, 100 and 150 minutes. Specimen 02.

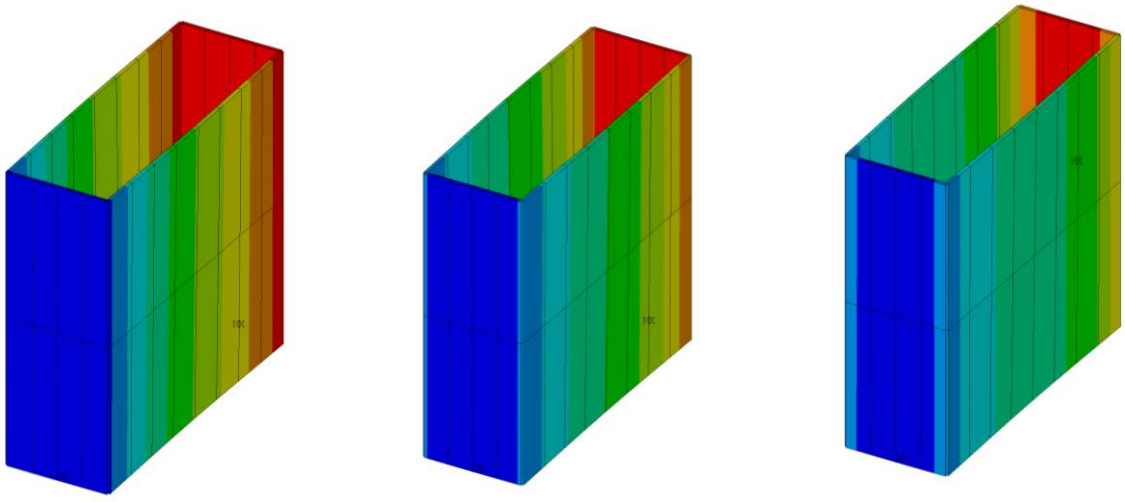

Figure B.2 – Temperature distribution at steel stud after 50, 100 and 150 minutes. Specimen 03.

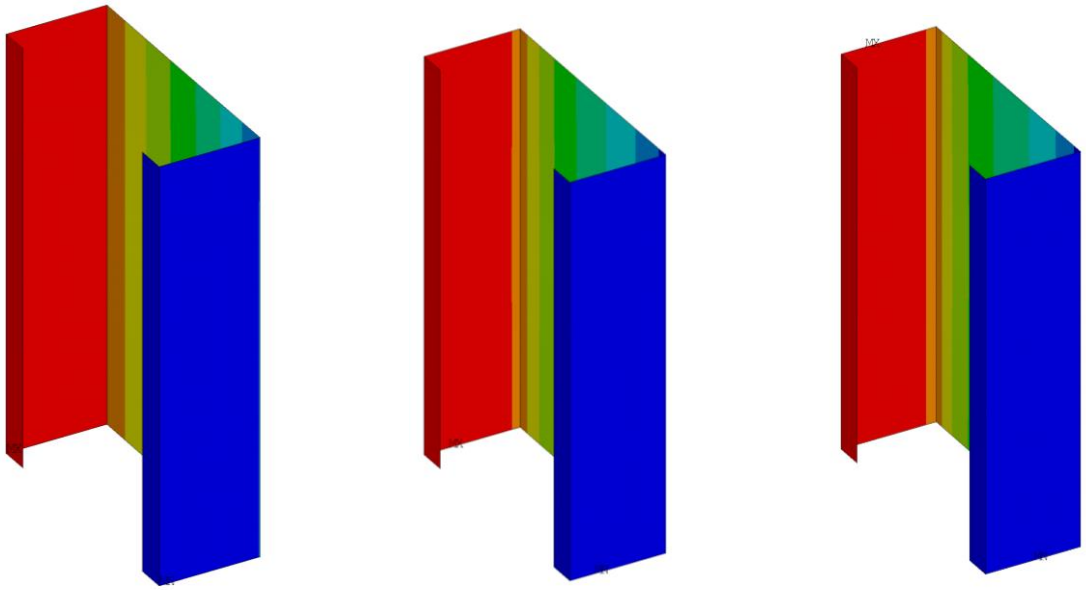

Figure B.3 – Temperature distribution at steel stud after 50, 100 and 125 minutes. Specimen 05.

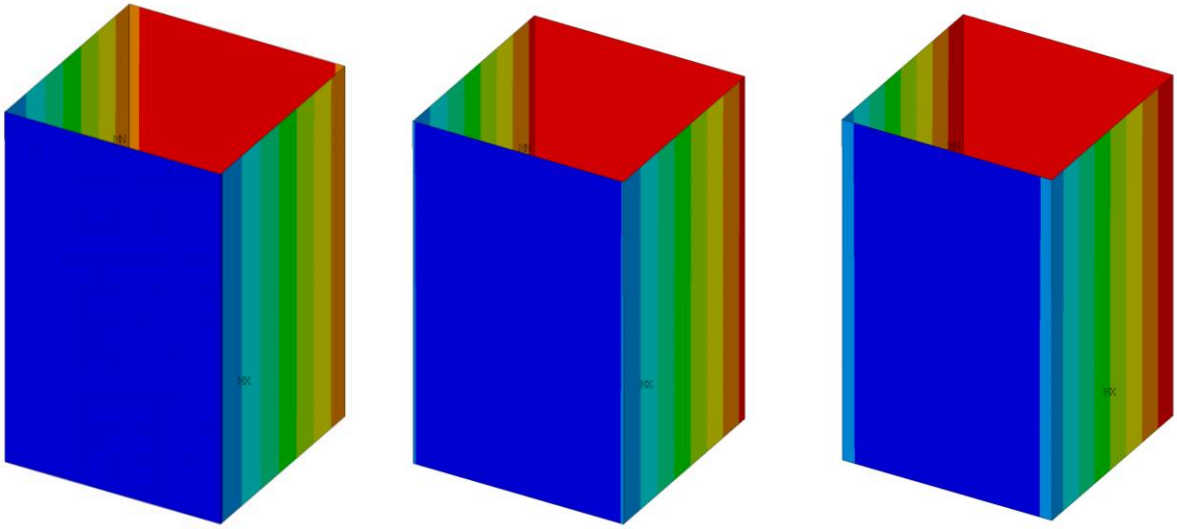

Figure B.4 – Temperature distribution at steel stud after 25, 75 and 125 minutes. Specimen 06.

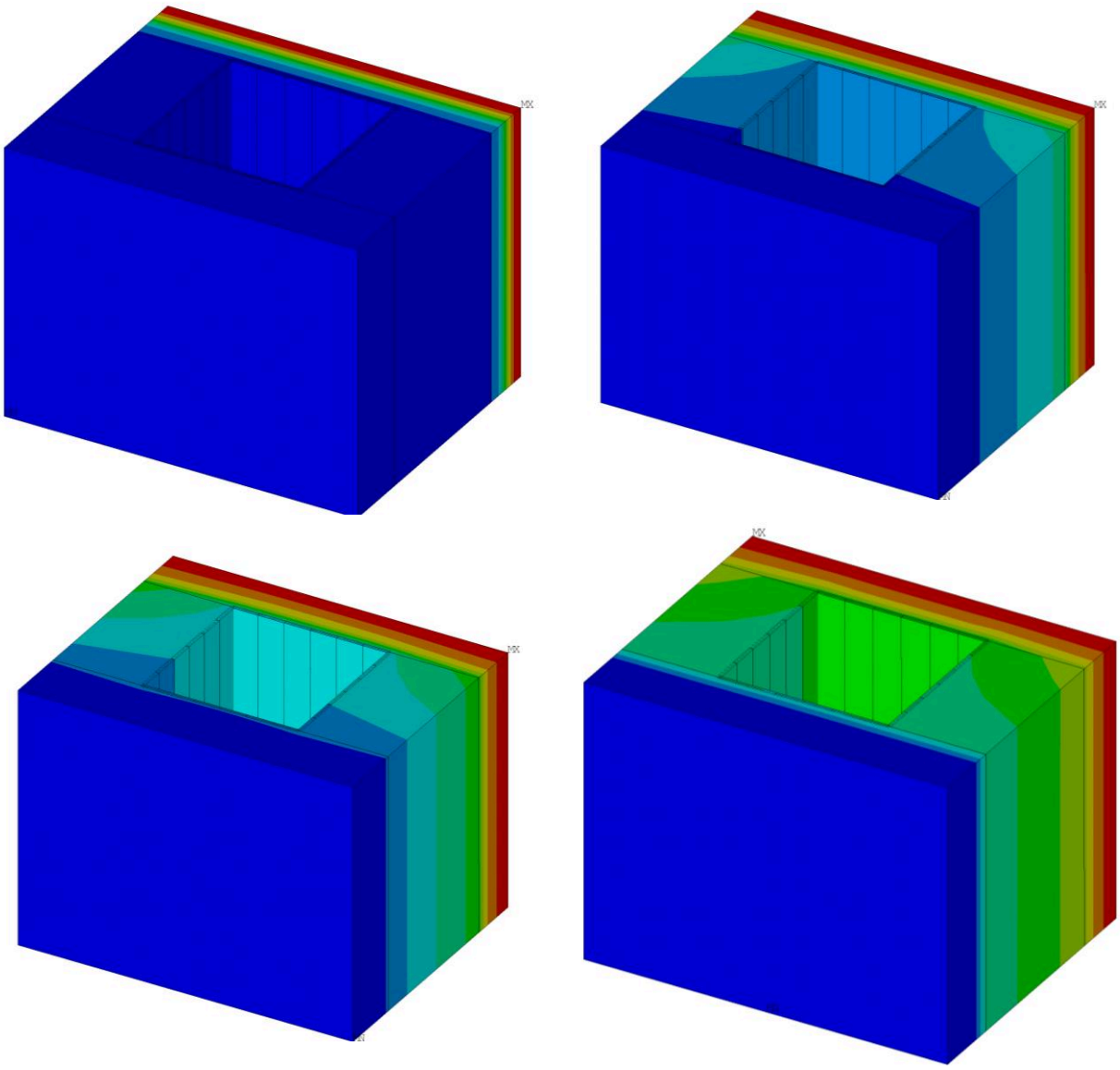

Figure B.5 - temperature distribution through steel and glass fibre.